8-1-2010

Modeling of dendrite growth with cellular automaton method in the solidification of alloys

Hebi Yin

Recommended Citation

Yin, Hebi, "Modeling of dendrite growth with cellular automaton method in the solidification of alloys" (2010). *Theses and Dissertations*. 3150.
https://scholarsjunction.msstate.edu/td/3150

MODELING OF DENDRITE GROWTH WITH CELLULAR AUTOMATON METHOD IN THE SOLIDIFICATION OF ALLOYS

By

Hebi Yin

A Dissertation
Submitted to the Faculty of
Mississippi State University
in Partial Fulfillment of the Requirements
for the Degree of Doctorate of Philosophy
in Mechanical Engineering
in the Department of Mechanical Engineering

Mississippi State, Mississippi

August 2010

By

Hebi Yin

MODELING OF DENDRITE GROWTH WITH CELLULAR AUTOMATON

METHOD IN THE SOLIDIFICATION OF ALLOYS

By

Hebi Yin

Approved:

Sergio D. Felicelli
Professor of Mechanical Engineering
Advisor

John Berry
Professor of Mechanical Engineering
(Committee Member)

Rogelio Luck
Professor of Mechanical Engineering
(Committee Member)

Liang Wang
Research Assistant Professor
Center for Advanced Vehicular Systems
(Committee Member)

David L. Marcum
Professor of Mechanical Engineering
(Graduate Coordinator)

Sarah A. Rajala
Dean of the Bagley College of
Engineering

Name: Hebi Yin

Date of Degree: August 7, 2010

Institution: Mississippi State University

Major Field: Mechanical Engineering

Major Professor: Sergio D. Felicelli

Title of Study: MODELING OF DENDRITE GROWTH WITH CELLULAR AUTOMATON METHOD IN THE SOLIDIFICATION OF ALLOYS

Pages in Study: 168

Candidate for Degree of Doctorate of Philosophy

Dendrite growth is the primary form of crystal growth observed in laser deposition process of most commercial metallic alloys. The properties of metallic alloys strongly depend on their microstructure; that is the shape, size, orientation and composition of the dendrite matrix formed during solidification. Understanding and controlling the dendrite growth is vital in order to predict and achieve the desired microstructure and hence properties of the laser deposition metals.

A two dimensional (2D) model combining the finite element method (FE) and the cellular automaton technique (CA) was developed to simulate the dendrite growth both for cubic and for hexagonal close-packed (HCP) crystal structure material. The application of this model to dendrite growth occurring in the molten pool during the Laser Engineered Net Shaping (LENS®) process was discussed. Based on the simulation results and the previously published experimental data, the expressions describing the relationship between the cooling rate and the dendrite arm spacing (DAS), were proposed. In addition, the influence of LENS process parameters, such as the moving speed of the laser beam and the layer thickness, on the DAS was also discussed. Different

dendrite morphologies calculated at different locations were explained based on local solidification conditions. And the influence of convection on dendrite growth was discussed. The simulation results showed a good agreement with previously published experiments. This work contributes to the understanding of microstructure formation and resulting mechanical properties of LENS-built parts as well as provides a fundamental basis for optimization of the LENS process.

DEDICATION

I would like to dedicate this dissertation to my family. Without their support I would not have had the determination and diligence to accomplish the body of work presented here. I appreciate my parents, my brother and my sisters, who care for me and encourage me. I am extremely appreciative of my wife, Liyan Wang, who has supported me during all these years. I also thank my lovely son, who always brings me joy and happiness.

ACKNOWLEDGEMENTS

First of all, I would like to thank my advisor, Dr. Sergio D. Felicelli, who has provided me with guidance, mentoring, and friendship that allowed me to complete this dissertation. He kindly helped me and my family on both my living and study during a time of need, which allowed me to be able to focus upon my research. He also gave me valuable suggestion and provided help in finding my future job. I would also like to especially thank Dr. John Berry, Dr. Luck, and Dr. Liang Wang for their guidance and assistance. Discussions with them have been very helpful to me. I will treasure the friendships I made while in graduate school and the many discussions I was able to have. I thank you very much for your friendship and kindness over the years and look forward to collaborating with you all in the future.

I would like to thank Dr. Mark F. Horstemeyer, the team leader of the Computational Manufacturing and Design (CMD) group of the Center for Advanced Vehicular Systems (CAVS). His vast knowledge and passion for science has always been inspiring to me. I also would like to thank Dr. Paul Wang, the manager of the CMD group of the CAVS for providing the resources required for me to carry on the research.

Finally, I would like to thank MSU-CAVS, DOE, and NSF for their financial support.

TABLE OF CONTENTS

Page

CHAPTER

LIST OF TABLES

TABLE Page

LIST OF FIGURES

FIGURE Page

LIST OF ABBREVIATIONS

CA	Cellular Automaton
CFD	Computational Fluid Dynamics
DAS	Dendrite Arm Spacing
DMD	Direct Metal Deposition
FD	Finite Difference
FE	Finite Element
FT	Front Tracking
FV	Finite Volume
HCP	Hexagonal close-packed
LB	Lattice Boltzmann
LCF	Laser cladding forming
LENS	Laser Engineered Net Shaping
LS	Level Set
LSFF	Laser Solid Freedom Fabrication
MC	Monte Carlo
PDAS	Primary Dendrite Arm Spacing
PF	Phase Field
SDAS	Secondary Dendrite Arm Spacing
SL	Solid-Liquid

LIST OF NOMENCLATURE

α	Thermal diffusivity
β	Thermal expansion coefficient
γ	Surface tension
δ	Anisotropy coefficient
ε	Emissivity of the part surface
$\varepsilon_{\emptyset}$	Gradient energy coefficient
η	Dendrite Arm Spacing
η_2	Secondary Dendrite Arm Spacing
θ_0	Angle of the preferential growth direction with respect to the x-axis
λ	Thermal conductivity
λ_s	Thermal conductivity of solid
λ_l	Thermal conductivity of liquid
μ	Dynamic viscosity
ν	Kinematic viscosity
ξ	Cooling rate
ρ	Density
ρ_l	Density of liquid
ρ_s	Density of solid
$\bar{\rho}_s$	Average density of solid
σ	Stefan-Boltzmann constant

σ_k	Surface tension gradient
τ_v	Relaxation time for fluid flow
τ_α	Relaxation time for thermal transfer
τ_c	Relaxation time for solute transfer
φ	Growth angle between the normal to the interface and the x-axis
$\emptyset$	Field variable
Γ	Gibbs-Thomson coefficient
$\mathit{\Gamma}$	Interface kinetic coefficient
K_i	Permeability in the i coordinate direction
Ω	Domain
Ω^l	Domain for liquid
Ω^s	Domain for solid
2D	Two dimensional
3D	Three dimensional
a	Size of the cell
c	lattice Boltzmann velocity
c_i	Solute concentration for i phase (solid or liquid)
c_s^*	Interface solute concentration in solid phase
c_l^*	Interface solute concentration in liquid phase
c_0	Initial solute concentration
c_l	Solute concentration in liquid
c_s	Solute concentration in solid
$\overline{c^j}$	Mixture concentration of solute j
c_l^j	Liquid concentration of solute j

c_σ	Concentration at LB method
$\bar{c}_\sigma$	Boundary constant concentration at LB method
C_p	Specific heat
C_s	Specific heat of solid
C_l	Specific heat of liquid
d	Normal distance
d_s	Length of the diagonal of the seed
D_l	Solute diffusivity for liquid
D^j	Diffusivity of solute j
D_i	Solute diffusivity for i phase (solid or liquid)
e	Macroscopic energy
e_a	Discrete velocities at a directions ($a = 0, \dots 8$)
f_a	Density distribution function for flow at a directions ($a = 0, \dots 8$)
f_a^{eq}	Equilibrium distribution function at a directions ($a = 0, \dots 8$)
f_l	Fraction of liquid
f_s	Solid fraction
$f_{T,a}$	Density distribution function for temperature at a directions ($a = 0, \dots 8$)
$f_{T,a}^{eq}$	Equilibrium function for temperature at a directions ($a = 0, \dots 8$)
F	Free energy function
Δf_s	Increase of solid fraction
g	Gravitational acceleration
g_i	Magnitude of gravity in the i coordinate direction
g_a	Density distribution function for solute at a directions ($a = 0, \dots 8$)
g_a^{eq}	Equilibrium distribution function for solute at a directions ($a = 0, \dots 8$)

G_r	Grashof number
h	Convective heat transfer coefficient
ΔH	Enthalpy of freezing
k	Partition coefficient
k^j	Partition coefficient for solute j
K	Curvature at interface
L	Latent heat
L_b	Characteristic length for the buoyancy force
L_R	Characteristic length taken as the pool radius
m	Number of cell for each side of FE mesh
m_l	Liquidus slope
m^j	Slope of liquidus for solute j
M_a	Marangoni number
n	Normal direction
N_{max}	Maximum nucleation density
p	Pressure
p^n	Nucleation probability
P_e	Peclet number
$\overrightarrow{q^s}$	Heat flux at interface in solid
$\overrightarrow{q^l}$	Heat flux at interface in liquid
t	Time
T	Temperature
T_0	Initial temperature
T_a	Ambient temperature

T_W	Wall temperature
T_E	Eutectic temperature
T_s	Solidus temperature
T_l	Liquidus temperature
T^l	Interface temperature in liquid
T^s	Interface temperature in solid
T^H	Temperature releasing the latent heat
T^*	Interface equilibrium temperature
T_l^{eq}	Equilibrium liquidus temperature at the initial solute concentration
Δt	Time step
Δt_T	Time step for heat transfer
Δt_c	Time step for mass transfer
ΔT_N	Mean nucleation undercooling
ΔT_σ	Standard deviation of undercooling
u	Liquid velocity
u_i	Velocity at i coordinate direction
$\overline{u}$	Superficial velocity
v_0	Force boundary flow velocity
V	Volume
V_c	Volume of a single cell
V_n	Interface normal velocity
$\vec{V}$	Velocity vector
w_a	Weight function at a directions ($a = 0, \ldots 8$)
X	Lattice node

∇	Gradient operator

CHAPTER I

INTRODUCTION AND LITERATURE SUMMARY

1.1 Research blackground

The solidification process is an important step in the manufacturing of components. In most cases, mechanical properties depend on the solidification structure at micro-scale level, including grain size or secondary dendrite arm spacing, grain type, and so on. Figures 1.1 a) and b) show the relationships between the yield strength and the grain size [1] and secondary DAS (SDAS) [2]. The yield strength increases with decreasing grain size or SDAS. As the grain size decreases, the ratio of surface area to volume of the grain will increase, which allows more buildup of dislocations at the grain boundary. Also, the build-up of dislocations increase the yield stress of the materials since it requires a lot of energy to move dislocations to another grain. It is the well known Hall-Petch strengthening.

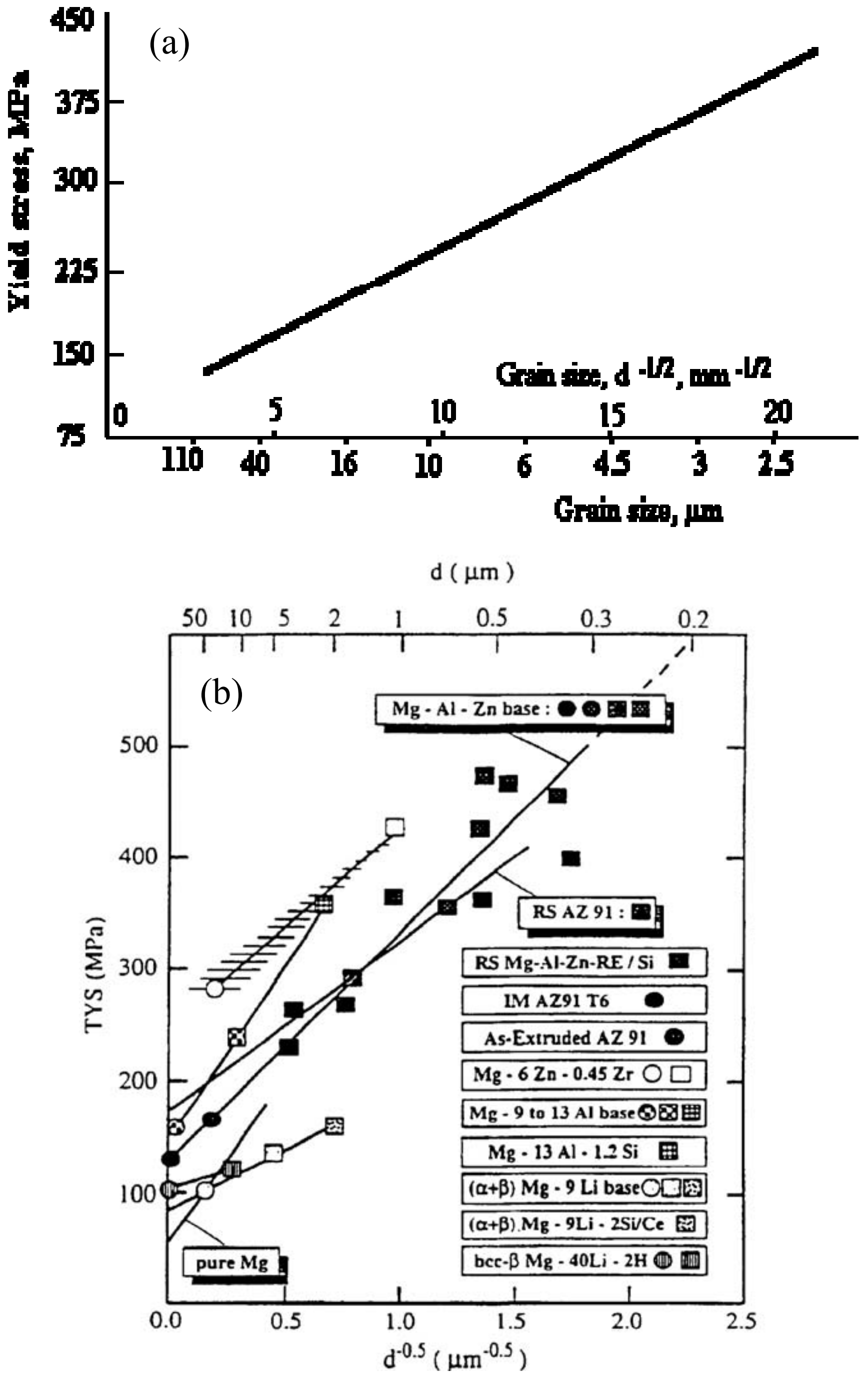

Figure 1.1 Relationship between yield strength and (a) grain size [1] and (b) secondary dendrite arm spacing [2]

However, the component with fine grain size is not always a good choice [3]. When creep resistance is required, eliminating grain boundaries is needed. Figure 1.2

show the gas turbine blades of Nickel-base superalloys obtained using a ceramic mould by different casting methods, producing different microstructure: quiaxed, columnar, and single-crystal grain microstructure. For the equiaxed grain microstructure, the presence of grain boundaries makes this structure susceptible to creep and cracking along those boundaries under centrifugal forces at elevated temperatures. For the columnar grain microstructure, the longitudinal but not transverse grain boundaries makes the blade stronger in the direction of the centrifugal forces developed in the gas turbine. For the single crystal blade, the lack of grain boundaries makes these blades resistant to creep and thermal shock. Thus, they have a longer and more reliable service life.

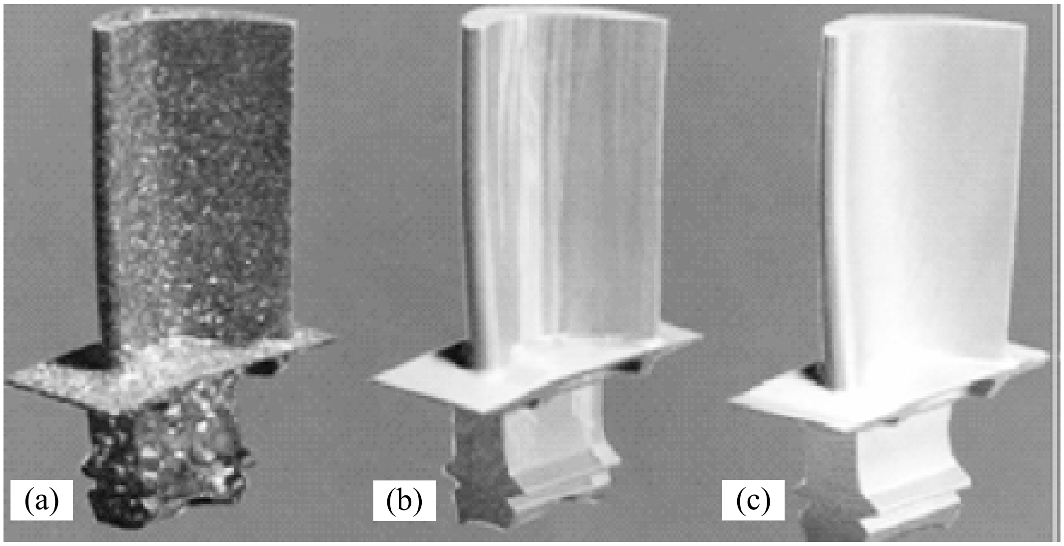

Figure 1.2 Nickel-based superalloy turbine blades solidified as (a) equiaxed grains, (b) columnar grains, and (c) a single crystal [3]

Since the importance of the prediction of solidification microstructure, this work talks about the development of modeling the dendrite growth. The dendrite growth is the primary form of crystal growth observed in the Laser Engineered Net Shaping (LENS®), and the properties of metallic alloys strongly depend on their microstructure; besides, understanding and controlling the dendrite growth is vital in order to predict and achieve the microstructure and hence the mechanical properties. The application of the model to the prediction of dendrite growth in the solidification of molten pool during LENS was especially discussed.

1.2 Description of the LENS process

LENS is a rapid fabrication process through which near-net-shaped three-dimensional (3D) components are built by the successive overlapping of layers of laser melted powder by computer-guided movement of the substrate or the laser in 3D space. The LENS fabrication technique was developed by Sandia National Laboratories in the late 90's, and it is gaining popularity as a rapid prototyping and repair technology because of its cost saving potentials and high cooling rates leading to fine microstructures similar to those observed in rapid solidification [4-6].

A typical LENS system consists of four parts: a laser, a controlled-atmosphere glove box, a 3D computer-controlled positioning system, and several powder-feed units as Figure 1.3 shows. Laser beam creates a small melt pool at the top surface into which the feed-metal powder is delivered. The powder melts and then begins to solidify. The combined effects of surface melting with newly-added-powder melting gives rise to the formation of a new layer.

Various alloys have been used in the LENS process, such as, stainless steel, tool steel, nickel-based alloys, and titanium alloys. LENS has several advantages over the traditional metal processing, including low cost and time saving, enhanced design flexibility and automation, and superior material properties. The main distinct applications of LENS technology include applying metal to existing parts and repairing worn or broken parts, 3D product with thin section or depth-to-diameter aspect ratios, and solid parts with complex internal and external features near to net shape.

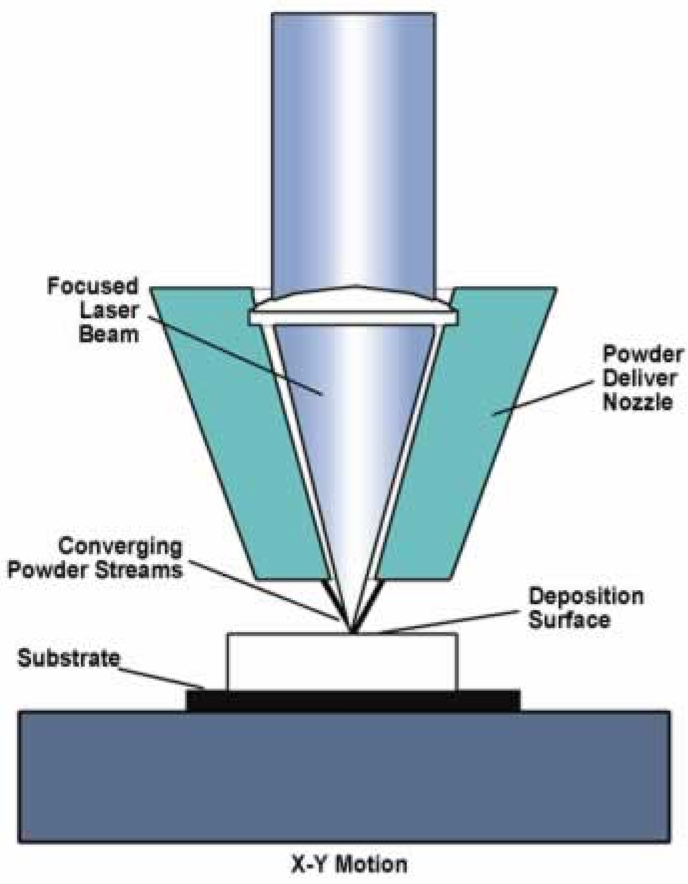

Figure 1.3 Schematic of a typical LENS system

1.3 Experiment on thermal behavior during LENS process

Since the complex manufacturing process, the LENS process is not yet fully understood, and the selection of process parameters is still often based on previous experience and trial and error experimentation. Appropriate tuning of the laser power, travel speed, powder flow rate, and several other parameters is essential to avoid defects and undesired microstructures. Kurz [7], Kelly and Kampe [8], Colaco and Vilar [9-10], among others, have shown that the microstructure and mechanical properties obtained with the LENS process partly depend on the solid-state transformations during cooling down to room temperature. However, the transformations are mainly driven by the consecutive thermal cycles during the LENS process when the laser beam moves along the part surface line by line and layer by layer. Therefore, it is critical to understand the local thermal cycles and temperature history in order to predict the solid phase transformations and thus the final microstructure in the part. Many experimental works have been done to characterize the thermal behavior during LENS deposition.

1.3.1 Thermocouple measurements

A relatively easy way to obtain a thermal signature during processing is by inserting thermocouples directly into the sample during fabrication. A sample of single-pass-width wide shell boxes with equal side lengths of 6.35cm was fabricated by Griffith *et al*. [11-13] from H13 tool steel with varying laser powers and traverse velocities. A fine diameter (10µm) Type C thermocouple bead was inserted directly into the deposition sample zone to obtain the accurate thermal history during the LENS fabrication for twenty deposition layers. The experimental temperature traces at one position were shown in Figure 1.4 as twenty layers were deposited on top of the thermocouple inserted into H13 LENS shell build.

Some experiments were also conducted to obtain temperature measurement data by K-type thermocouple. Pinkertona [14] positioned K-type thermocouple on the side surface of the uppermost deposited track, halfway along it. An experiment was conducted by Peyre *et al*. [15] that 0.2mm diameter type-K thermocouples were spot welded at different locations in the substrate, as close as possible (0.5-4mm) from the manufactured wall, to record temperature versus time data.

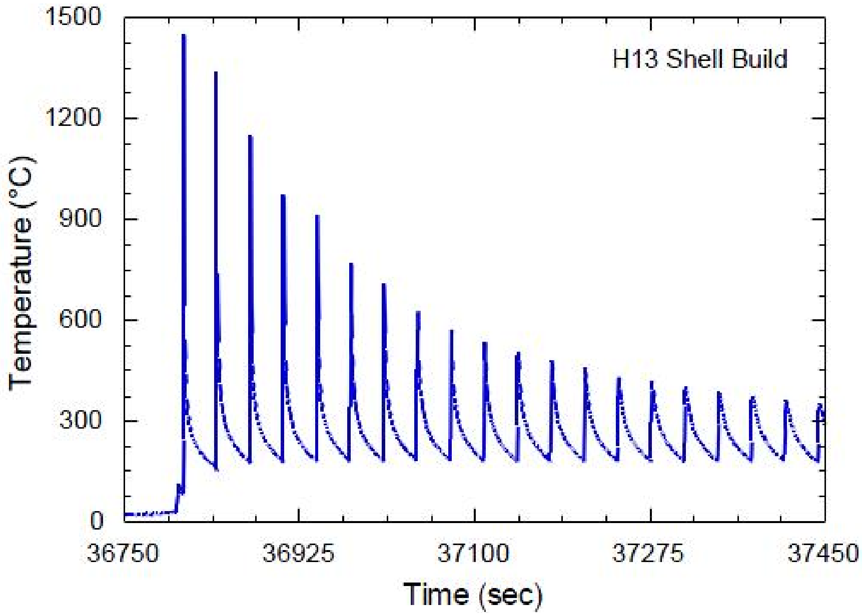

Figure 1.4 In-situ temperature readings for twenty deposition layers

1.3.2 Non-invasive thermal imaging

It is known intuitively that a thermal gradient exists across the molten pool and into the bulk material created by the LENS process. The nature and extent of this gradient has not been fully characterized. Since mechanical properties are dependent upon the microstructure of the material, which in turn is a function of the thermal history of solidification, an understanding of the temperature gradient induced by LENS processing is of special interest. It would be particularly beneficial to use non-invasive thermal imaging to measure the temperature profile and gradients and to use these thermal profiles in feedback control.

Hofmeister *et al*. [16] employed a digital 64×64 pixel CCD video camera with thermal imaging techniques to observe the molten pool. The thermal-imaging camera views the sample through a CaF viewpoint in the front of the LENS glove box. The experimental setup is shown in Figure 1.5. These experiments were conducted on AISI316 stainless steel using two different particle size distributions. The molten pool size was analyzed from the thermal images (shown in Figure 1.6(a)), and the temperature gradients and cooling rates in the vicinity of the molten pool were also obtained as shown in Figure 1.6(b) and (c) respectively. Griffith and Hu *et al.* [12, 13, 17] conducted similar experiments with 320×244 and 128×128 pixel CCD respectively.

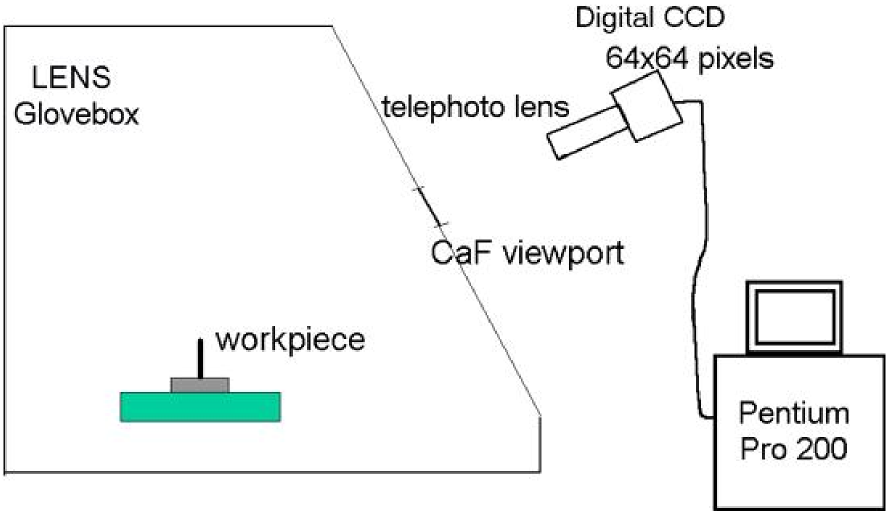

Figure 1.5 A schematic of the thermal-imaging experimental setup for LENS

The smart digital CMOS camera (Fastcam Photron) was also used to capture the thermal image [15, 18]. It is a powerful standalone vision-capture device and has the capability to measure the melt pool and adjacent region simultaneously and their evolution with incremental layers. Compared to the typical CCD camera, the CMOS camera converts the light intensity to voltage in a logarithmic manner other than linear which expands measurement range. This feature allows the CMOS camera to work efficiently at such a strong light intensity circumference as the laser material process.

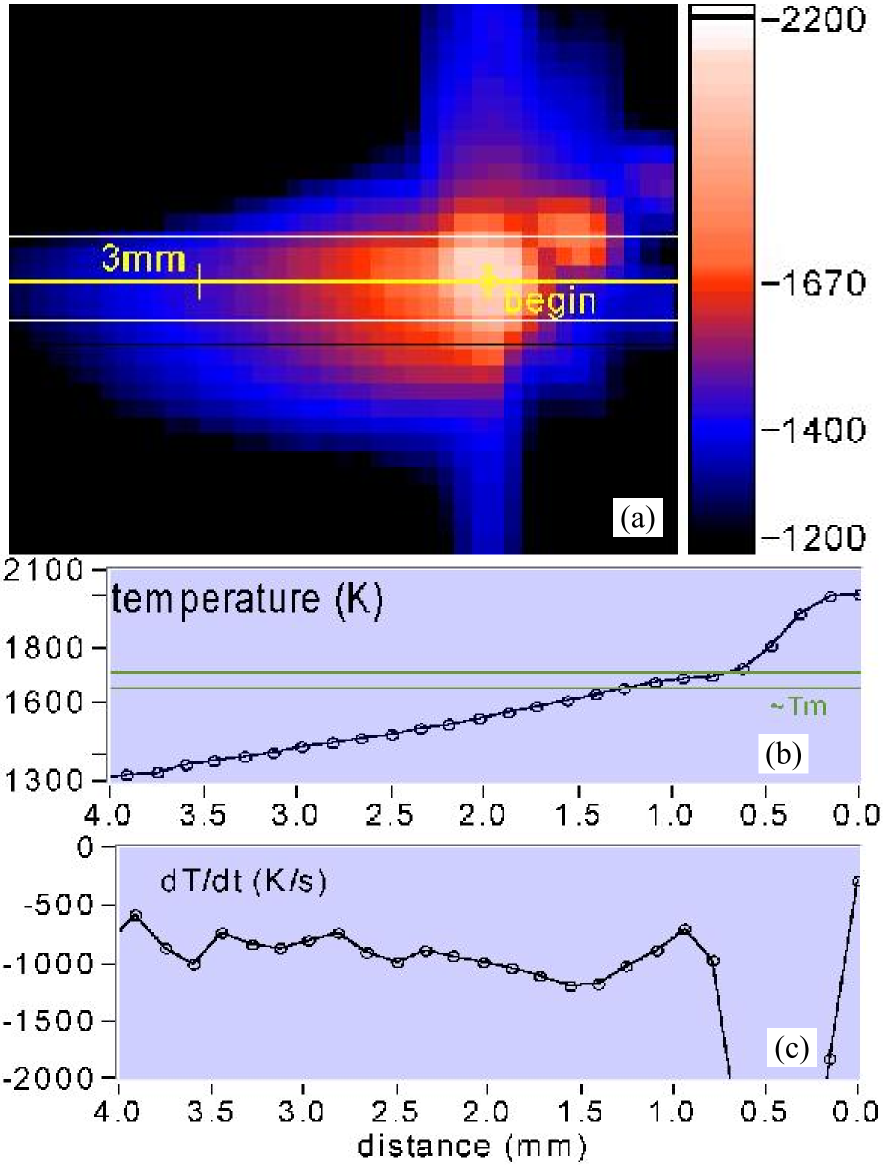

Figure 1.6 (a) A thermal image of the line build with corresponding graphs of (b) the temperature distribution along the yellow cursor and (c) the cooling rate [16]

1.4 Heat transfer simulation

However, the experimental measurement of a detailed thermal history in the part is difficult to achieve because the required experiments would be very costly and time-consuming. An alternative approach is to use numerical simulation with appropriate mathematical models. Many numerical models have been developed to try to establish an understanding of the thermal behavior in the LENS process.

Grujicic *et al*. [19, 20] developed a two-dimensional (2D) finite difference (FD) model to calculate the temperature profiles in the fabricated part when the laser beam moved across the top surface of the sample, obtaining the minimum power of the laser needed to initiate melting of the part surface. Jendrzejewski *et al*. [21] developed a 2D finite element (FE) modeling of temperature distribution for multi-layer structures by direct laser deposition in an Ar environment to numerically obtain and compare with experimental data, and powders of bronze B10 and stellite SF6 alloys and also base plates of S235JR steel were taken as sample materials. Kelly and Kampe [8] developed a 2D transient thermal model to calculate the temperature distribution for multiple layer depositions of the titanium alloy Ti-6Al-4V during a single-line build, and implicit (backward-difference) FD techniques was taken to solve the transient-heat-conduction equation. Wang and Felicelli [22] predicted the temperature distribution during deposition of AISI316 stainless steel as a function of time and process parameters by developing a 2D thermal model with one layer of deposition.

Besides the 2D models, 3D models were also built. Ye *et al*. [23] developed a 3D FE model to predict temperature distribution during the process, especially near the molten pool. Their results showed good agreement with experimental observations. In the simulation process, a thin wall part deposited on the substrate was discretized by using cubic solid elements. For AISI316 stainless steel thin wall fabricated in the LENS process, numerical simulation was performed to study the entire thermal behavior in process. Temperature distribution and gradient in the fabricated part were obtained from the results of FE method simulation. Costa *et al*. [24] developed and applied a 3D FE model to calculate the thermal history in a single-wall plate. They also studied the influence of substrate size and idle time on the temperature field of the fabricated parts. A paper by Alimardani *et al*. [25] presented a 3D transient numerical approach for modeling the multilayer laser solid freeform fabrication (LSFF) process. Using this modeling approach, the geometry of the deposited material as well as temperature and thermal stress fields across the process domain could be predicted in a dynamic fashion. Dai and Shaw [26] developed a 3D FE model to investigate the effects of the volume shrinkage due to transformation from a powder compact to dense liquid on the temperature distribution and the size of the transformation zone during laser densification. The results showed that simplified models that did not include the local geometry change due to the volume shrinkage during densification provided good estimations of the temperature field.

Some commercial softwares were used to simulate the thermal behavior for the laser deposition process. Peyre *et al*. [15] carried out a 3D FE calculation on COMSOL 3.3 Multiphysics software to describe thermal behavior during direct metal deposition (DMD) of a titanium alloy. Labudovic *et al*. [27] developed a 3D model for direct laser metal powder deposition process and rapid prototyping with commercial software ANSYS. The model calculated transient temperature profiles, dimensions of the fusion zone, and residual stresses. Wang *et al*. [28] developed a 3D FE model using the commercial software SYSWELD to study the molten pool size by analyzing the temperature and phase evolution in stainless steel 410 during the LENS deposition of a thin-walled structure.

1.5 Fluid flow simulation

1.5.1 Fluid flow simulation for welding

Beside the heat transfer simulation, a number of 2D and 3D numerical models have also been developed to understand fluid flow phenomena in welding processes. Fusion zone geometry can be predicted from the transient heat transfer and fluid flow with natural convection model for various conditions [29-33]. The velocity of the liquid metal in the weld pool increases with time during heating, and convection plays an increasingly important role in the heat transfer in the weld pool towards the end of the pulse. Many literatures describe the fluid flow in the pool with considering the surface tension induced Marangoni convection. The surface tension force arises because of the spatial variation of surface tension between the middle and the periphery of the weld pool resulting from the temperature variation between the centre and the edges of the melt pool, while the thermal gradients in depth trigger buoyancy flow. The liquid flow is mainly driven by the surface tension and, to a much less extent, by the buoyancy force. Marangoni convection also plays critical role in determining the temperature distribution in the work-piece and melt flow in the weld pool.

Some models [34-37] respectively adopted FD and finite volume (FV) methods to discover that the fluid flow in laser generated melt pool was dominated by Marangoni flow. Sundar *et al*. [36] calculated two cases: (1) without fluid flow, that is, pure conduction and (2) with surface tension driven flow. From the simulation, it was observed that the fluid flow played a significant role in deciding the temperature distribution and the final shape and size of the weld pool. Ye and Chen [37] developed a 3D model to compare the melt flow and heat transfer between the Marangoni convection and natural convection, finding that the Marangoni convection played a critical role in determining the temperature distribution and melt flow in the weld pool and could not be ignored even for the full-penetration welding of a thin plate. Since the melt flow driven by the surface tension gradient as $\partial\sigma/\partial T < 0$ could appreciably enhance the energy transport from the vapor hole, both the length and width of the weld pool increased with increasing Marangoni number. Hughes *et al*. [38] developed a 2D model to discuss the influence of positive and negative surface tensions on pool shapes. For the negative and positive gradient cases the predominant surface flow was away from and towards the heat source respectively. The convective heat transport was consequently directed towards or away from the axis, resulting in either a deeper or flatter weld pool shape respectively.

The analysis by He *et al*. [39] showed that the liquid metal convection continued to be an important mechanism for heat transfer within the weld pool as the scale of the weld was reduced in linear and spot laser micro-welding operations in comparison with the conventional welds. Even with relatively small dimensions of laser micro-welds, the Peclet number was found to be large enough for Marangoni convection to be important in the heat transfer.

However, some works indicated that heat conduction sometimes played an important role in the heat transfer in the weld pool under some particular conditions. Rai *et al*. [40] developed a 3D model to calculate the temperature and velocity fields and weld pool geometry for welding systems. It was shown that the temperature profile and the weld pool's shape and size depended strongly on the convective heat transfer for low thermal conductivity alloys like stainless steel. For high thermal conductivity aluminum alloys, convection did not play a significant role in determining the shape and size of the weld pool. The weld cross sections for AISI304 stainless steel showed a large width near the surface which narrowed considerably toward the bottom due to convection dominated heat flow. On the other hand, the main mechanism of heat transfer during welding of 5754 aluminum alloy was heat conduction during keyhole mode laser welding. And He *et al.* [41] also found that heat transfer by conduction was important when the liquid velocity was small at the beginning of the pulse and during weld pool solidification.

A few articles [42, 43] even discussed about the turbulent convection in the weld pool. Chakraborty *et al.* [43] carried out two sets of simulations from a 3D model for the same set of processing parameters: one with the turbulence model and the other without activating the turbulence model. The enhanced diffusive transport associated with turbulence was shown to decrease the maximum values of temperature, velocity magnitude, and copper mass fraction in the molten pool. The composition distribution in turbulent simulation was found to be more uniform than that obtained in the simulation without turbulent transport. In addition to that, the maximum values of these quantities were also found to be smaller in the turbulent pool than the corresponding magnitudes obtained from the laminar simulation, since the eddy mass diffusivities turned out to be several orders of magnitude higher than the corresponding molecular mass diffusion coefficients of molten metal.

Some models [44, 45] assumed the flat top surface of the model pool while calculating the fluid flow in the weld pool, and some others [30, 46-48] calculated the free surface. Surface profile was calculated by minimizing the total surface energy [30, 46]. Level set (LS) method was also used to get the free surface [47]. Ha and Kim [48] discussed the Marangoni effect with deformable free surface in fixed grid system. The free surface elevated near the weld pool edge and descended at the center of the weld pool if dr/dT was dominantly negative. The predicted width and depth of the weld pool with moving surface were a little greater than those with flat weld pool surface. It was believed that the oscillation of the weld pool surface during the melting process enhanced the rate of convective heat transfer in the weld pool.

1.5.2 Fluid flow simulation in the molten pool for laser deposition

Compared to the large works on the fluid flow for welding, only a few papers [49-53] were published to investigate the fluid flow in the molten pool for the laser deposition or laser surface melting. The simulation results of the models with free surface movement by LS approach showed that Marangoni driven convection played significant roles on heat dissipation and melt pool shape [49-51]. Lei *et al*. [52] found that if a pure conduction model was used or only buoyancy-driven flow was considered one would more greatly over predict the surface temperature. When surface-tension temperature coefficient was less than zero, the flow was outward from the center of the pool to the pool periphery and resulted in a shallow and wide pool shape. Three dimensional model [53] was applied to laser processing of AISI 304 stainless steel. The effects of heat conduction, Marangoni flow, and thermal buoyancy on melting process and shape of molten pool were thoroughly analyzed. Marangoni flow made a molten pool wider and shallower by comparing to the heat conduction.

1.6 Properties and microstructure for LENS parts

1.6.1 Properties of LENS components

A lot of experiments [12, 13, 54-66] have been conducted to examine the mechanical properties of LENS deposited material, and various materials have been involved, such as steel alloys, In alloys, Ti alloys, and Al alloys. Hardness has been tested for LENS deposited materials, such as H13 [12, 54], AISI4140 [55], WC-Co [56], Fe-based metallic glass [57], and AIS316 [59]. Some calculations on the hardness were also carried out, including AISI420 [24], H13 [54, 58], and AISI316 [59]. The experiment and calculation results showed that hardness had a slightly higher value when having a higher moving speed of laser beam. Also Sandia report in 1999 [62] showed that the LENS AISI308 component had higher hardness than the annealed AISI308. The ultimate tensile strength and yield tensile strength were also tested for many materials. Many materials including Sandia report in 2006 [65] showed that LENS deposited components had superior strength properties to annealed material, such as AISI304 [60, 64], AISI316 [61], AISI308 [62], and 663 copper alloy [66]. Zheng *et al*. [59] also compared the tensile mechanical properties for LENS and conventional wrought AISI316 and investment cast, and comparison [66] was also made by LENS to sand mould casting for 663, and the same results were concluded. Griffith *et al*. [13] reported a partial list of the room temperature mechanical properties for alloys fabricated parts by LENS, ranging from stainless steels to titanium to nickel-based alloys. It was found from the results that, in most cases, the LENS properties were as good as if not better than the traditionally fabricated material. For AISI316, the yield strength was double that of wrought while retaining a ductility of nearly 50%. This is most likely due to Hall-Petch grain size refinement, where finer grain sizes result in higher yield strengths. Typical LENS-processed grain sizes range from 1-10 microns, where traditional wrought material is around 40 microns.

1.6.2 Microstructure for LENS parts

The cooling rate calculated in present research is found to be as high as 10^4K/s, which leads to a fine microstructure. Several other numerical simulation [21, 67-69] and experimental [13, 59, 70, 71] results have also reported that the cooing rate was usually determined to be in the range of 10^3 to 10^4K/s.

Many experiments conducted with various alloys under different operation conditions have proved that the dendrite structure could be observed [14, 59, 70, 72-85], and some experiments [79-85] have proved that cell and column/dendrite coexist. The grain size is as fine as a few microns [16, 59, 68, 72, 73, 75, 76, 85-91] due to the high cooling rate. Both cellular and dendrite structures were observed by Smugeresky *et al.* [90], and the cell sizes and the SDAS were in the range of 2 to 15μm, with laser power 150-600W, travel speed of 4.2-16.9mm/s for AISI316. Hofmeister *et al.* [16] found that the average dendrite mean intercept length increased from 3 to 9μm when increasing the laser power for deposition of AISI316. In laser deposition of Ni-based alloys, it has also been observed that the primary DAS (PDAS) was about 5μm and that the SDAS was in the range of 1.5 to 2.5μm [76]. A summary of reported microstructures for different materials and deposition processes is given in Table 1.1. Note that reported dendrite dimensions differ for the same material; this is probably due to the different operation parameters during the deposition process.

Table 1.1 Measured grain and dendrite sizes

Materials	Dimension (μm)	Process	Reference
AISI316	DAS:1.31-3.0	LENS	[85]
AISI308	PDAS: 4	LENS	[86]
AISI308	PDAS: 4	LENS	[87]
H13	Grain width: 4-20	DMD	[75]
H13	SDAS: 2	LENS	[73]
AISI316	Mean intercept length: 3.25-8.68	LENS	[16]
H13	PDAS: 1.5-4; SDAS: 2-5.5	DMD	[68]
AISI304	Grain width: ~10	LENS	[89]
AISI316	SDAS: <5	LENS	[72]
Ni-based alloy	PDAS: 5; SDAS: 1.5-2.5	DMD	[76]

Table 1.1 (Continued)

AISI316	PDAS: 8-20	LCF	[59]
AISI316	SDAS: 2-15	LENS	[90]
H13	Grain width: 6.4-12.2	DMD	[91]

Different dendrite morphologies can be obtained by controlling the thermal gradient (G) and cooling rates (solidification velocity (R)) in the molten pool [14, 92, 93]. Some analytic models were also built to prove the formation of dendrite on the basis of the G and R calculated during the LENS process [68, 94, 95]. Bontha *et al.* [94] determined the relationship between the dendrite morphology, the temperature gradient, and solidification velocity during the LENS process by plotting points in G versus R space as Figure 1.7 shows. The authors found that the resulting grain morphology could be predicted as either columnar, equiaxed, or mixed. The conditions of laser power and laser travel speed for which a fully columnar dendritic structure was also obtained in LENS-deposited Ti-6Al-4V thin walls.

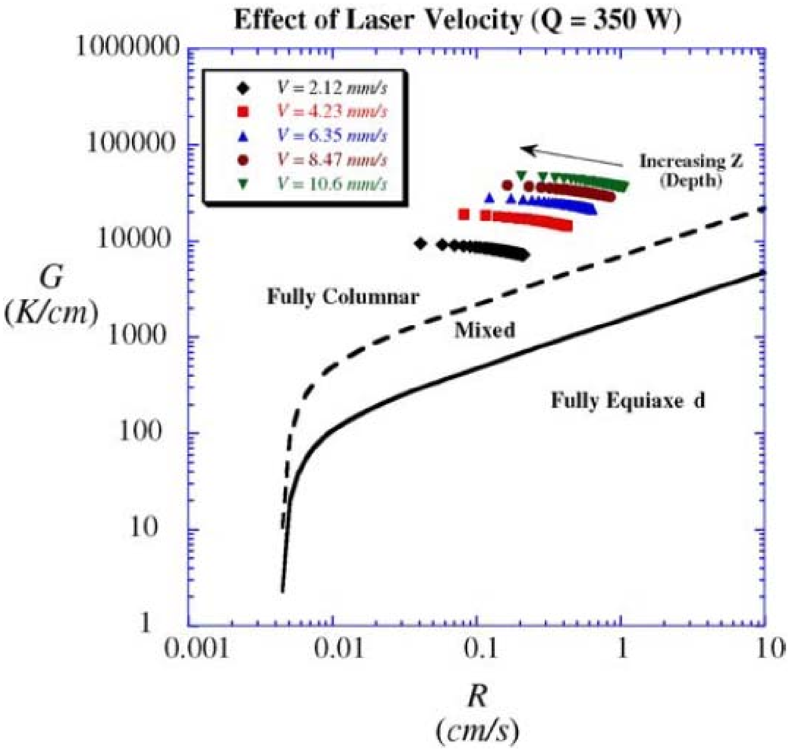

Figure 1.7 Effects of laser velocity on predicted grain morphology in thin-wall Ti-6Al-4V deposits in Ref. [94].

The microstructure in the deposited part is very complicated because it undergoes a near rapid solidification process and several solid state phase transformations when cooling to room temperature. Due to the lack of re-crystallization of the last layer in the multi-layer deposition of the LENS process, the microstructure of the last layer differs from the rest of the layers. Cellular, as well as dendritic structures, have been observed in the deposition layers [81, 89, 96, 97]. A dendritic structure was usually found in last layer while a dendrite/cell structure was found in the previous layers [72, 74, 76, 80, 83, 84, 98]. Columnar dendrites were observed in the last layer with AISI316 [74]. The cell structure of AISI316 after cooling down to room temperature was also obtained [98] as Figure 1.8 shows. A dendritic microstructure can also occur in layers other than the last one. The top layer showed a mainly dendritic structure, and this structure was also observed at layer boundaries [72] as Figure 1.9 shows. It can be identified that the microstructure of the last layer differs from others partly because all other layers are tempered during deposition of the next layer except for the last one. All the above reports provide clear evidence that dendritic structures can occur during the solidification in the LENS process.

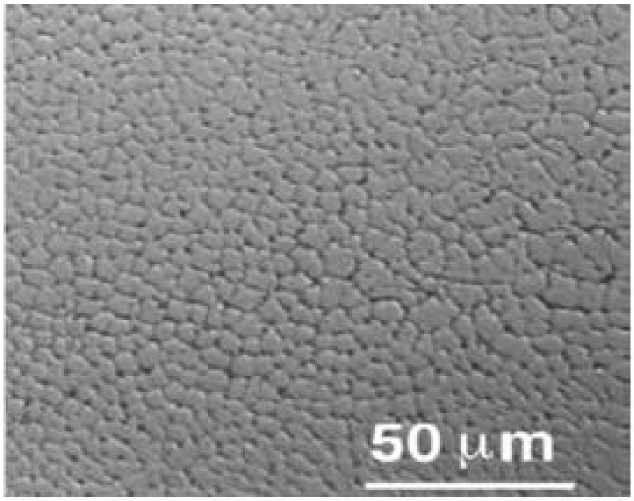

Figure 1.8 AISI316 typical cellular microstructure found in recrystallized layers [98]

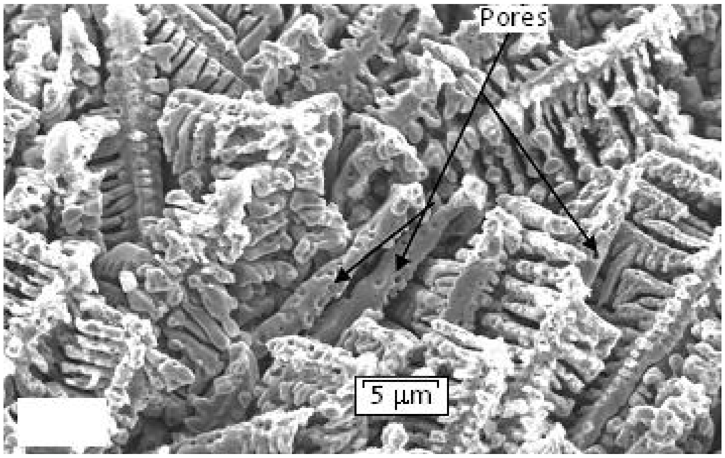

Figure 1.9 AISI316 fine dendritic structure found in the top layer [72]

1.6.3 Simulation of microstructure evolution

Kurz [7] developed a model on microstructure mapping in processes with a clear character of directional solidification such as was observed in laser surface treatment and laser welding. Pavlyk and Dilthey [99] simulated the dendrite morphology for arc welding and calculated a stable dendrite structure with a PDAS of 10-15μm. Simulation on 106×106 grid points took 2×10^5 time steps. And a cell size of about 0.1μm was used, which was more than one order of magnitude smaller than that the dendrite tip radius and the diffusion length.

Very few papers published the results on the microstructure simulation on the LENS process. Miller *et al*. [100] developed a 3D model with the Monte Carlo method to simulate the microstructure evolution, but only obtained the cell grain microstructure, and also Grujicic *et al*. [19] calculated the columnar grain evolution of solidification microstructure in the LENS rapid fabrication process with CA method, but without dendrite details.

1.6.4 Review of solidification modeling

In earlier times, most of the solidification problems were solved by analytical solutions with simple geometries due to the constraints in the available computational tools. The occurrence of computer numerical methods were adopted, but constrained to one diffusion equation because of the limited power of computer. Then multidimensional models have been developed to deal with multi-physics phenomena with the advanced and powerful computers in the past few decades. Several articles reviewed the solidification simulation. Hu and Argyropoulos [101] summarized the macro energy transport models during the solidification and analyzed the relative merits and disadvantages of each formulation. Rappaz [102] introduced the basic concepts of macroscopic and microscopic phenomena which entered normally into any solidification process. The mechanism of microstructure formation was outlined for both eutectic and dendritic alloys solidified with equiaxed and columnar morphologies. Stefanescu [103] classified the prediction method of microstructural evolution as being the continuum approach (deterministic), or on the stochastic (probabilistic) approach, or, more recently, on a combined approach. The prediction of microstructure evolution was analyzed based on the solid/liquid transformation during the solidification. Boettinger *et al*. [104] discussed the most important advances in solidification science and technology and summarized the advent of new mathematical techniques (especially phase field (PF) and cellular automata (CA) models) coupled with powerful computers to simulate grain growth and final microstructure evolution. A most recent review [105] revealed that the recent popular research on solidification science places extra emphasis on (1) key anisotropic properties of the solid-liquid interface that governed solidification pattern evolution, including the solid-liquid interface free energy and the kinetic coefficient and (2) dendrite solidification at small scale (atomic scale) and at large growth rates, with particular emphasis on orientation selection and/or under complex conditions (fluid flow).

1.7 Simulation methods for solidification microstructure evolution

The emergence of simulation methods enables prediction on grain structure and morphological evolution. In the last decade, numerical simulation has been widely used to predict microstructural changes during solidification. Various types of deterministic and stochastic methods have been applied to characterize the dendritic growth during solidification, including front tracking (FT), PF, LS, and CA methods.

1.7.1 Front tracking method

Some models with FT algorithm were built for solidification problems [106-108]. The main idea of this method is that the interface is identified by an ordered set of marker points located on the interface and is represented by the distance between the points and some reference surface. A line connecting the marker points, usually a piecewise polynomial, represents the front. Three distinct steps are involved, including interface reconstruction and advection (tracking), calculation of normal velocity, and solution of the governing equations.

The first task of this method is to find the points where the interface intersects the Cartesian grid lines. First, identify the points where the interface cuts the vertical lines in the grid (see Figure 1.10), which is termed as marker points. Next, determine the points of intersection of the interface with the other two sets of grid lines, which are referred to as intersection points. Once the interface is advected over time step, new marker points corresponding to the new interface location need to be determined.

The normal velocity V_n of the interface is obtained from the difference between the normal gradients of temperature in the liquid and solid as latent heat is liberated via the following equation (Stefan condition):

$$\lambda_s \frac{\partial T^s}{\partial n} - \lambda_l \frac{\partial T^l}{\partial n} = \Delta H \cdot V_n \qquad \text{(Eq.1.1)}$$

Where is ΔH enthalpy of freezing, and λ_s and λ_l are thermal conductivity for solid and liquid, and T^l and T^s are interface temperature in liquid and solid.

In order to solve the governing equations in the two phases, a methodology needs to be devised for applying the equations for each of the phases in the interfacial cells. The interfacial cell is partitioned according to the actual position of the interface in the cell, and the equations are solved separately in each phase.

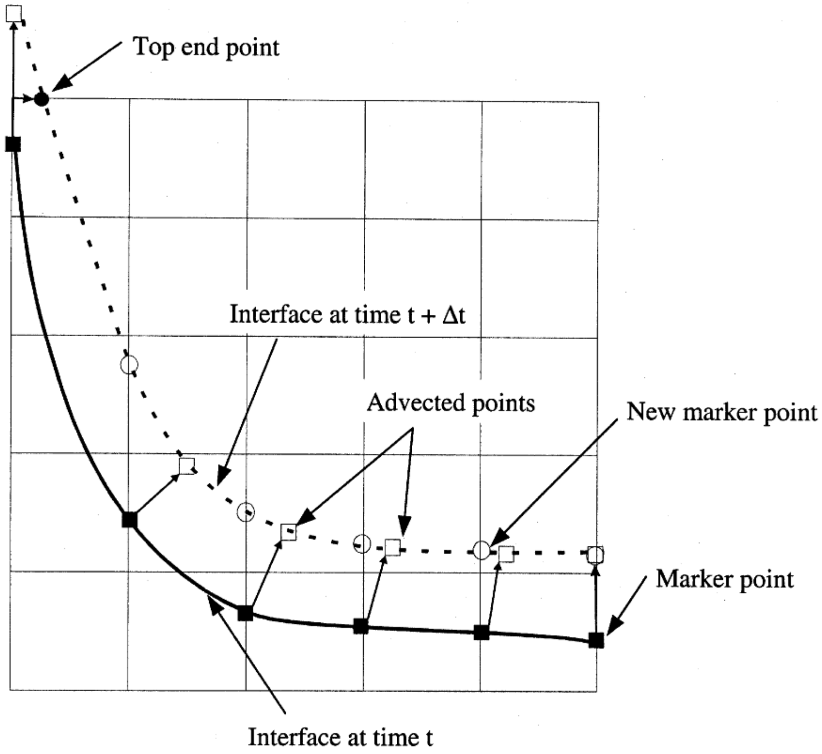

Figure 1.10 Schematic for front tracking method

For the FT method, topological changes like coalescence (merging of two dendrite arms) is difficult to be handled and/or implemented. Besides, this method usually involves fairly large grid anisotropy.

1.7.2 Phase field method

The PF method was firstly developed by J. Langer (1978) [109], and it simulates the microstructure by solving the equations governing the evolution of the PF variable and heat or solute. A field variable, ∅, can describe the real world by identifying the phase of a point in the domain but without physical meaning. If the point lies in the liquid region, $\emptyset = 0$; if the point lies in the solid region,$\emptyset = 1$. Values of $\emptyset$ between zero and one represent points that lie in the interface. The phase variable can be obtained by solving the Kinetics equation:

$$\frac{\partial \emptyset}{\partial t} = -\Gamma \cdot \frac{\delta F}{\delta \emptyset} \quad \text{(Eq.1.2)}$$

Where the Γ is interface kinetic coefficient. The free energy function F is:

$$F = \int_V \left[f(\phi) + \frac{1}{2} \cdot (\varepsilon_{\emptyset})^2 \cdot (\nabla \emptyset)^2 \right] dV \quad \text{(Eq.1.3)}$$

Where the $f(\phi)$ is free energy density and $\varepsilon_{\emptyset}$ is gradient energy coefficient. There are several advantages for this method, including easy to be implemented, capable of reproducing most of the phenomena associated with microstructure formation, but it has its disadvantage, and that is parameter identification and the simulation domain size.

The PF method simulates the phase types by solving differential equations that govern the evolution of the PF variable [110-114]. It has been applied to simulate the microstructural evolution of pure metals [113] and multi-component systems [110, 114]. However, the PF method requires significant computer resources which limits its application because the calculation domain cannot be very large.

The main advantage of this approach is that complex topology changes are easily handled since there is no need to explicitly track the interface or even provide interfacial boundary conditions. The disadvantage of this method is in relating the parameters in the evolution equation for $\emptyset$ to phenomenological parameters such as surface tension and interface kinetic coefficient.

1.7.3 Level set method

Several models [115-117] were also developed to simulate the dendrite growth during solidification. The LS method also constructs a field $\emptyset$ to describe the interface such that at any time t, the interface is equal to the zero LS of $\emptyset$, i.e.,

$$\Gamma(t) = \{x \in \Omega : \phi(x,t) = 0\} \qquad \text{(Eq.1.4)}$$

And the $\emptyset$ is equal to the signed distance function from the interface

$$\phi(x,t) = \begin{cases} +d(x,t), & x \in \Omega^l \\ 0, & x \in \Omega^l \\ -d(x,t), & x \in \Omega^s \end{cases} \qquad \text{(Eq.1.5)}$$

Where the $d(x,t)$ is normal distance of point x from the interface.

At the solid-liquid interface, the motion of the interface moving velocity $\vec{V}$ (see Figure 1.11) is dictated by the classical Stefan equation (energy balance at the freezing front), which can be obtained by:

$$\rho_s \cdot L \cdot \vec{V} = \overrightarrow{q^s} - \overrightarrow{q^l} \qquad \text{(Eq.1.6)}$$

Where $\overrightarrow{q^s}$ and $\overrightarrow{q^l}$ the heat flux at the interface to the solid and to the liquid, which can be obtained by:

$$\vec{q} = \lambda \cdot \nabla T \cdot n \qquad \text{(Eq.1.7)}$$

Where the n is normal direction at the interface.

The idea behind the LS method is to move $\emptyset$ with the correct speed $\vec{V}$ at the interface which is extracted from Eq.1.8.

The interface position is thus implicitly stored in $\emptyset$. And the motion equation governing the $\emptyset$ is given by:

$$\frac{\partial \emptyset}{\partial t} + \vec{V} \cdot |\nabla \emptyset| = 0 \qquad \text{(Eq.1.8)}$$

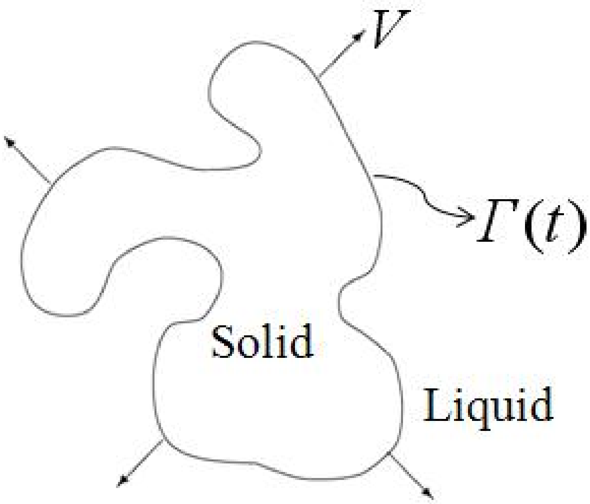

Figure 1.11 Schematic for level set method

The advantages of the LS method include that discontinuities can be naturally handled and computation is accurate enough. The disadvantage is that it still needs to calculate the phase as variable to determine the interface

1.7.4 Cellular automaton method

Another method used to simulate the grain growth is the CA method. This method produces results similar to those of the PF method by obtaining the temperature and solute fields and then determining the solid/liquid (S/L) interface. The CA method was first proposed by Von Neumann and Burks (1966) [118]. Since then, it has had numerous diverse applications, including microstructure evolution during solidification. CA systems consist of a lattice of discrete areas known as cells, and the solidification domain is mapped with a regular arrangement of cells as Figure 1.12 (a) shows [119]. The cells each store their state, which changes in discrete time-steps. For the solidification model, each CA cell has three possible phase types, the liquid, solid, and interface cell as Figure

1.12 (b) shows. The state of a cell at the next time-step is dependent on its current state and the current states of its immediate neighbors.

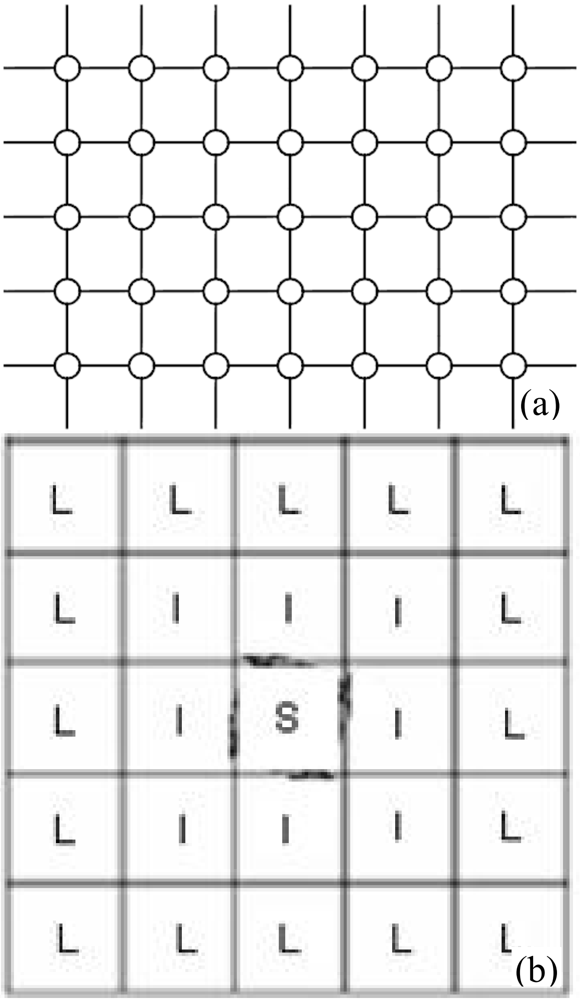

Figure 1.12 (a) Arrangement of CA cells in calculation domain; and (b) three possible phase types for each cell

In the 2D case, three kinds of neighborhood configurations have been defined, including the Von Neumann, Moore, and uniform configurations as shown in Figure 1.13 [120]. The Von Neumann neighbors are the four nearest cells located directly above, below, and to the left and right of the cell, while the Moore neighbors are the cells in all eight directions, including the four nearest cells and four next-nearest cells. The uniform configuration is used for hexagonal lattices, and the uniform neighbors are the all six touching hexagonal cells.

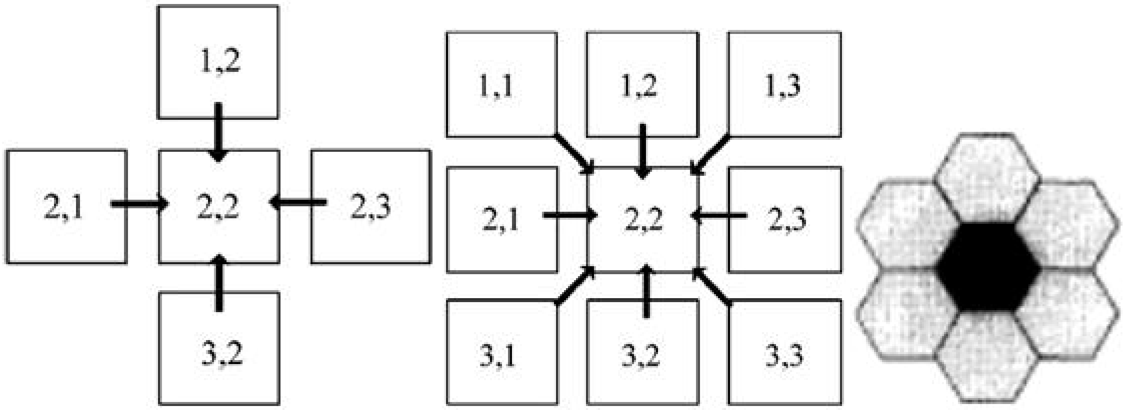

Figure 1.13 Three kinds of neighborhoods from left to right: Von Neumann, Moore, and uniform

A set of rules is defined which determine the conditions upon which the cell will change its state as Figure 1.14 shows [121]. Initially a square representing nuclei to growth is put at the center of cell, and this cell is defined to be interface cell. The length, L_a, determining the growth velocity, depends on the changing of solid fraction. If the corner of this square reaches a neighbor cell, the neighbor cell is changed to be an interface cell. A new solid square is generated in the interface cell, and the center of the square is set at the corner of the original square; the new square, representing new nuclei, starts to grow. After the original square has changed the neighboring cells into interface cells, the original cell continues to grow. If the fraction of solid in the original cell becomes unity, the state of the original cell becomes solid and changes any surrounding liquid cells into interface cells.

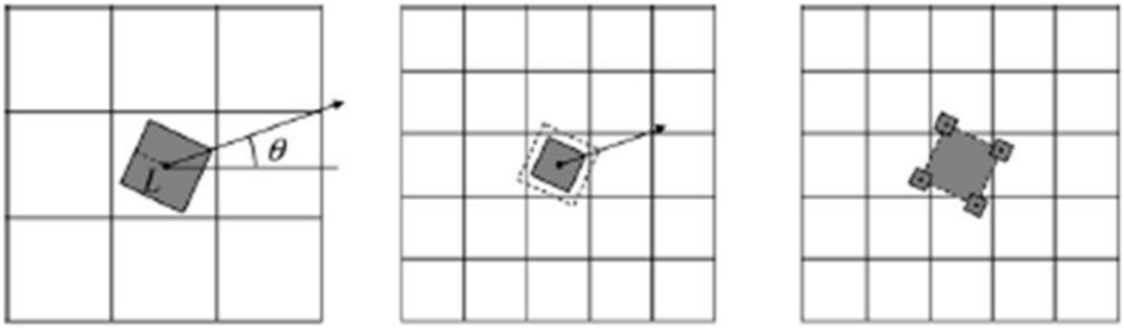

Figure 1.14 Schematic of CA transition rules to capture interface cells

$$L_a^{t+\Delta t} = L_a^t + \Delta f_s \cdot a \qquad \text{(Eq.1.7)}$$

Where Δf_s is the increasing of solid fraction, a is the size of the cell, and L_a is the distance between the center and the side of the solid square.

As just mentioned, the calculation domain is mapped with cells, and usually there are many grains in the domain, and each grain is described by different sets of cells as Figure 1.15(a) shows, but only those located at the boundary (i.e. in contact with liquid cells) being active for the calculation of the growth process as shown in Figure 1.15(b) [122]. The states of all cells are updated synchronously during each time-step, producing an overall change in the lattice.

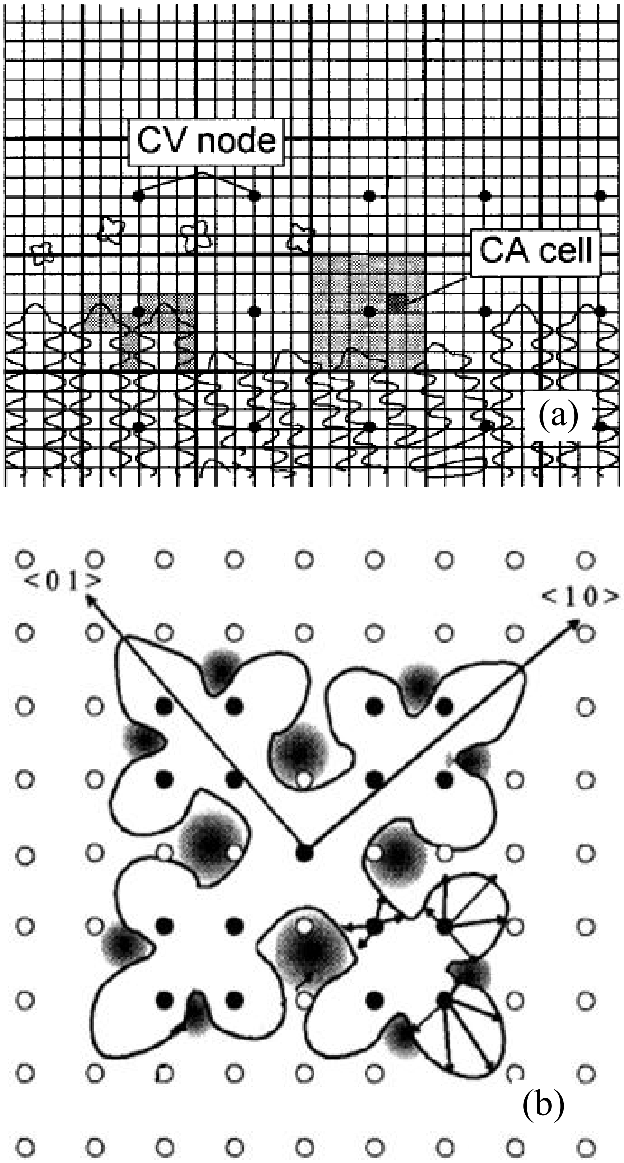

Figure 1.15 (a) Dendrite being described with a set of cells; and (b) the only the cell at interface being active for growth calculation

The CA method can treat arbitrary grain shapes, and it is also well adapted to describe the grain competition growth, morphology transition, and the merging between two arms. However, this method has the difficulties of the artificial anisotropy introduced by the CA mesh.

1.8 Previous solidification modeling with CA technique

Many CA models were built to simulate the solidification of alloys [123-154]. Rappaz and Gandin [133, 134] developed a 2D probabilistic model to simulate the dendritic grain formation during solidification based on the CA technique. They coupled the CA algorithm and FE method to obtain the thermal field and the microstructure of an Al-Si alloy, but this work did not provide the details of the growing process of dendritic grain. Sanchez and Stefanescu [135] developed a dendrite growth model which proposed a solution for the artificial anisotropy, but the dendrite could grow only aligned with the mesh or in a 45-degree orientation. Then improved models [136, 137] were proposed by introducing a new virtual FT method, which was able to simulate dendrites growing in any preferential orientation. Zhu and Hong [138] developed a CA model to simulate the solidification microstructure of both eutectic and hypoeutectic Al-Si alloy and provided good insight into the eutectic nucleation and growth behaviors. They [122] also applied this model to simulate the evolution of dendritic structures in competitive growth of columnar dendrites in the directional solidification of alloys and metal mold casting. Wang and Nakagawa *et al*. [121, 130] developed the dendrite growth models using a modified FT technique with new growth algorithm to capture the solid/liquid interface cell, thus to simulate the dendrite growth with consideration of preferential crystallographic orientation of a dendrite.

Some articles [139-142] simulated the columnar-to-equiaxed transition (CET) during the directional solidification of alloys by a solute diffusion controlled dendritic solidification model with coupled CA technique-FD or FE methods.

Later, a CA model which considered the influence of fluid flow on the dendrite growth was also developed [143-145] with constant and uniform inlet flow velocity imposed on one side to discuss the growth features under convection, finding that the tip growth velocity increased in the upstream direction with an increase of the inlet flow velocity. Mullis [146] built a model to evaluate the effect of fluid flow orthogonal to the principal growth direction on the dendritic growth, finding that such a flow caused rotation of the tip due to thermal/solutal advection.

In addition to these 2D simulations, several 3D models [121, 147-154] were also reported, which combined the CA and FE methods to simulate the dendritic growth in binary alloys controlled by solute diffusion. Chang *et al*. [151] developed a 3D solidification model to simulate the dendritic grain structures of gas atomized droplets in a non-uniform temperature field on the basis on combined CA technique and the FV heat flow calculation. Gandin *et al*. [152] proposed a 3D model coupled CA and FE model to calculate the final grain structure for super alloy precision castings. Zhu *et al*. [153] developed a three dimensional CA model to calculate the microstructures evolution with competitive dendritic growth in the practical solidification of alloys casting. Lee *et al*. [154] built a 3D multiscale model coupled CA technique for microscale component diffusion with FE method for macroscale heat transfer to simulate the grain growth and microstructure evolution and thus predicted the microporosity and microsegregation.

1.9 Research objectives and dissertation structure

Dendrite growth is the primary form of crystal growth observed in the laser deposition process. The properties of metallic alloys strongly depend on their microstructure. Understanding and controlling the dendrite growth is vital in order to predict and achieve the desired microstructure and hence the mechanical properties of the laser deposition metals. So the objective of this work is to develop a solidification model, which couples the FE method and CA technique to predict the dendrite growth in the molten pool during the LENS process. For this research:

Chapter II presents model development for the calculation of the temperature distribution during deposition of multiple layers of AISI410. The calculation results with this 2D model are analyzed and compared with those by the 3D model developed by Wang *et al*. [28].

Chapter III presents the macro-solidification model development to understand the heat/mass transfer and fluid flow during the LENS deposition of stainless steel AISI410. Simulation results on fluid flow with buoyancy forces are compared to those with considering the surface tension caused by temperature gradient.

Chapter IV presents the simulation on solidification microstructure evolution during the LENS process with deposition of a single layer of Fe-0.13wt%C. DAS and dendrite morphology are predicted, and the influence of LENS process parameters on the dendrite growth is also discussed.

Chapter V presents the modeling of dendritic growth for binary Mg-8.9wt%Al alloys with HCP structure during the solidification. Hexagonal shape mesh is generated, and the simulation dendrite morphology is predicted with perfect six-fold symmetry. The impact factors on dendrite morphology, including cooling rate, undercooling, surface tension, and anisotropy coefficient are discussed.

Chapter VI presents 2D lattice Boltzmann (LB)-CA model to simulate the temperature field, solute concentration, fluid flow, and dendrite growth. LB method is adopted to simulate the solute distribution and fluid flow, and CA is used to predict the dendrite growth.

Chapter VII summarizes the results of the work performed in this research, and recommendations for future research are also presented.

CHAPTER II

TWO-DIMENSIONAL THERMAL MODEL FOR LENS PROCESS

2.1 Introduction

It is critical to understand the local thermal cycles and temperature history since it partly determines the final microstructure and thus the mechanical properties of the LENS components. Many experiments and simulations (including 2D and 3D models) have been done to characterize the thermal behavior during LENS deposition. But no work has been done to compare the results from 2D and 3D models.

As with most 3D models, the computational time greatly exceeds that of equivalent 2D models. This is even so when only simple heat conduction is being calculated. The computational cost of a 3D model becomes impractical when more complex phenomena of interest are simulated, like solidification, segregation, porosity, molten pool convection, solid phase transformations, strain and stresses, and others. The single-wall build, in which a thin plate is deposited layer by layer, is the geometry of choice to study the LENS process because of its relative simplicity for modeling and experimental trials. The fact that both 2D and 3D models have been used in the literature to simulate this simple geometry indicates that it is not clear whether a 2D model can capture the thermal phenomena of interest. The situation has not been analyzed and, when in doubt, authors resort to 3D modeling at the expense of analysis time and simplified physics. Because the thermal history is the key to predict microstructure and mechanical response, the determination of the conditions under which a 2D model can be used to calculate the temperature field with acceptable accuracy would be very useful to undertake combined numerical/experimental studies of the LENS process that go beyond thermal-only aspects.

In this chapter, a 2D FE model is developed to calculate the temperature distribution during deposition of multiple layers of AISI410. The thermal characteristics and molten pool size predicted with this 2D model is then compared with those calculated with the 3D model developed by Wang *et al*. [28] and with experimental data. The experimental data of temperature/coolingrate need compensation to obtain the correct thermal results; however, the cooingrate was obtained by consecutive temperature at curtain time interval in the simulation. The conditions under which the 2D simulations produce acceptable results are identified, as well as the cases in which 3D effects cannot be captured by the 2D model. The influence of the idle time between the depositions of consecutive layers of material and of substrate size on the thermal cycle/history is also illustrated.

2.2 Two dimensional FE model

2.2.1 Model description

A 2D FE model is developed to simulate the transient temperature field during the deposition of ten consecutive layers of a single-wall plate of AISI410. The schematic of the geometry is shown in Figure 2.1(a). A fixed FE mesh is constructed for the substrate and the ten layers of the plate. A uniform layer thickness is used whose value is set consistently with the powder deposition rate and the travel speed of the laser/nozzle head. Initially, the substrate is at room temperature, and the layer elements are inactive. When a new layer is being deposited, the elements of that layer are activated and they remain active for the rest of the simulation. The initial temperature for the new layer being deposited is above the melting temperature, and which means the injecting melt powder is supposed to be totally melted. The boundary conditions (Figure 2.1(b)) include convection heat loss on the top and sides, a prescribed temperature at the bottom of the substrate, and convection/radiation on the top plus a heat flux due to the incident laser power. The boundary conditions are updated dynamically as layers are activated and new sections of the boundary become active. After finishing depositing one layer and before beginning depositing the next layer, there is a time interval called the idle time, during which the laser/nozzle head is returned to the left end of the plate, so that all layers are deposited from left to right. During the idle time, the laser and powder injection are turned off and the corresponding heat flux boundary condition is inactive.

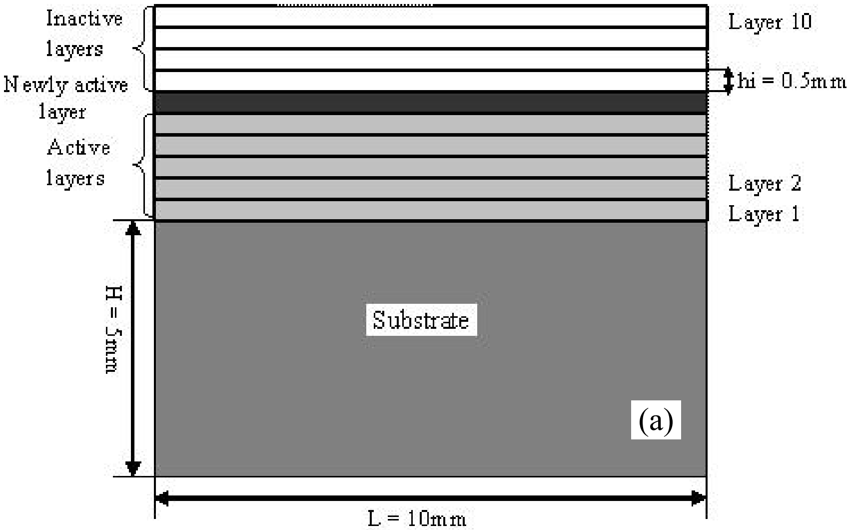

Figure 2.1 (a) Sketch of element activation to illustrate the laser powder deposition with multi-passes, (b) schematic of the model showing the boundary conditions used for the temperature calculation, (c) 3D model of Ref. [28]

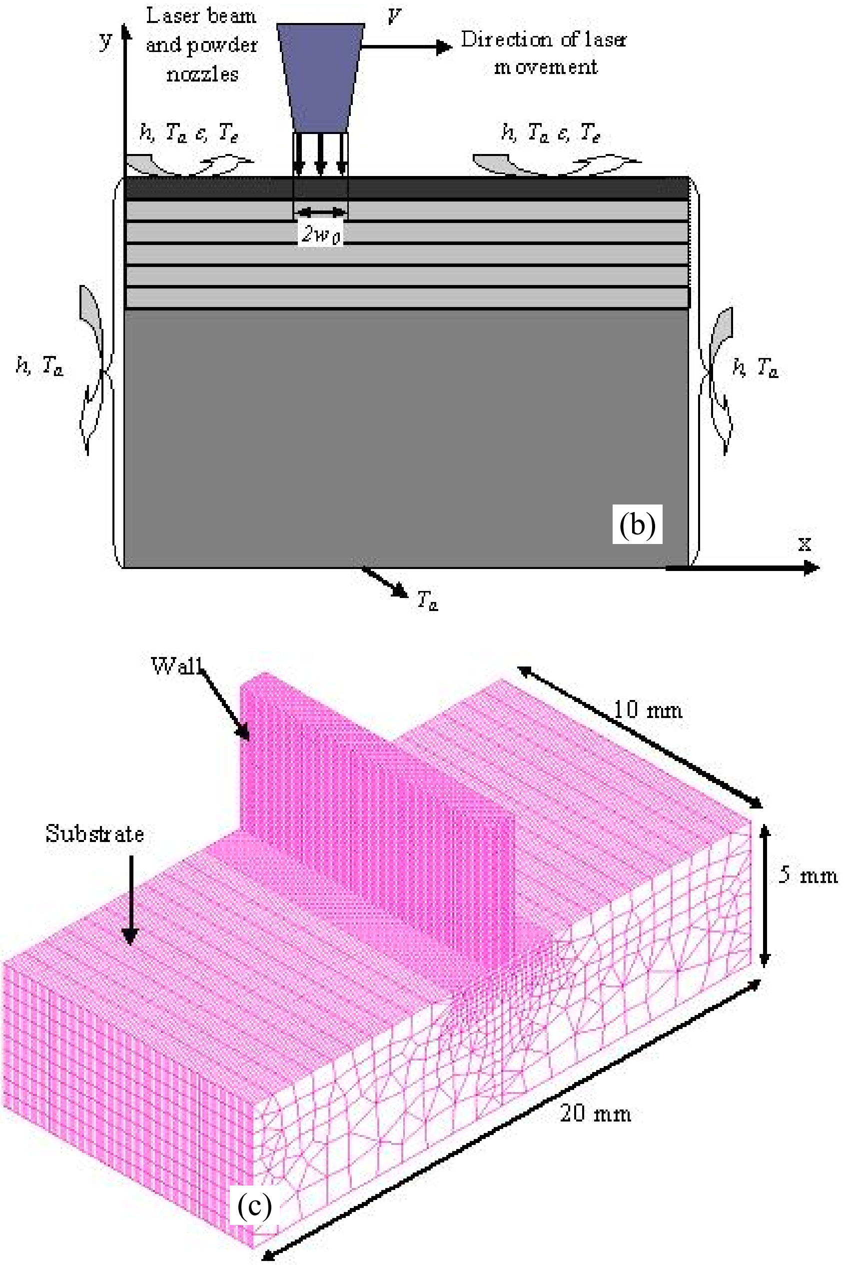

Figure 2.1 (Continued)

In order to compare the results of the 2D model with those from the 3D model by Wang *et al*. [28], the same material properties and process parameters are employed. The plate is built by depositing 10 layers of material, each with a length of 10.0mm and a height of 0.5mm, on top of a substrate with dimensions 5.0mm high and 10.0mm long.

For comparison purposes, the geometry of the 3D model of Ref. [28] is shown in Figure 2.1(c). The travel speed of the laser beam is 7.62mm/s, and the laser beam moves from left to right for each layer deposition. AISI410 was used for both the deposited plate layers and the substrate. The thermal properties of AISI410 used in this model are presented in Table A.1 in Appendix A.

2.2.2 Heat transfer equation

The 2D transient equation of heat conduction describing the heat transfer within the plate during the LENS process is:

$$\frac{\partial T}{\partial t} = \alpha \cdot \left(\frac{\partial^2 T}{\partial x^2} + \frac{\partial^2 T}{\partial y^2}\right) - \frac{L}{C_p}\frac{\partial f_l}{\partial t} \qquad \text{(Eq.2.1)}$$

Where T is temperature, t is time, x and y are the horizontal and vertical coordinates, respectively; α is the thermal diffusivity, L is the latent heat of melting, C_p is the specific heat, and f_l is the fraction of liquid, approximated as $f_l = (T - T_s)/(T_l - T_s)$, where T_l is the liquidus temperature and T_s is the solidus temperature of the alloy.

2.2.3 Initial and boundary conditions

The boundary conditions are shown in Figure 2.1(b). A forced boundary condition is prescribed on bottom of the substrate:

$$T(x, y, t)|_{y=0} = T_a \qquad \text{(Eq.2.2)}$$

Where T_a is the ambient temperature around the part, and in this work it was considered to be equal to the room temperature. The initial temperature of the substrate is also assumed at room temperature:

$$T(x,y,t)|_{t=0} = T_a \qquad y \leq H \qquad \text{(Eq.2.3)}$$

The initial condition of the newly deposited material for each layer is set equal to the melting temperature:

$$T(x,y,t)|_{t=0} = T_a \qquad y > H \qquad \text{(Eq.2.4)}$$

The boundary condition on the section of the top layer under the laser beam is [28]:

$$-\lambda \cdot \frac{\partial T}{\partial y} = h(T - T_a) + \varepsilon\sigma(T^4 - T_w^4) - Q_r \qquad \text{(Eq.2.5)}$$

Where k is the thermal conductivity, h is the convective heat transfer coefficient, ε the emissivity of the part surface, σ the Stefan-Boltzmann constant [$\sigma = 5.67\times10^{-8}$ W/m^{2}K^4], and T_w the temperature of the internal wall of the glove box (taken equal to T_a in this work). In Eq.2.5, Q_r is a distributed heat source with a Gaussian profile:

$$Q_r = A_0 \cdot \exp(-\frac{2(x-x_0)^2}{{w_0}^2}) \qquad \text{(Eq.2.6)}$$

Where $A_0 = -(2a_eP_l)/(\sqrt{2\pi}w_0)$ being a_e is the effective absorption of the laser beam energy, P_l the laser beam power, w_0 the beam radius, and x_0 the x coordinate of the laser-beam axis. Because a_e and w_0 are constants, in this model, different Q_r was obtained by changing A_0.

The boundary condition for the new elements of the top surface, other than the elements beneath the laser beam, considers only the effects of convection and radiation heat loss:

$$-\lambda\frac{\partial T}{\partial y} = h(T - T_a) + \varepsilon\sigma(T^4 - {T_w}^4) \qquad \text{(Eq.2.7)}$$

For the two vertical sides, heat loss due to heat convection is assumed:

$$-\lambda \frac{\partial T}{\partial x} = h(T - T_a) \quad x = L \qquad \text{(Eq.2.8a)}$$

$$+\lambda \frac{\partial T}{\partial x} = h(T - T_a) \quad x = 0 \qquad \text{(Eq.2.8b)}$$

Where L is the width of the plate. Because of the limitation of 2D modeling, it is not possible to establish a direct correlation between the actual 3D absorbed power distribution and the idealized 2D power profile used in this work. Ye *et al*. [155] investigated the thermal behavior in the LENS process with the FE method. In their work, the temperatures of the nodes where the laser beam focused on were set as the melting point temperatures, thus the laser power did not actually play a role. In this study, the coefficient A_0 is determined by matching the maximum calculation temperature in the molten pool with the measured value reported by Hofmeister *et al*. [16]. By using a 2D model, it is also assumed that there is no significant heat loss through the front and back surface of the part. The time evolution of the isotherms is calculated as the laser beam travels across the top surface of the part and layers are deposited. The model dynamically updates the thermal boundary conditions with laser position and newly added layers; hence it is able to calculate temperature profiles both far of and near the side edges of the plate.

2.3 Results and discussions

In lack of available experimental data with AISI410, I use the experiments of Hofmeister *et al*. [16] for correlation purposes. In these experiments, ultra high speed digital imaging techniques were employed to analyze the image of the molten pool and the temperature gradient on the surface surrounding the molten pool in AISI316 samples fabricated using LENS. AISI316 and AISI410 have similar thermal properties and in my calculations, I use computational process parameters that approximated the conditions of Hofmeister's experiments. To compare the 2D model with the Hofmeister's measurements, a first calculation is performed for the deposition of the top layer (the 10th layer), using the experimental temperature data as initial condition for the previously built layers.

Figure 2.2 shows the temperature contours when the laser beam is at the center of the top layer. The travel speed of the laser beam is 7.62mm/s. It is observed that the temperature profiles predicted by the 2D model and the 3D model of Ref. [28] are very similar. The size of the molten pool predicted by the 2D model (Figure 2.2(b)) is a slightly larger than the one predicted by the 3D model (Figure 2.2(a)) because the heat loss along the z direction is not considered in the 2D model. Figure 2.2(c) shows the profile of temperature and cooling rate from the center of the molten pool to a position 4mm away opposite to the laser moving direction (indicated in Figures 2.2(a-b)). The temperature profile calculated by the 2D model qualitatively agrees with the experimental data of Ref. [16] and with the results calculated by the 3D model of Wang *et al*. [28]. However, the 2D model predicts two small kinks in the temperature and cooling rate curves which are missed by the 3D model, but are consistent with the trend shown in the experiment data. The location of these kinks corresponds to a very thin mushy zone surrounding the molten pool and consequent effect of the latent heat of fusion. The 3D model of Ref. [16], based on the commercial software SYSWELD, did not include latent heat effects and hence could not capture this trend.

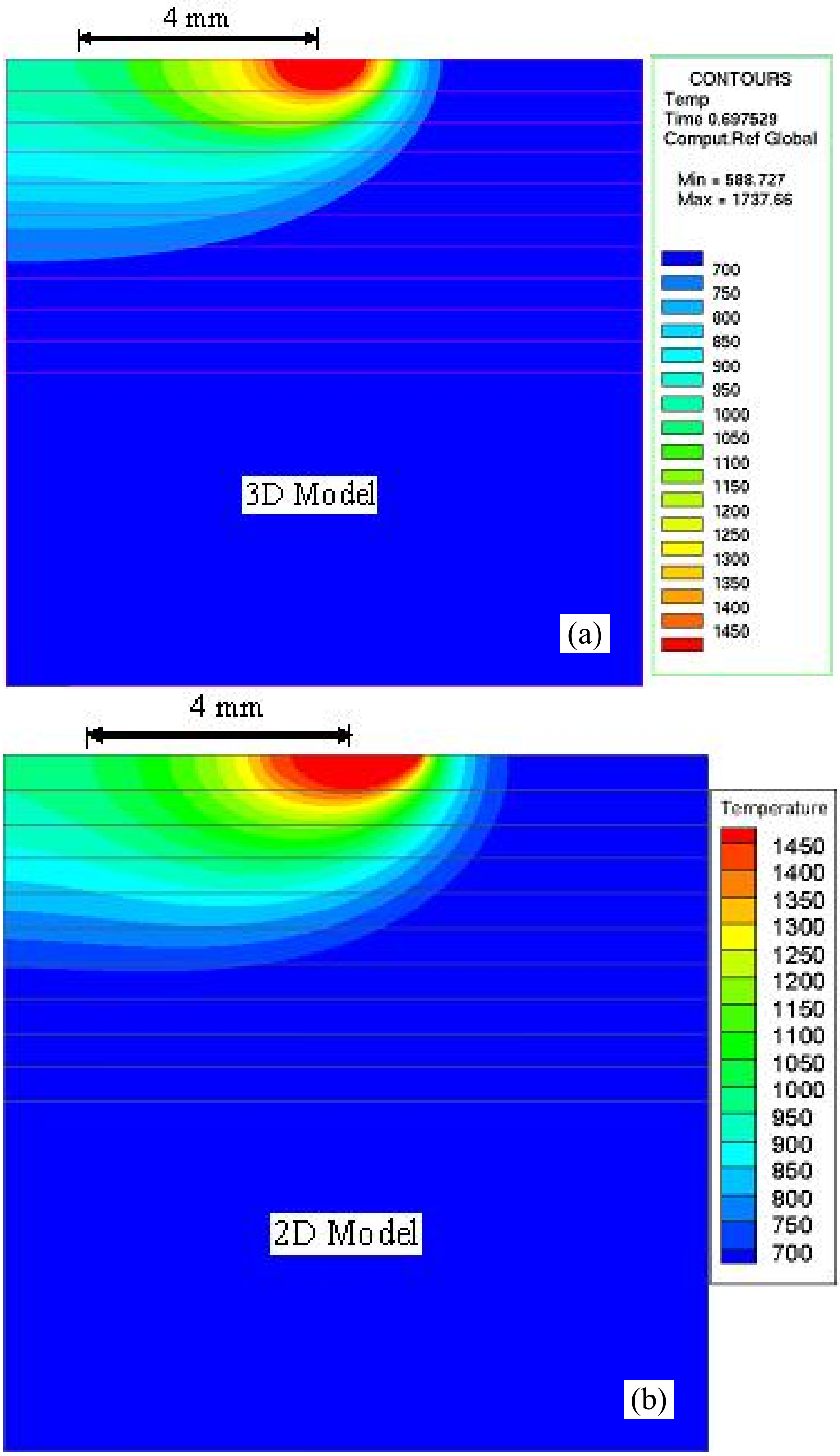

Figure 2.2 Temperature distribution predicted by (a) the 2D model and (b) the 3D model. Molten pool is indicated by the 1450°C isotherm, (c) Comparison of calculated results by the 2D and 3D models and experimental data of Hofmeister *et al*. [16]

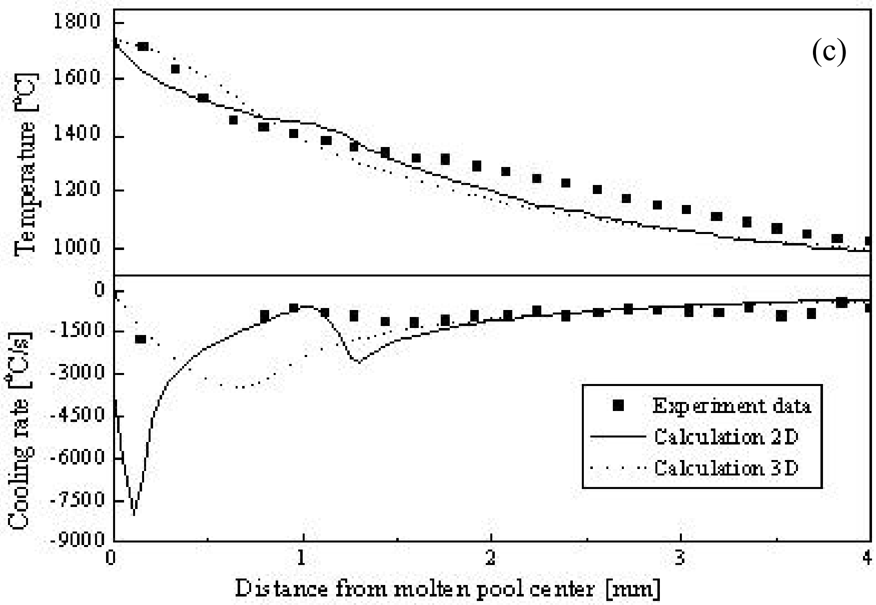

Figure 2.2 (Continued)

In the next simulations, I compare the 2D and 3D models for multilayer deposition for three different travel speeds of the laser beam. In the 3D simulations of Ref. [28], the power program during the deposition of different layers was optimized to obtain a steady molten pool size. In order to reproduce this feature with a 2D model, the power coefficient A_0 needs to be selected accordingly. For each travel speed, the power coefficient A_0 is first determined by matching the maximum temperature in the mid-point of the first layer with the one calculated by the 3D model. For subsequent layers, I assume that A_0 follows the same profile of the power curve of the 3D model, which was optimized for steady pool size. The A_0 – curves for different travel speeds as a function of layer number are shown in Figure 2.3(a). As explained in Ref. [28], in order to maintain the same pool size from layer to layer, the applied power must decrease as layers are deposited in order to compensate for the heating of the part and less heat loss to the substrate. The corresponding temperature profiles along the plate centerline, calculated with the 2D and the 3D models, are indicated for three different travel speeds in Figure 2.3(b), at the time when the 10th layer has been deposited. Higher speeds correspond with higher temperature because less time is available for the layers to cool down between laser scans. In Figure 2.3(b), I can observe the consequence of having used the same power profile of the 3D part in the 2D calculation. Because the heat loss in the z-direction is not considered in the 2D model (and particularly, the heat loss from a 3D substrate), the temperature of the lower portion of the part becomes hotter as layers are deposited, in comparison with the 3D plate. At the end of the deposition of the 10th layer, the bottom temperature of the 2D plate has increased to 600°C, while the 3D part remained at 200°C. For the upper layers, the temperature is more sensitive to travel speed, but the temperature difference between the 2D and 3D parts becomes less pronounced as the dissipation of the substrate is less dominant.

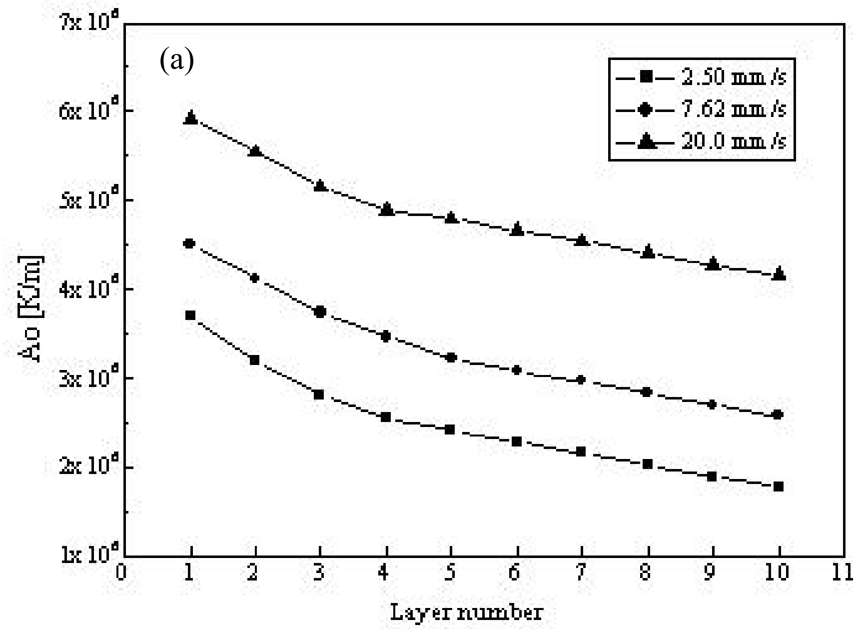

Figure 2.3 (a) Profiles of the A_0 power coefficient of 2D model. (b) Temperature profiles calculated by the 2D and 3D models along the plate centerline for various scanning speeds of the laser beam

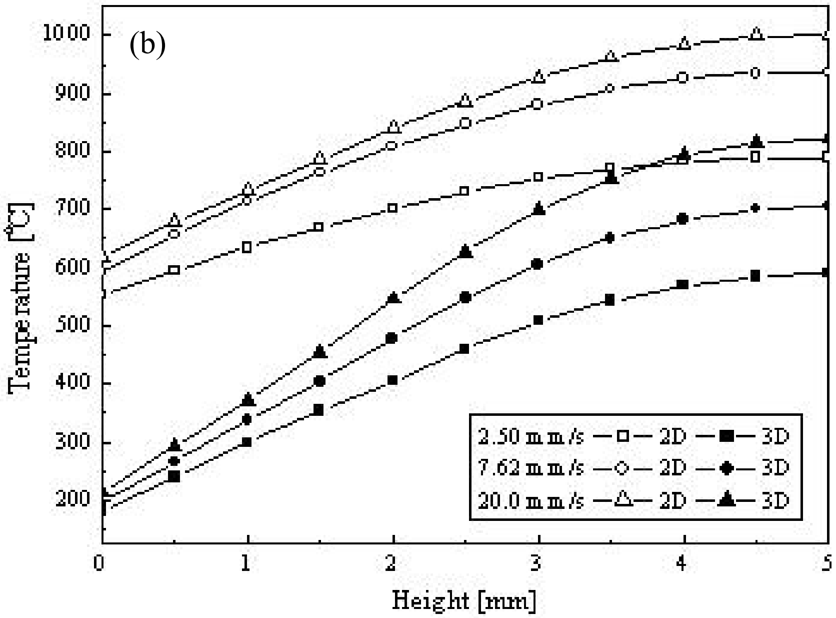

Figure 2.3 (Continued)

Figures 2.4(a) and (b) show the temperature contours in and around the molten pool for layers number 2, 4, 6, 8, and 10, predicted by the 2D and 3D models, when the laser is at the mid-point of the layer. The laser travel speed is 7.62mm/s. The molten pool size of the 10th layer is very similar to that predicted by Wang *et al*. [28]. The discrepancy in pool size between the 2D and 3D model increases as it moves down closer to the substrate, as expected from the thermal profiles observed in Figure 2.3.

Figure 2.4(c) shows the thermal cycles at the mid-points of deposited layers 1, 3, 5, and 10 for the 2D model. Figure 2.4(d), extracted from Ref. [28], shows the same cycles calculated with the 3D model. The temperature of each layer reaches a peak every time the laser goes over the mid-point of the plate, and then decreases to a minimum value before the laser starts scanning a new layer (the idle time between layers also affects the minimum temperature). The calculated thermal cycles look similar for the 2D and 3D models, with the discrepancies already observed in Figure 2.3, which show higher temperature for the lower layers of the 2D model at the end of the deposition because of the extra heat loss by the 3D substrate. Note also that the cooling part of the cycle curves in the 2D model shows the effect of latent heat, which is missed by the 3D model.

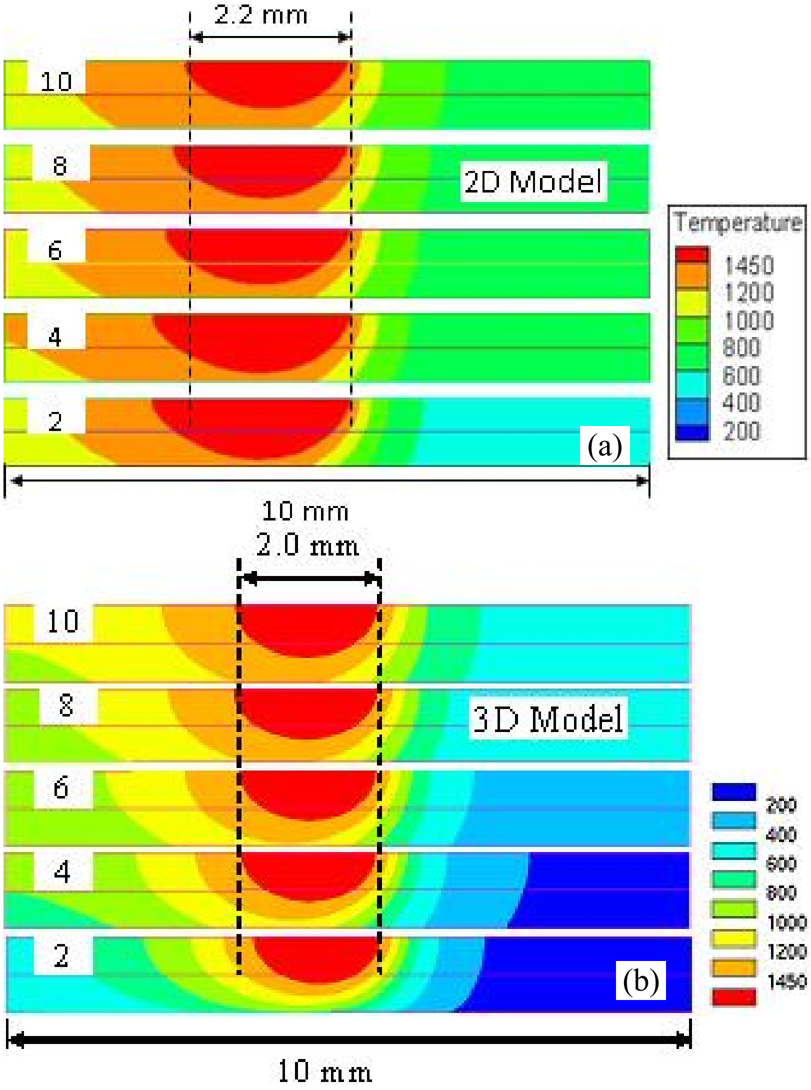

Figure 2.4 Temperature distribution when the laser beam is at the center of layers 2, 4, 6, 8 and 10 calculated by the (a) 2D and (b) 3D models; molten pool is indicated by the 1450°C isotherm. Temperature cycles at the mid-points of layers 1, 3, 5 and 10 as ten layers are deposited for the (c) 2D and (d) 3D models. V=7.62mm/s. In (d), Ms is the martensite start temperature (350°C).

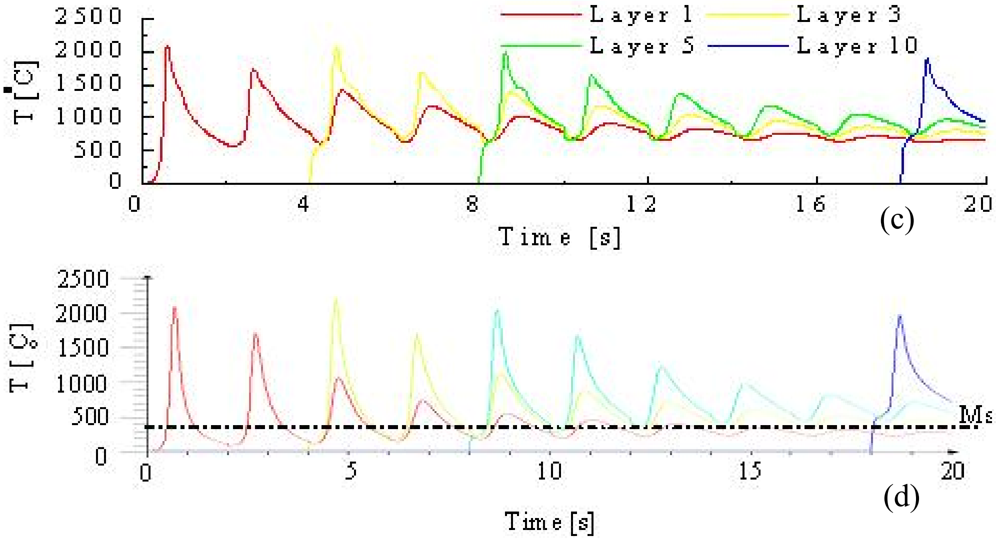

Figure 2.4 (Continued)

A comparison of the temperature contours predicted by the 2D and 3D models is shown in Figure 2.5 for the two other values of travel speed, 2.5mm/s and 20 mm/s, when the laser is at the mid-point of the 10th layer. It is observed that the molten pool size in this layer is very similar for both 2D and 3D calculations, but the 2D substrate is hotter than the 3D one, the difference being more pronounced for higher travel speed. The elongation effect of the pool for higher speed is similarly captured by the 2D and 3D models.

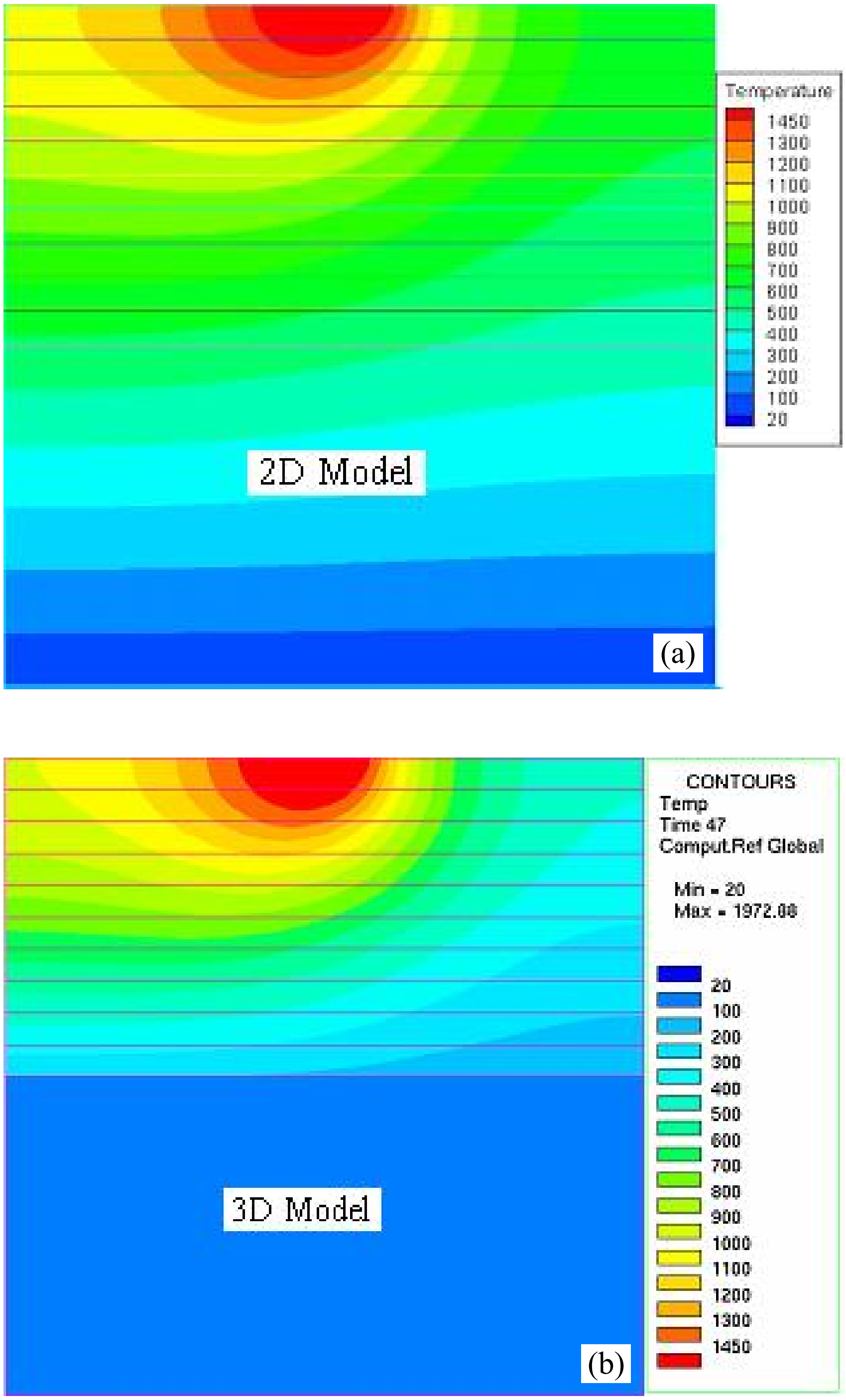

Figure 2.5 Temperature distribution when the laser beam is at the center of the 10th layer as predicted by the (a) 2D model and (b) 3D model for V=2.50mm/s and by the (c) 2D model and (d) 3D model for V=20.0mm/s

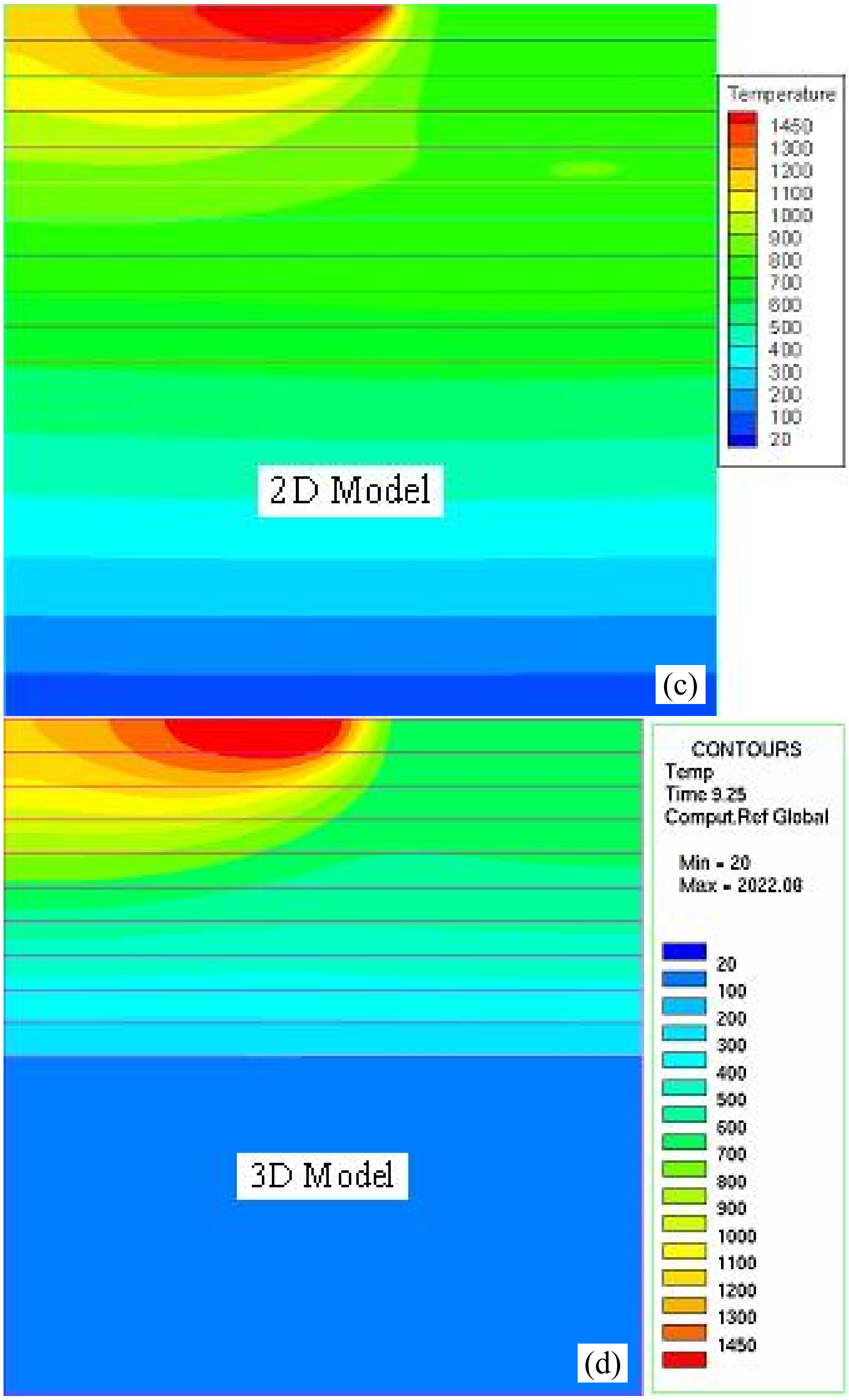

Figure 2.5 (Continued)

Figure 2.6 illustrates the influence of the idle time elapsed between finishing depositing one layer and starting the next layer. Figure 2.6(a) shows the temperature profile along the plate centerline after the 10th layer has been deposited. It is observed that the idle time does not change the shape of the profiles, but only displaces the curves toward lower temperature for longer idle time. The thermal cycles for the case of an idle time of 4.4s are shown in Figure 2.6(b). This figure should be compared with Figure 2.4(c), where the idle time was 0.82s. It can be seen that longer idle time allows the midpoint to cool down to a lower temperature, in particular, below the martensite start temperature (350°C). Hence, idle time can play an important role when trying to control the final microstructure.

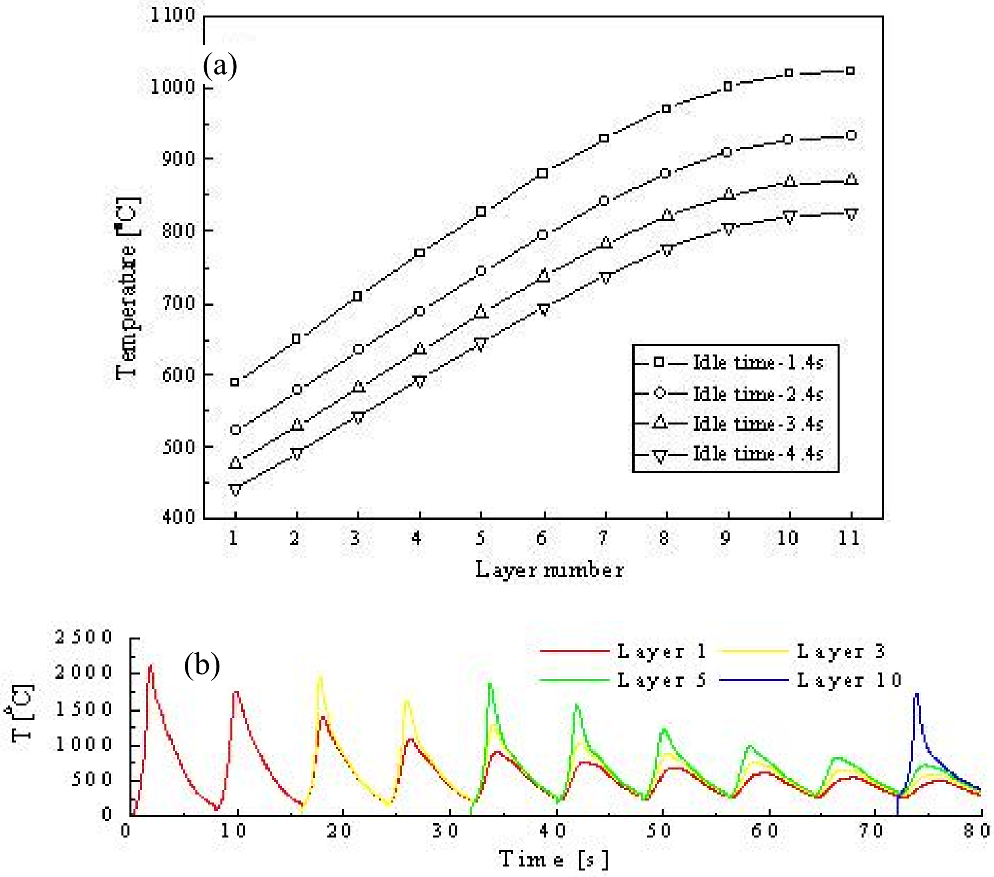

Figure 2.6 (a) Temperature along the plate centerline for four different idle times after the 10th layer is deposited. (b) Temperature cycles at the mid-points of layers 1, 3, 5 and 10 calculated with the 2D model as ten layers are deposited. Idle time is 4.4s, travel speed V=2.5mm/s.

The substrate size has an obvious influence on the thermal cycles of depositions. More heat is lost from a larger substrate, which causes a higher temperature gradient along the height of the plate and leads to a lower average temperature. Because of the restricted heat loss in a 2D substrate, increasing the height of the substrate will lead to the opposite results, i.e., a higher temperature in the part. This is contrary to the prediction of the 3D model and also opposes the results published by Costa *et al*. [24]. Actually, in order to approximate the effect of a larger 3D substrate, either the height of the 2D substrate has to be reduced or a lower temperature must be applied as boundary condition on the bottom of the 2D substrate. The first option is illustrated in Figure 2.7 for a travel speed of 7.62mm/s. Figure 2.7(a) shows the molten pool in different layers for a substrate height of 2mm. Note the smaller pool size compared with Figure 2.4(a), in which the substrate height is 5mm. The temperature profiles along the centerline of the plate are shown in Figure 2.7(b) for different substrate sizes. Observe that a smaller substrate size tends to better approximate the temperature profiles in Figure 2.3(b) calculated with the 3D model.

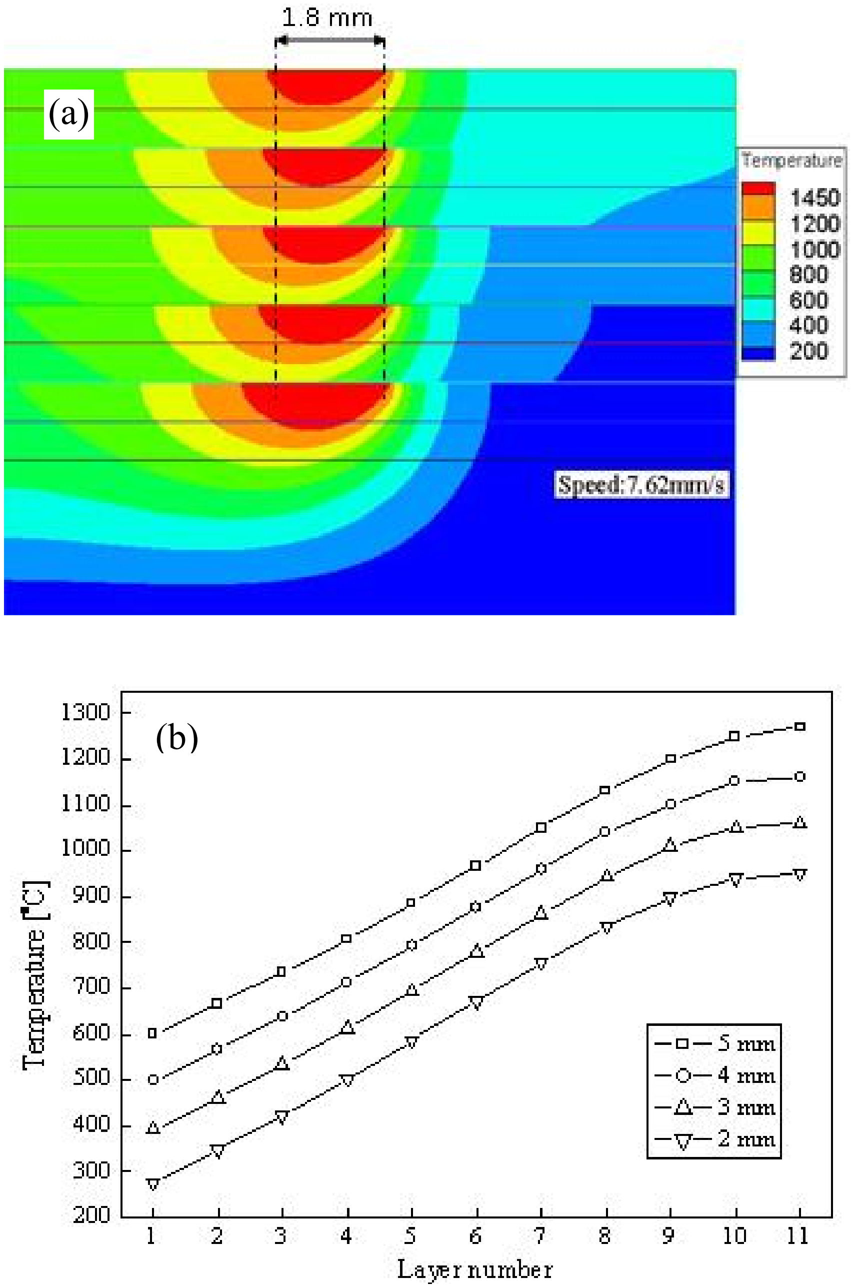

Figure 2.7 (a) Molten pool size and shape when the laser beam moves to the center of the part for layers 2, 4, 6, 8 and 10, with a substrate height of 2mm. (b) Temperature along the plate centerline for four different substrate sizes.

2.4 Conclusions

A 2D FE model was developed to simulate the temperature history during multilayer deposition by the LENS process. The objective of the paper was to investigate the applicability of a 2D model to capture thermal phenomena observed in experiments and previously simulated by commercial software. The deposition of a thin plate made of 10 layers of AISI410 built over a substrate of the same material was analyzed. The temperature distribution, temperature history, molten pool size and shape, and cooling rates were calculated with both the 2D and 3D models, comparing the predicted results under variations of process parameters like laser travel speed, power program, substrate size and idle time. It was found that the 2D model can reasonably reproduce the results of the 3D model for most cases. However, care must be taken when analyzing the optimization of the power program for steady molten pool size, as well as the effect of changes in the substrate size. The higher heat loss produced by the 3D substrate leads to large discrepancies between the two models, particularly at the lower layers of the part. However, it is possible to design an equivalent 2D model that uses a shorter substrate and produces a thermal response of the part similar to the one observed in the 3D model. Because of the inherent savings in computational time of 2D simulations, more phenomena of interest could be added to a LENS model, like solidification, pool convection, segregation and porosity, while still keeping the computational costs at manageable levels. A validated equivalent 2D model can also constitute an improved alternative for online control of the process, which is currently based only on monitoring of the pool size.

The work of this chapter was published in the Journal of Heat Transfer in 2008 [156].

CHAPTER III

MARANGONI CONVECTION AND SOLIDIFICATION DURING LASER DEPOSITION OF AISI410 ALLOY

3.1 Introduction

In recent years there has been much progress in the understanding of heat transfer by both numerical simulation and non-contact temperature measurement techniques during the LENS process [22-24, 28, 50, 155, 157]. However, most of these works were mostly concerned with the heat transfer aspect of the process, while only some studies have been reported to gain insight into the fluid flow phenomena, particularly the flow pattern that occurs in the molten pool. Fortunately, the fluid flow and heat transfer in LENS processes share certain common features with laser welding or laser cladding processes. Therefore, the abundant literature available on these processes can provide useful information about the particular features of LENS fabrication. A number of 2D and 3D numerical models have been developed to understand fluid flow and heat transfer phenomena in welding processes with considering the Marangoni effect, finding that Marangoni flow plays an important role in the heat transfer in the laser welding.

In this chapter, a transient FE solidification model is used to understand the heat/mass transfer and fluid flow during the LENS deposition of AISI410. Surface tension and buoyancy forces are considered for the calculation of transient liquid pool convection. The calculated molten pool dimensions, flow pattern and the profiles of temperature and velocity were compared for different moving speeds of the laser beam, which helps to understand the significance of the various driving forces for the liquid pool convection. The results also reveal the importance of the laser moving speed in the calculation of the flow field in molten pool. In addition, solute transport during solidification is also calculated, revealing the macrosegregation profiles left by the deposition process.

3.2 Numerical model

3.2.1 Mathematical formulation

A 2D FE model is used to simulate solidification in a molten pool under a moving heat source, as shown in Figure 3.1. Several assumptions are made in the model as follows [45]: a) The top surface of the liquid pool can be assumed to be flat; b) The liquid metal is considered an incompressible Newtonian fluid; c) The properties are taken to be different for solid and liquid phases; d) Laser power distributed in a Gaussian manner is applied at the top surface; e) The solid and liquid phases are considered as a continuum medium, and the velocity of the solid phase is zero.

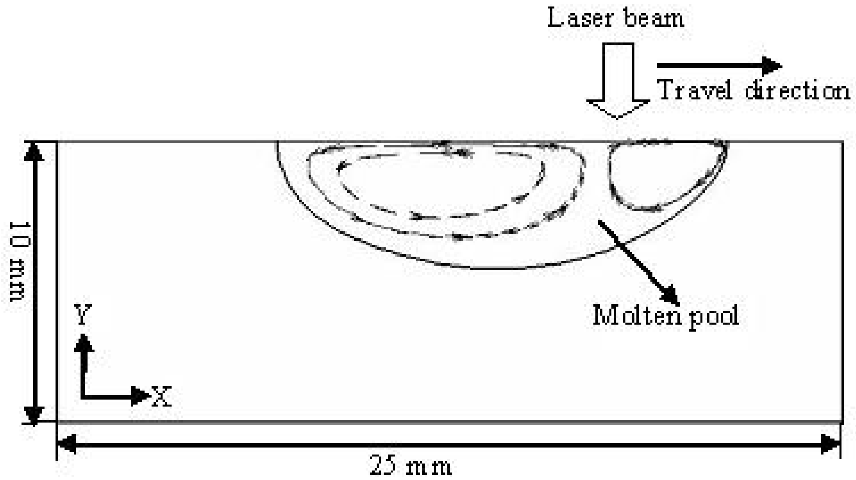

Figure 3.1 Schematic diagram of calculation domain for fluid flow simulation in the molten pool during LENS process

3.2.2 Momentum conservation

With the foregoing simplifications, the equations of continuity and momentum can be written as follows [158]:

$$f_l \frac{\partial}{\partial t}\left(\frac{u_i}{f_l}\right) + \bar{u}\nabla\left(\frac{u_i}{f_l}\right) = -\frac{f_l}{\rho_l}\frac{\partial p}{\partial i} + \mu\nabla^2 u_i + \frac{1}{3}\mu\beta\frac{\partial^2 f_l}{\partial x_i \partial t} - \frac{\mu f_l}{K_i}u_i + \frac{f_l}{\rho_l}\rho g_i \qquad \text{(Eq.3.1)}$$

Where the subscript i refers to the x or y directions, ∇ is the gradient operator, $\bar{u}$ is the superficial velocity, f_l is the liquid fraction, t is time, ρ is density, p is pressure, μ is viscosity, β is the thermal expansion coefficient, K_i is the permeability in the x or y direction, and g_i is the magnitude of gravity in the x or y direction.

3.2.3 Mass conservation

$$\nabla \cdot \bar{u} = \beta \cdot \frac{\partial f_l}{\partial t} \qquad \beta = \frac{\rho_s - \rho_l}{\rho_l} \qquad \text{(Eq.3.2)}$$

3.2.4 Energy equation

$$[\bar{\rho}_s c_s(1-f_l) + \rho_l c_l f_l]\frac{\partial T}{\partial t} - \alpha\nabla^2 T = -\rho_l c_l \bar{u}\cdot\nabla T - \bar{\rho}_s[L + (c_l - c_s)(T - T^H)]\frac{\partial f_l}{\partial t}$$

(Eq.3.3)

Where T is temperature, $\bar{\rho}_s$ is density of solid, c_l and c_s are solute concentration in liquid and solid, respectively, α is the thermal diffusivity, and T^H is the temperature at which the latent heat L is given.

3.2.5 Conservation of solute components

It is assumed that the diffusion of each alloy element in the liquid is simply Fickian, and an equation of solute conservation can be written independently for each one of the alloy solutes. The diffusion in the solid phase is neglected, and each solute has a conservation equation in the liquid:

$$\frac{\partial \overline{C^j}}{\partial t} = \nabla\cdot\left(D^j f_l \nabla c_l^j\right) - \bar{u}\cdot\nabla c_l^j - \beta\frac{\partial f_l}{\partial t}c_l \tag{Eq.3.4}$$

Where $\overline{C^j}$ is the mixture concentration of solute j in solid and liquid and D^j is the diffusivity of solute j.

3.2.6 Initial and boundary conditions

The calculation domain is assumed to be initially at uniform temperature:

$$T(x,y,0) = T_0 \tag{Eq.3.5}$$

On the top surface the heat boundary condition is:

$$-\lambda\cdot\frac{\partial T}{\partial y} = \begin{cases} -A_0\exp\left(-\frac{2(x-x_0)^2}{{w_0}^2}\right) & r \leq r_0 \\ h(T-T_a) + \sigma\varepsilon\left(T^4 - {T_w}^4\right) & r > r_0 \end{cases} \tag{Eq.3.6}$$

Where $A_0 = -(2a_eP_l)/(\sqrt{2\pi}w_0)$ being a_e the effective absorption of the laser beam energy, P_l the laser beam power, w_0 the beam radius, and x_0 the x coordinate of the laser-beam axis. In addition, h is the convective heat transfer coefficient, T_a is the environment temperature, σ is the Stefan-Boltzmann constant [$\sigma = 5.67\times10^{-8}\text{W/m}^2\text{K}^4$], ε is the emissivity of the part surface, λ is the thermal conductivity, and T_w is the temperature of the internal wall of the glove box (taken equal to T_a in this work).

$$T(x,0,t) = T_0 \tag{Eq.3.7}$$

On the lateral surfaces of the model, the heat boundary condition is:

$$-\lambda\cdot\frac{\partial T}{\partial x} = h(T-T_a) \tag{Eq.3.8}$$

3.2.7 The flow boundary condition

At the surface of the weld pool, the Marangoni effect is incorporated by relating the shear stress to the spatial gradient of surface tension as follows:

$$-\mu\frac{\partial u}{\partial z}=\frac{\partial \gamma}{\partial T}\frac{\partial T}{\partial x} \qquad \text{(Eq.3.9)}$$

Where $\partial\gamma/\partial T$ is the temperature coefficient of the surface tension. In this research, the surface tension as a function of temperature is specified as a model parameter, namely the surface tension coefficient. It is important to note that the curvature effects are neglected as a flat weld pool surface is assumed.

3.3 Simulation results

The physical properties of the AISI410 alloy used in the simulations are given in Table A.1 in Appendix A. The thermal properties are the same used in thermal analysis of Refs. [28,159], while the phase diagram information was calculated with Thermo-Calc software.

Figure 3.2(a) shows temperature profiles along the depth direction obtained by experiments and a 3D heat conduction model as described in Ref. [159]. The temperature calculated by the 3D model is comparatively higher than the measured data because the model considered only heat conduction and did not account for the additional heat transfer produced by Marangoni convection. Figure 3.2(b) shows the temperature profiles obtained with the current model under the same process parameters, with and without consideration of Marangoni convection in the molten pool.

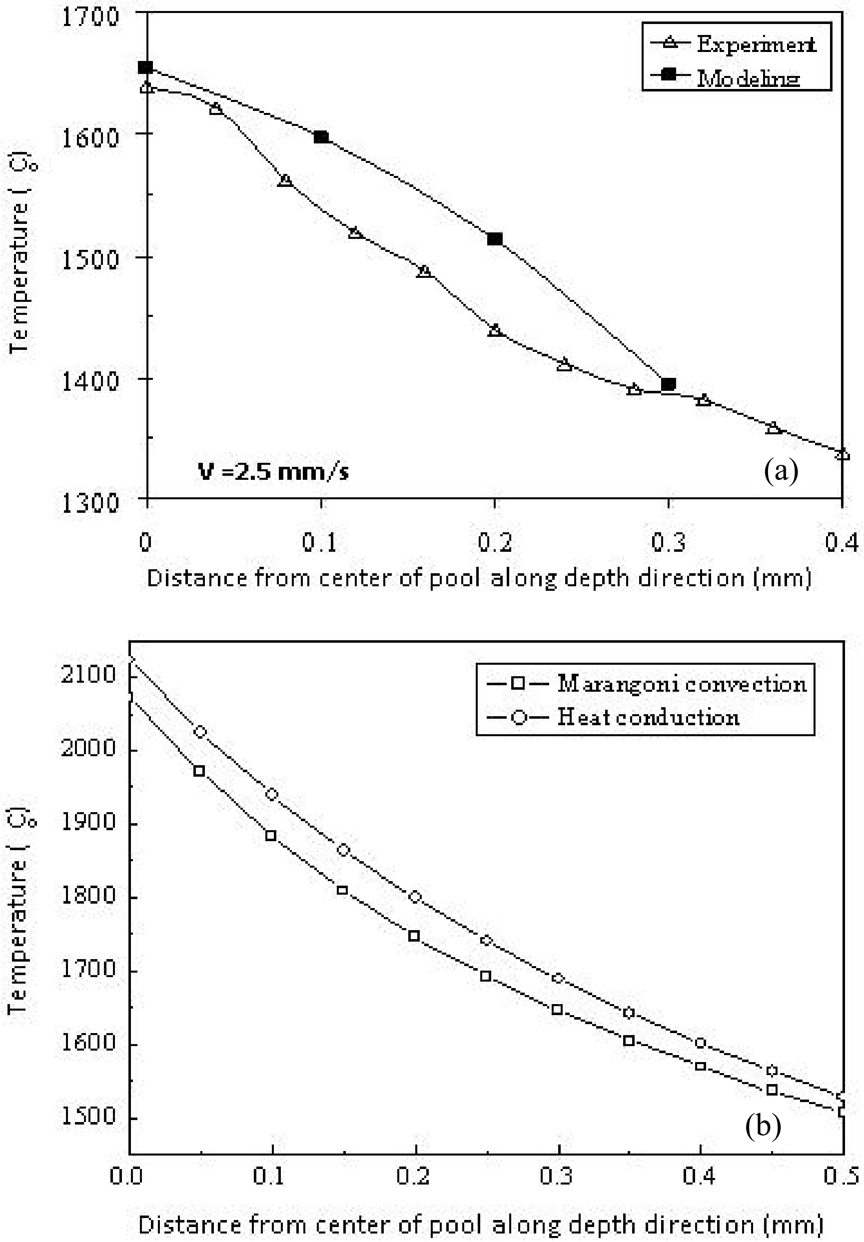

Figure 3.2 Temperature profiles along the depth direction. (a) Experiment and 3D heat conduction model of Ref. [159]. (b) Temperature profiles along the depth direction obtained by 2D model

The scales of temperature of Figures 3.2(a) and (b) are not directly comparable because the results of Figure 3.2(b) were obtained with a 2D model, which results in a higher power density. However, it is clear from Figure 3.2(b) that the effect of ignoring

Marangoni convection is to over-predict the temperature by approximately 60°C, in good agreement with the experimental observation in Figure 3.2(a).

Figure 3.3 shows the velocity field in molten pool with (Marangoni convection in Figure 3.3(a)) and without (Natural convection in Figure 3.3(b)) consideration of surface tension at the moving speed of 4mm/s. The melt steel rises from the pool bottom to the pool surface. It continues to flow outward from where (the right of center of the pool surface) the temperature is higher and the surface tension lower (for Marangoni convection) or the density lower (for natural convection), toward the edge of the pool surface, where the temperature is lower and the surface tension higher (for Marangoni convection) or the density higher (for natural convection). It goes on to sink along the container wall and returns to the pool bottom to start all over again. There are two asymmetric flow loops in the pool. The one on the right is clockwise and the one on the left is counterclockwise. The flow vertex centers are closer to the surface with the consideration of Marangoni effect than with natural convection.

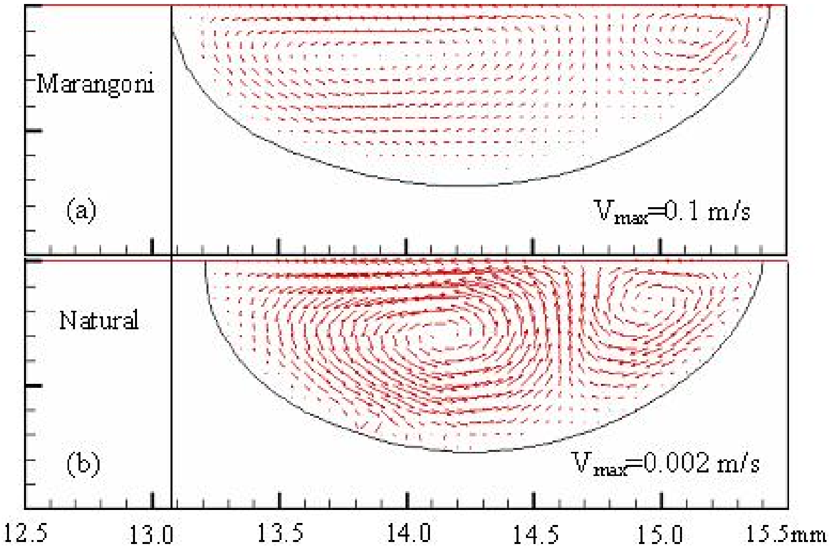

Figure 3.3 Velocity field with (a) Marangoni convection and (b) Natural convection at the moving speed of 4mm/s with high laser power

Calculation is performed at the same moving speed of laser speed, but decreasing the laser power input (energy of laser beam), aiming to get a smaller geometry size of molten pool comparing to that shown in Figure 3.3. Figure 3.4 shows the velocity and fluid flow pattern. While considering the Marangoni effect, the surface tension makes the pool obviously appear two flow loops even in much smaller pool size. If the calculation is carried out only with natural convection, it is easily and interestingly to be seen that the right vertex in the molten pool is too close to the pool surface and nearly disappears. So, it can be concluded that the flow pattern in molten pool is affected by pool size.

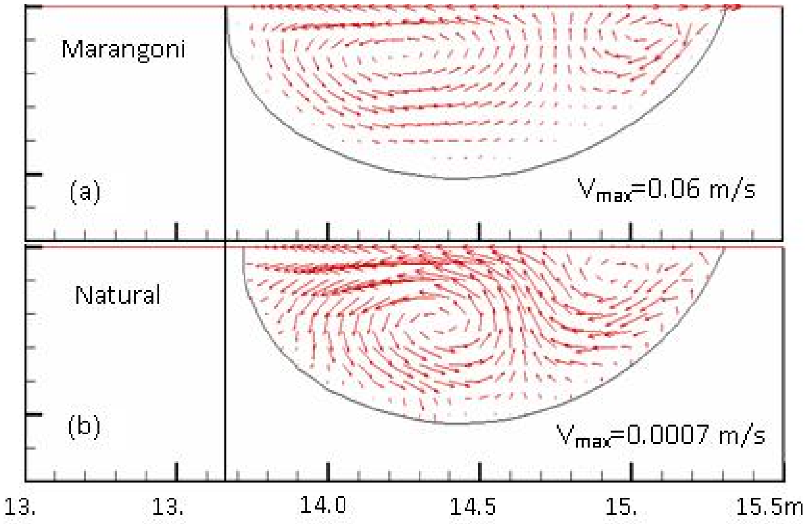

Figure 3.4 Velocity field with (a) Marangoni convection and (b) Natural convection at the moving speed of 4mm/s with low laser power

Figure 3.5(a) and (b) respectively show the velocity fields for Marangoni convection and natural convection with the moving speed of 16mm/s. There is only one loop in the liquid pool with its center far from the pool surface and the right loop disappears when just considering the natural convection as shown in the figure. However, there still exist two loops although the right one is small if considering the effect of surface tension in the calculation

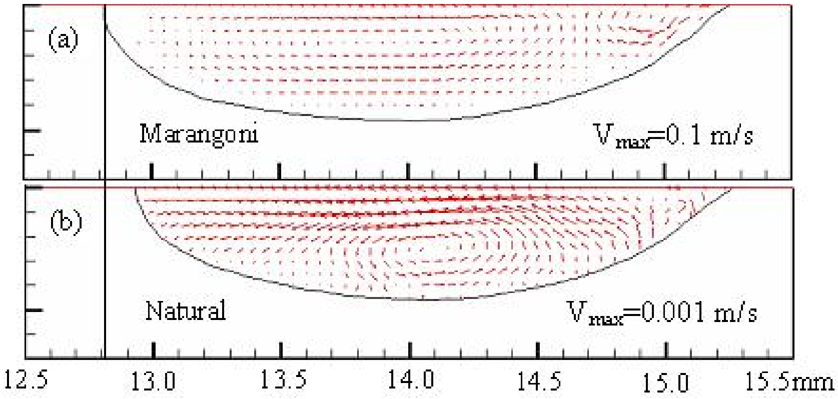

Figure 3.5 Velocity field with (a) Marangoni convection and (b) Natural convection at the moving speed of 16mm/s with high laser power

As shown in the three Figures 3.3-3.5, it is clearly seen that there are two flow loops (if have) which are asymmetric because of the movement of laser beam, and the centers of the flow loops are closer to the pool surface with the effect of Marangoni than that without the effect of Marangoni. By comparing the results of marangoni and natural convections, these three figures have another obvious common: the pool has a wider size with the consideration of Marangoni effect. Also, the flow pattern in molten pool is affected not only by pool size also by moving speed of laser beam. So the convection in these pools is dominated by Marangoni convection in each case.

Figure 3.6(a) shows the temperature profiles along the pool surface for a laser travel speed of 4mm/s calculated under different assumptions of heat transfer mechanisms. The flow of molten steel from locations of higher temperature to lower temperature makes the peak temperature decrease in comparison with the pure conduction case, while increasing the temperature at the periphery of the pool. For this value of the laser travel speed (4mm/s) the maximum temperature in the surface of the pool calculated with heat-conduction-only model exceeds the one calculated with the Marangoni model by approximately 100°C. As expected, the temperature profiles corresponding to natural convection and heat conduction are almost identical because of the weak buoyancy flow in the small molten pool. It is also observed that the molten pool becomes wider with the Marangoni effect. It indicates that the Marangoni flow plays an important role in transferring the heat from the center of the laser beam to the molten pool boundary. A similar comparison of the temperature profiles is done in Figure 3.6(b) for a laser travel speed of 16mm/s. It is observed that in this case the temperature profiles are closer to each other, with peak temperatures differing by 50°C approximately. This is an interesting observation because it indicates that for large laser travel speeds, a conduction-only model may be good enough to simulate the thermal transport in the pool. Keep in mind that the laser power is another factor that affects the temperature profile and is not considered here; a large power will increase the size of the pool and may make again important the Marangoni effect, even for fast travel speeds.

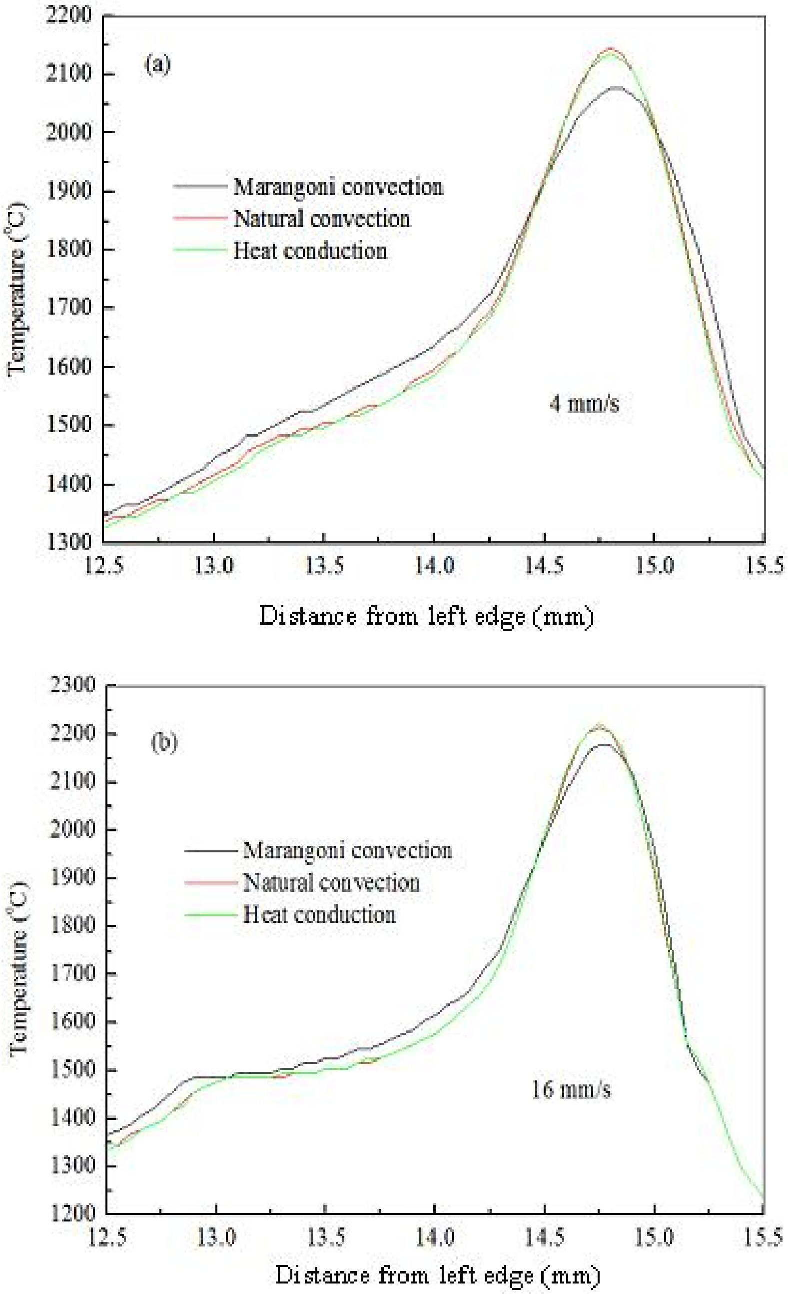

Figure 3.6 Temperature profiles along the pool surface for laser travel speeds of (a) 4mm/s and (b) 16mm/s

The solidification model can calculate the volume fraction of liquid and hence allow comparison of the size of the molten pool relative to the mushy zone, as shown in Figure 3.7. It is observed that, due to the very steep temperature gradients, the mushy zone is extremely thin, only about 0.1 mm at the trailing edge and much thinner at the front. A fine mesh discretization is necessary in order to properly capture the solidification and transport phenomena in this region.

The convection field in the pool is also shown in Figure 3.7. The liquid metal flows upward at the position where the laser beam impinges on the surface and then two recirculation cells form, a small one ahead of the laser beam and a larger one behind. Note the high magnitude of the velocity caused by the Marangoni convection, in agreement with previous reports [43, 45]. The velocity drops several orders of magnitude as the liquid enters the tip of the mushy zone, but it is evident that this intense convection field must have a strong influence in the solute mixing and dendrite growth, which in turn will affect the solidification microstructure. Because of the thin mushy zone and strong convection, a continuum-type model as used in this work is not adequate to investigate the interdendritic transport phenomena in more detail. This is an area for potential research using a microscopic model of dendrite growth under strong convection fields [19, 122].

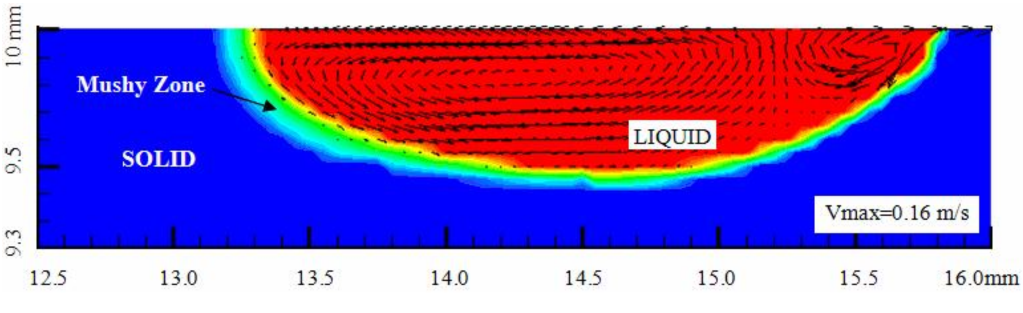

Figure 3.7 Volume liquid fraction for laser moving speed of 8mm/s (Red: all liquid, Blue: all solid). Velocity vectors are shown in black

Figures 3.8(a) and (b) show the profiles of temperature gradient along the x- and y- directions calculated for two laser travel speeds and with two different assumptions of heat transfer: heat conduction and Marangoni convection. It is observed that the Marangoni convection affects mostly the x-component of the gradient when compared to a pure conduction model. The y-component of the gradient is relatively insensitive to the Marangoni effect for both travel speeds, while the maximum x-component is over predicted by about 300°C/mm when a pure conduction model is used instead of a model including Marangoni convection. However, both models (pure-conduction and Marangoni) predict a doubling of the maximum y-gradient when increasing the travel speed from 4 to 16mm/s. This indicates that heat conduction in the y-direction (i.e., depth direction) is dominated by heat conduction, while Marangoni convection affects mainly the heat transport in the x- (horizontal) direction.

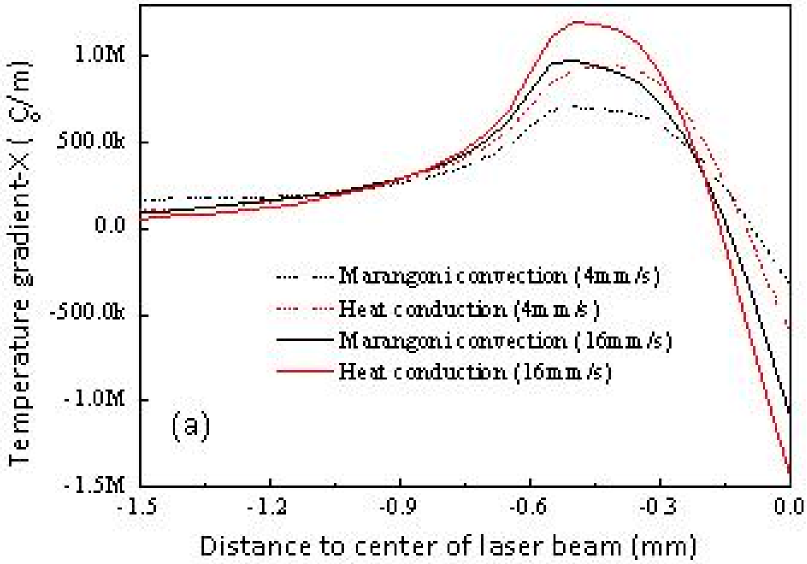

Figure 3.8 (a) x- component and (b) y-component of temperature gradient profiles along the pool surface for laser speeds of 4mm/s and 16mm/s

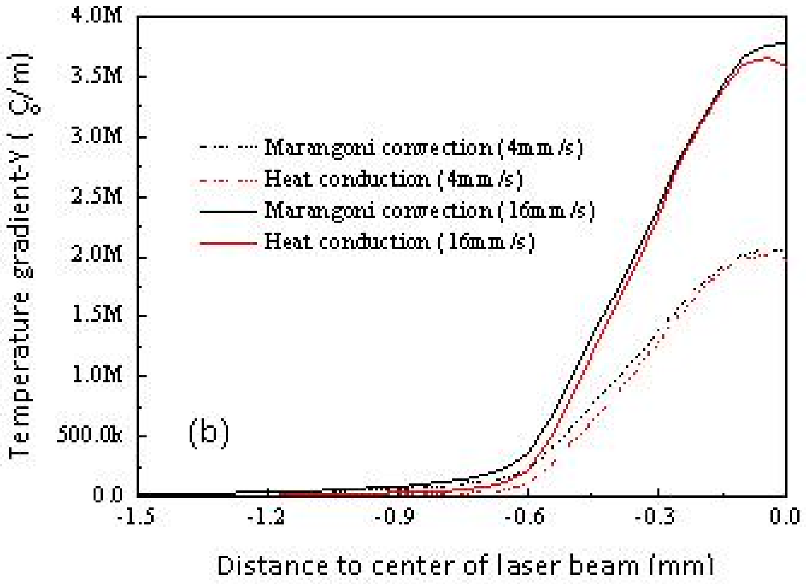

Figure 3.8 (Continued)

The simulation results shown in Figure 3.9 give an idea of the sensitivity of the velocity profiles along the molten pool surface to the magnitude of the surface tension coefficient (Eq.3.9). The value of the surface tension gradient used in the previous calculations is -0.0004N/(m K) (Table A.1 in Appendix A). It is observed that doubling the value of the surface tension coefficient approximately doubles the peak velocity in the pool, although the shape of the velocity profile stays basically the same. Note the strong intensity of the velocity, which is consistent with other observations reported in the literature [43, 45]. The case of zero surface tension gradient corresponds to natural convection; for this case the maximum velocity is about 10^{-3}m/s and does not show in the plot.

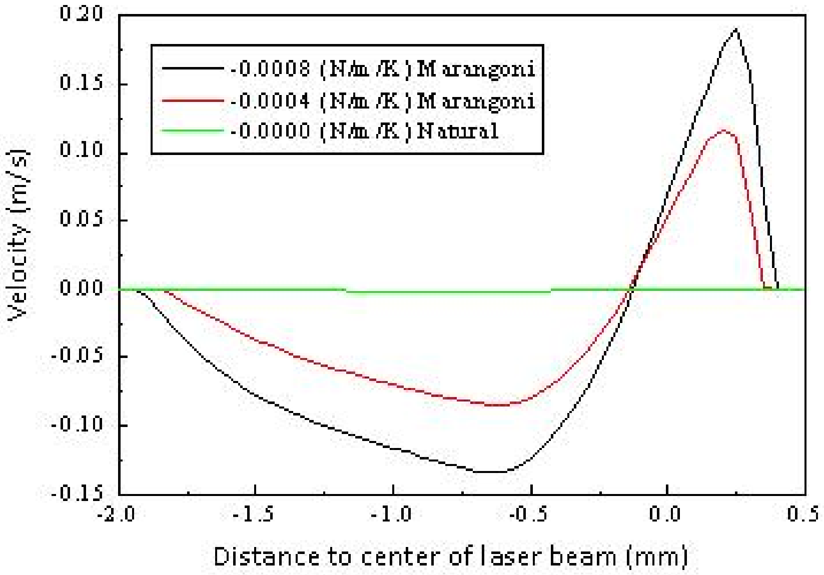

Figure 3.9 The velocity profile on the pool surface for different surface tension coefficients

The model developed in this work is able to calculate solute redistribution during solidification due to solute partitioning and diffusion/convection transport. To our knowledge, this is the first calculation of this type reported for the LENS process. The liquidus temperature of AISI410 and the partition ratios for C, Si, Mn, and Cr are calculated using the commercial software ThermoCalc. The initial solute concentrations for each element in AISI410 are indicated in Table 3.1.

Table 3.1 Chemical composition of AISI410 used in the simulations, wt %

C	Si	Mn	Cr
0.13	0.35	0.46	12.0

Figure 3.10 shows the solute concentration field of C, Si, Mn, and Cr in the melt pool and surrounding area during deposition. The mushy zone has been indicated by two black lines corresponding to the liquidus and solidus isotherms. In this simulation the

laser travel speed is 2.5mm/s, hence a wider mushy zone is obtained than the one observed in Figure 3.7. Although the color scale has been amplified to detect slight variations of concentration, it is observed that no significant macrosegregation has occurred. This is attributed to the effective mixing produced by the strong Marangoni convection.

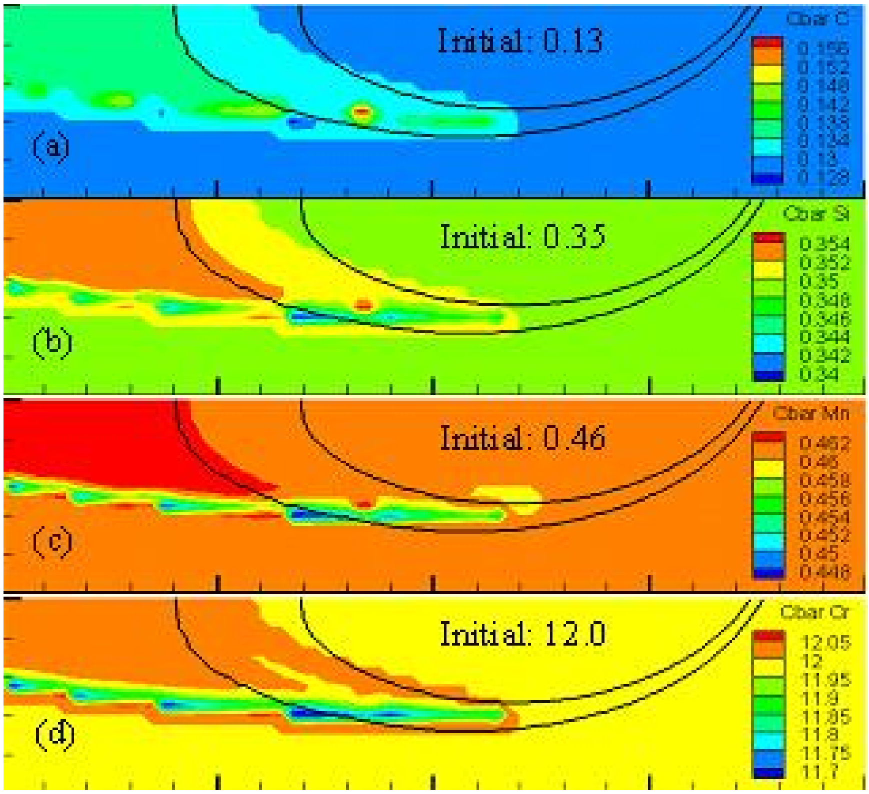

Figure 3.10 Solute concentration fields at the moving speed of laser beam 2.5mm/s for (a) C, (b) Si, (c) Mn, and (d) Cr

3.4 Discussion

3.4.1 Relative importance of different driving forces

The driving forces for the liquid flow in the weld pool considered in the model include the surface-tension and the buoyancy forces. The surface tension force, often referred as the Marangoni force, arises because of the spatial variation of surface tension between the near-middle and the periphery of the pool resulting from the temperature gradient. The Marangoni number, M_a, is used to describe the ratio of surface tension gradient force to viscous force, while the Grashof number, G_r, describes the ratio of buoyancy force to viscous force. Some works have reported the relative importance of different driving forces in the molten pool based on the ratio of surface tension force to buoyancy force [39,41], which for the parameters of our simulations yield:

$$R_{s/b} = \frac{M_a}{G_r} = \frac{(\rho L_R \Delta T |\partial\gamma/\partial T|)/\mu^2}{(g\beta {L_b}^3 \Delta T \rho^2)/\mu^2} = \frac{L_R |\partial\gamma/\partial T|}{g\beta {L_b}^3 \rho} = 2.55 \times 10^4 \qquad \text{(Eq.3.10)}$$

Where g is the gravitational acceleration, β is the thermal expansion coefficient, ΔT is the temperature difference between the peak pool temperature and the solidus temperature, and L_b is a characteristic length for the buoyancy force in the liquid pool which is approximated by one eighth of the pool radius. L_R is a characteristic length taken as the pool radius at the top surface of weld pool. Therefore, it can be expected that the liquid flow is mainly driven by Marangoni convection and to a much less extent by the buoyancy force, which is consistent with the results shown in Figures 3.3-3.5 and 3.9.

3.4.2 Relative importance of conduction and convection

In the weld pool, heat is transported by a combination of convection and conduction. The relative importance of convection and conduction in the overall transport of heat can be assessed from the value of the Peclet number, P_e, which for the parameters of our simulations yields:

$$P_e = \frac{heat_{convection}}{heat_{conduction}} = \frac{u\rho C_P \Delta T}{(\lambda \Delta T)/L_R} = u\rho C_P L_R/\lambda = 240u \qquad \text{(Eq.3.11)}$$

Where u is the velocity of the liquid metal in the pool. The Marangoni force causes a large horizontal velocity (~0.2m/s), particularly near the surface of the pool, hence it is expected that advection dominates heat transport in the x-direction, while in the vertical direction heat is transported mostly by conduction. This observation is also made from the analysis of the temperature gradient profiles in Figure 3.8.

3.4.3 Order of magnitude of maximum velocity in the weld pool

The convection in the pool results mainly from the surface tension force that is determined by the temperature gradient at the pool surface. The maximum velocity can be roughly estimated assuming that it occurs approximately halfway between the heat source axis and the weld pool edge [41, 160]

$$u_m{}^{3/2} = \frac{\partial \gamma}{\partial T}\frac{\partial T}{\partial y}\left(\frac{W^{1/2}}{0.664\rho^{1/2}\mu^{1/2}}\right) \qquad \text{(Eq.3.12)}$$

Where W is the width of the weld pool. According the above equation, the maximum velocity is approximately 0.9m/s, while the simulations give a maximum velocity of about 0.2m/s. The smaller simulated velocity is attributed to the shallow pool of the LENS process in comparison with the larger spot-welding pools for which Eq.3.12 is usually applied. It should be mentioned that although velocities of this magnitude and higher have been reported in the literature, there exist wide discrepancies in the results obtained by various investigators. Experimental determination of the velocities and temperatures in the weld pool remains a major challenge in the field.

3.5 Conclusions

A comprehensive 2D solidification model, that included the calculation of fluid flow and macrosegregation, was developed to simulate the temperature, solute redistribution, geometry and flow pattern in the molten pool during the LENS process of steel alloy AISI410. The velocity profile in the molten pool was affected not only by the moving speed of the laser beam but also by the pool geometry and size. Strong Marangoni convection dominated the liquid flow in the pool and increased the width of the pool. When surface tension effects were not important, the velocity due to natural convection was very small and the temperature profiles in the pool were indistinguishable of the pure conduction case. The effect of the Marangoni convection on the temperature profiles was also affected by the laser travel speed, producing changes in the temperature gradient. Both the temperature coefficient of the surface tension and the laser travel speed affected the peak fluid velocity in the pool. For the material and process parameters analyzed, no significant macrosegregation was observed in the calculated solute profiles.

The work of this chapter was pre-viewed and presented in the conference TMS in 2008 [161].

CHAPTER IV

DENDRITE GROWTH SIMULATION DURING SOLIDIFICATION IN LENS PROCESS

4.1 Introduction

Many samples have been tested to prove the good mechanical properties obtained with LENS, like yield strength, ultimate strength and hardness for various kinds of alloys Some comparisons were made with the same deposition materials by LENS to other processing methods, and the results showed that the LENS parts had better mechanical properties due to the very fine microstructure produced by the high cooling rate.

The microstructure, which is determined by the thermal history and also controls the mechanical properties, gained more and more attention, and many experiments have been done to analyze the microstructure, especially the grain size (DAS for columnar dendrite) and morphology. Experiments have proved that very fine microstructures were formed due to the high cooling rates and temperature gradients and studied the relationship between the cooling rate ξ (K/s) and DAS, η, and these showed that a linear relationship exists between log ξ and log η [162]. A general relationship between ξ and SDAS (η_2, in μm) was experimentally determined as $\eta_2 = 25\xi^{-0.28}$ for AISI310 in laser welding [163]. Ghosh and Choi [68] deduced an equation which described the relationship between the DAS and the thermal behaviors, and based on the equation, the DAS was calculated to evaluate the microstructure. Very few papers [19, 100] were published on the numerical modeling of the microstructure evolution during the solidification and solid-state phase transformation while cooling down to room temperature, with scarce or no details on the dendrite morphology and growth process.

This chapter will focus on the microstructure evolution of the solidification process: DAS and dendrite morphology and the influence of LENS process parameters on the solidification. A 2D FE method coupled with a CA technique is developed to calculate the dendritic growth during the solidification in the molten pool during LENS deposition of a single layer of Fe-0.13wt%C binary alloy, and the thermal properties adopted in the calculation as listed in Table A.2 in Appendix A. The model solves the conservation equations of heat and mass transfer in order to calculate the temperature field, solute concentration, and the dendrite growth morphology. The relationship between the cooling rate and DAS, including PDAS and SDAS, is determined by evaluating the constants of the empirical expression of Ref. [163]. The effect of the moving speed of the laser beam, laser power, layer thickness, and substrate size on the grain growth is discussed. Dendrite morphologies at locations close to the top surface and close to the substrate are also compared.

4.2 Model description

The simulation of dendrite growth needs a much smaller scale (microns) than that of thermal modeling of LENS process; hence two spatial scales are used in the model – a macro scale for LENS heat transfer calculation and a micro scale for the simulation of dendrite growth.

4.2.1 Calculation of solute distribution and nucleation

The Chapter II gives the details of the thermal field simulation during LENS deposition. The calculation of the transient temperature field is performed in a computational domain encompassing the molten pool and surrounding area as shown in Figure 4.1(a) with mesh as shown in Figure 4.1(c). A small square domain of 100μm in side length (Figure 4.1(b)) is considered for the grain growth simulation. Each FE mesh in this small domain is refined into m×m cells for the solute and CA calculations with mesh as shown in Figure 4.1(d). The temperature of each cell is obtained by interpolating the temperatures of the four nodes of the FE. At two different locations of the molten pool, top domain (next to the pool surface) and bottom domain (0.5 and 0.25mm below the pool surface for layer thickness of 0.5 and 0.25mm, respectively), the dendrite morphologies are studied. A comparison is also performed for dendrite growth resulting from deposition over a thin (1.5mm) and thick (5mm) substrate.

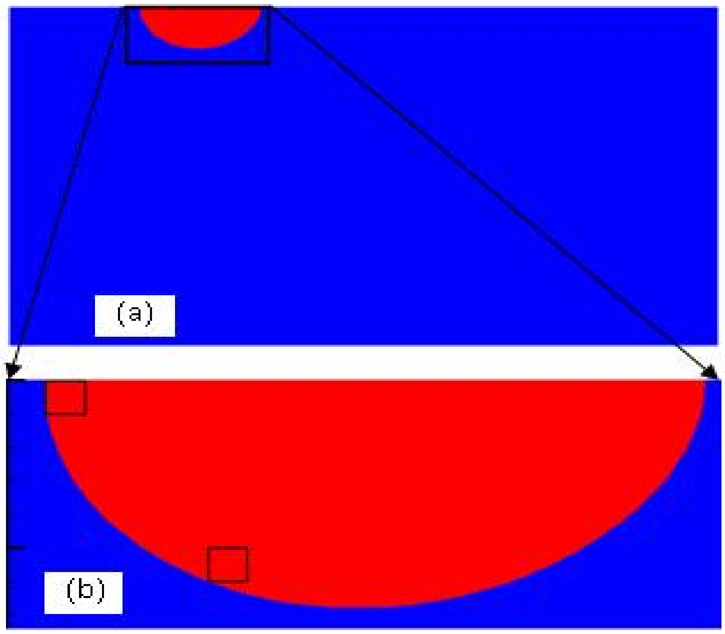

Figure 4.1 (a) LENS calculation domain of thermal model with indicated molten pool at the top; (b) small square domains with side length of 100μm (upper domain is close to top surface and bottom domain is one-layer-thickness from top surface; (c) magnification of small domain (upper/bottom domains) in (b) with FE mesh; (d) the cells network of each finite element as shown in (c) (example: element HIJK) for calculation of solute transfer and grain growth in the CA method.

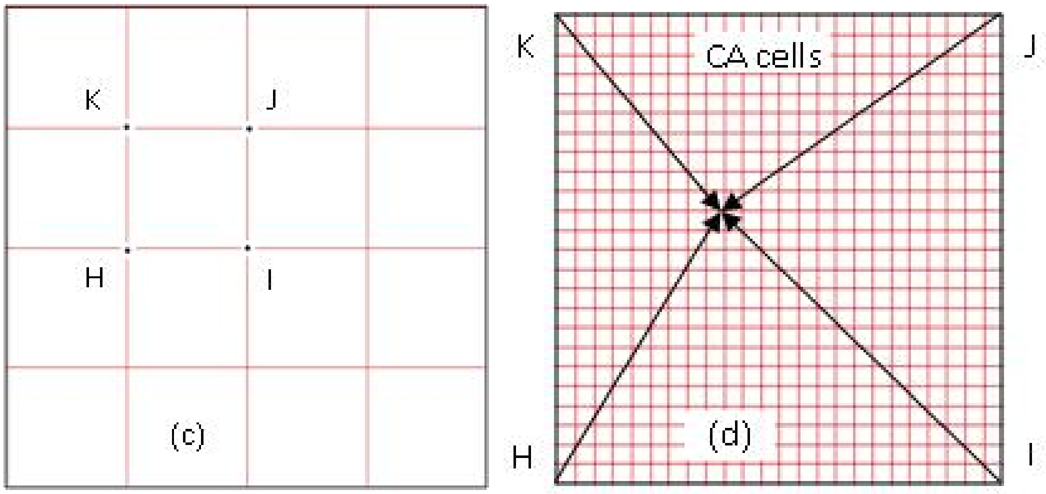

Figure 4.1 (Continued)

The solute conservation in solid and liquid phases is obtained by solving the governing equation for each phase separately, as shown below:

$$\frac{\partial c_i}{\partial t} = D_i \cdot \nabla^2 c_i + c_i \cdot (1-k)\frac{\partial f_s}{\partial t} \qquad \text{(Eq.4.1)}$$

Where c is solute concentration, D is solute diffusivity, the subscript i indicates solid or liquid, k is the partition coefficient, and f_s is solid fraction.

At the Solid/Liquid interface, the solute partition between liquid and solid is given by:

$$c_s^* = k \cdot c_l^* \qquad \text{(Eq.4.2)}$$

Where c_s^* and c_l^* are interface solute concentrations in solid and liquid phases, respectively. A zero-flux boundary condition is applied to the cells located at the boundaries of the calculation domain.

The interface curvature of a cell with solid fraction f_s can be obtained by counting the nearest and second nearest neighboring cells [139]:

$$K = \frac{1}{a}\left(1 - 2\frac{f_s + \sum_{j=1}^{N} f_s(j)}{N=1}\right) \qquad \text{(Eq.4.3)}$$

Where a is the length of the CA cell side, N is the number of the nearest and second nearest neighboring cells, and $f_s(j)$ is the solid fraction of neighboring cells.

The liquid concentration in interface cell is given by [121]:

$$c_l = c_l^* - \frac{1-f_s}{2} \cdot a \cdot G_c \qquad \text{(Eq.4.4)}$$

Where G_c is the concentration gradient in front of the solid/liquid interface, and the interface equilibrium composition (c_l^*) is calculated by:

$$c_l^* = c_0 + \frac{T^* - T_l^{eq} + \Gamma K}{m_l} \qquad \text{(Eq.4.5)}$$

Where $c_0$is the initial solute concentration, $T^*$is the interface equilibrium temperature calculated by Eq.2.1, T_l^{eq} is the equilibrium liquidus temperature at the initial solute concentration, m_l is the liquidus slope, Γ is the Gibbs-Thomson coefficient, and K is the curvature of the S/L interface.

A continuous Gaussian nucleation distribution, $dn/d(\Delta T)$, is used to describe the grain density increase(dn) with the increase of undercooling by $d(\Delta T)$. The total density of nuclei, $n(\Delta T)$, at a certain undercooling ΔT, is given by [102, 133, 140, 164]:

$$n(\Delta T) = \frac{N_{max}}{\sqrt{2\pi}\Delta T_\sigma}\int_0^{\Delta T} \exp\left[-\frac{(\Delta T - \Delta T_N)^2}{2(\Delta T_\sigma)^2}\right] d(\Delta T) \qquad \text{(Eq.4.6)}$$

Where ΔT_N is the mean nucleation undercooling, ΔT_σ is the standard deviation of undercooling, and N_{max} is the maximum nucleation density.

For one time step, the undercooling increases by $\delta(\Delta T)$, so the density of nuclei increases by:

$$\delta n = n\big(\Delta T + \delta(\Delta T)\big) - n(\Delta T) = \frac{N_{max}}{\sqrt{2\pi}\Delta T_\sigma}\int_{\Delta T}^{\Delta T+\delta(\Delta T)} \exp\left[-\frac{(\Delta T-\Delta T_N)^2}{2(\Delta T_\sigma)^2}\right] d(\Delta T)$$
(Eq.4.7)

The nucleation probability of each cell is given by:

$$p^n = \delta n \cdot V_c$$ (Eq.4.8)

Where V_c is the volume of a single cell. Nucleation will occur in the cell when the cell's random number [0, 1] is less than p^n.

4.2.2 The rules of capturing interface cells

Each cell of the CA mesh has three possible states: solid, liquid, and interface (partially solidified). Figure 4.2 shows a sketch of the grain growth model, illustrated for the case of a cubic crystal material [121, 130]. Since a cubic crystal material grows following four preferred directions and has a four-fold symmetry, a square-shape solid seed is initially placed at the center of a cell and the seed is allowed to grow along its diagonals. Once the corners of the square seed reach any of the eight neighboring cells, the neighbor cell will be changed to an interface cell. A new square seed, having the same preferential crystallographic orientation as the original cell, is generated and placed at the center of the new interface cell. The new square seed starts to grow according to the change of the solid fraction in the new interface cell. After the original square has changed its neighboring cells into interface cells, the original cell continues to grow until its solid fraction becomes unity, after which the state of the original cell becomes solid and changes any surrounding liquid cells into interface cells. During the growth, the length of the diagonal (d_s) of the seed is calculated based on the solid fraction f_s.

$$d_s = \sqrt{2} \cdot f_s \cdot a$$ (Eq.4.9)

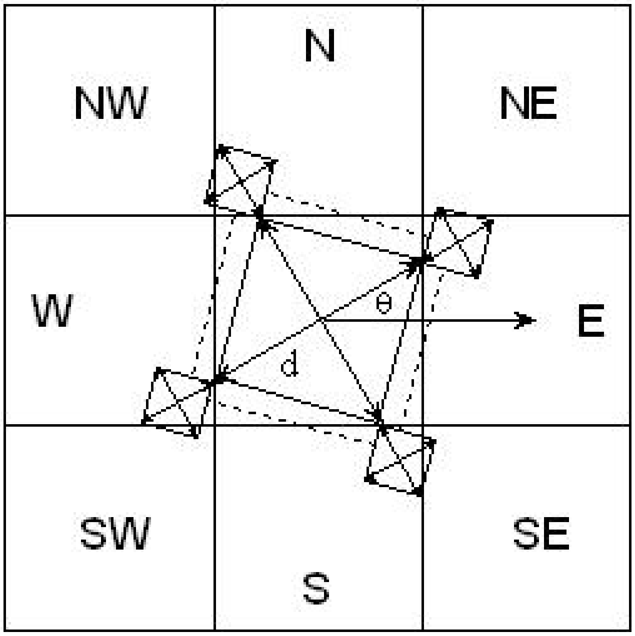

Figure 4.2 Sketch of growth algorithm for cubic crystal material used in this model, with a nucleus set in the cell center with preferential orientation of θ to the x-axial.

4.3 Simulation results

4.3.1 Cooling rate and DAS

The SDAS and PDAS for various cooling rates are determined by examining the simulated dendritic structure in this model. Figure 4.3(a) and (b) show the relationship between the cooling rates and the SDAS and PDAS, respectively, both of which indicate that the DAS (SDAS and PDAS) decreases with increasing cooling rates. The experimental relationship between the SDAS and cooling rate for AISI310 from Ref. [163] and the experiment data for Fe-Ni-Cr ternary alloys with 59 pct Fe by Electron-Beam Surface melting from Ref. [165] are also plotted in Figure 4.3(a), showing a similar trend with the simulated curve and good agreement for low cooling rate. The experimental data, however, shows about 30% larger DAS than the calculation for higher cooling rate. This may be due to the different composition contents of the alloy used in this model and the experiments. By fitting the calculation data, a new equation describing the relationship between the cooling rate and SDAS for AISI310 is proposed as indicated in Figure 4.3(a). The simulated values of PDAS are significantly higher than the SDAS, reaching values as large as 20μm for the lower cooling rates. Choi and Mazumder [166] developed a FE welding model to predict thermal history and PDAS and found that the average size of the PDAS was dependent upon the welding speed, varying between 7.5 and 20μm for columnar dendrites at a cooling rate of around 400K/s for AISI304 stainless steel, which is in good agreement with our results of Figure 4.3(b). The calculated values of PDAS is also supported by the measured data by Elmer *et al.* [165] as shown in Figure 4.3(b).

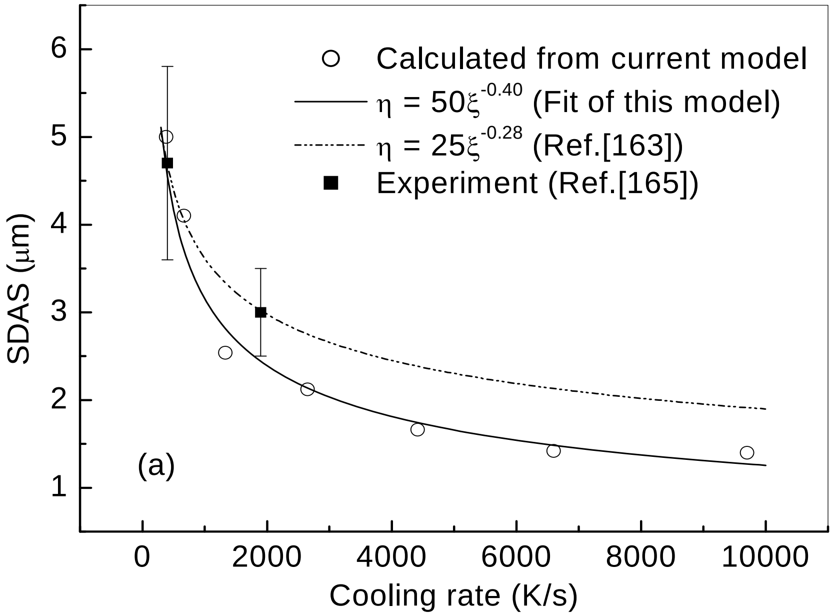

Figure 4.3 (a) SDAS and (b) PDAS as a function of the cooling rate calculated in this model for alloy Fe-0.13%C and published experiments.

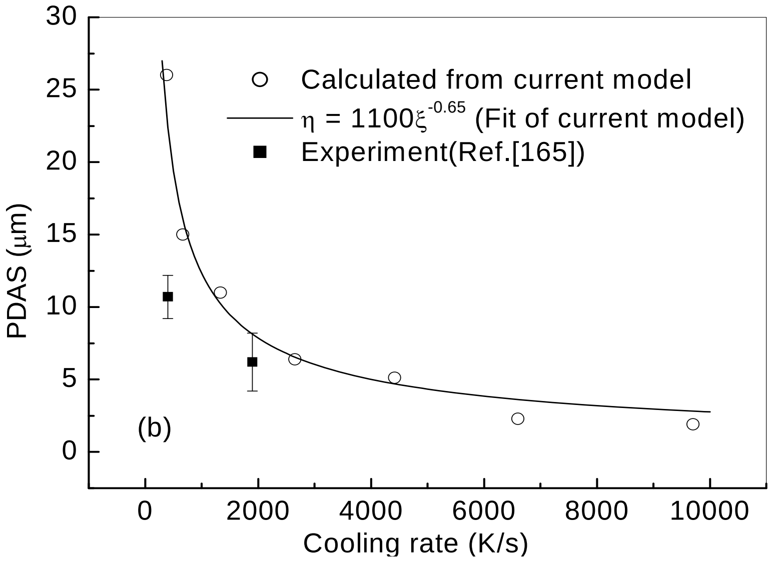

Figure 4.3 (Continued)

4.3.2 Moving speed of laser beam and dendrite morphology

A single layer of 0.25mm is deposited over a 5mm thick substrate. The laser power is set so that the depth of the molten pool is somewhat larger than 0.25mm in order to have an overlap with the substrate. In the calculation, in order to keep approximately a constant size of the molten pool for various moving speeds of the laser beam, a higher laser power must be used for faster laser speed, as determined in several experimental and modeling works [167-169, 90]. Figure 4.4(a-c) show the solidification microstructure in the small square domain located in the lower region of the molten pool (see Figure 4.1(b)) for different travel speeds of the laser beam. The calculated cooling rate is also shown. The color bar scale on the right denotes solute concentration of Carbon in wt%. With the increase of the scanning speed, the dwell time of the heat source at each point of the track decreases; therefore, the solidification velocity and cooling rate increase. When the laser moving speed increases from 2 to 20mm/s, the cooling rate increases from 1050 to 9000K/s with constant pool size. The figures clearly show the columnar-type dendritic growth, with varied DAS depending on the cooling rate. It is easily seen that by increasing the scan speed of the laser beam both the PDAS and SDAS decrease. Due to the extremely high cooling rate and the narrow PDAS (less than 5μm) at the laser moving speed of 20mm/s (Figure 4.4(c)), formation of secondary and terciary arms is not always possible, and an interesting dendrite-to-cellular transition is observed. Previous experimental works [59, 69, 97] have confirmed that both a finer microstructure and a higher cooling rate were obtained by increasing the laser travel speed. Kobryn *et al.* [97] investigated the influence of laser speed on grain growth and found that the grain size decreased by increasing the laser scaning speed. Pal [170] observed that dendrites and cells coexisted in laser welded AISI316 with scanning speed of 15mm/s. Pan *et al.* [77] conducted laser deposition experiments with scanning speed of 50.2mm/s and observed the directional growth of cells within the center part of the molten pool. It must be noted that although the simulations of Figure 4.4 show an approximately constant molten pool size, this is achieved by adjusting the laser power. In actual depositions, the laser power is left constant and if the laser moving speed is increased, a smaller pool size will be obtained, which results in a higher cooling rate and smaller dendrite size.

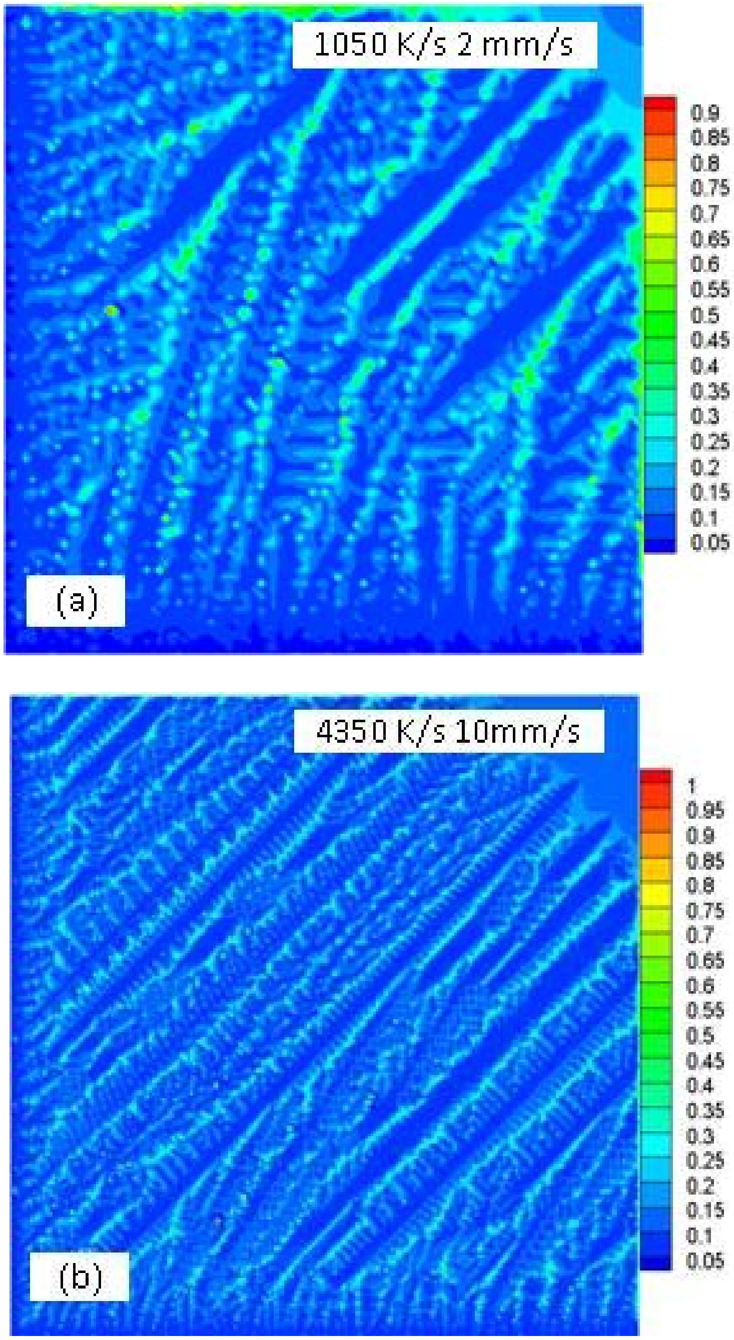

Figure 4.4 Solidification microstructure when laser moving speed is (a) 2mm/s, (b) 10mm/s, and (c) 20mm/s. Cooling rate (K/s) is also shown. Color bar denotes solute concentration of C (wt%). Note dendritic to cellular transition for the highest cooling rate (c). (d) microstructure of type AISI316 Laser welds, Power 1.2KW, Speed 15 mm/s. 200X[170]; (e) SEM micrograph of cells within the center part of the molten pool (50.2mm/s) [77].

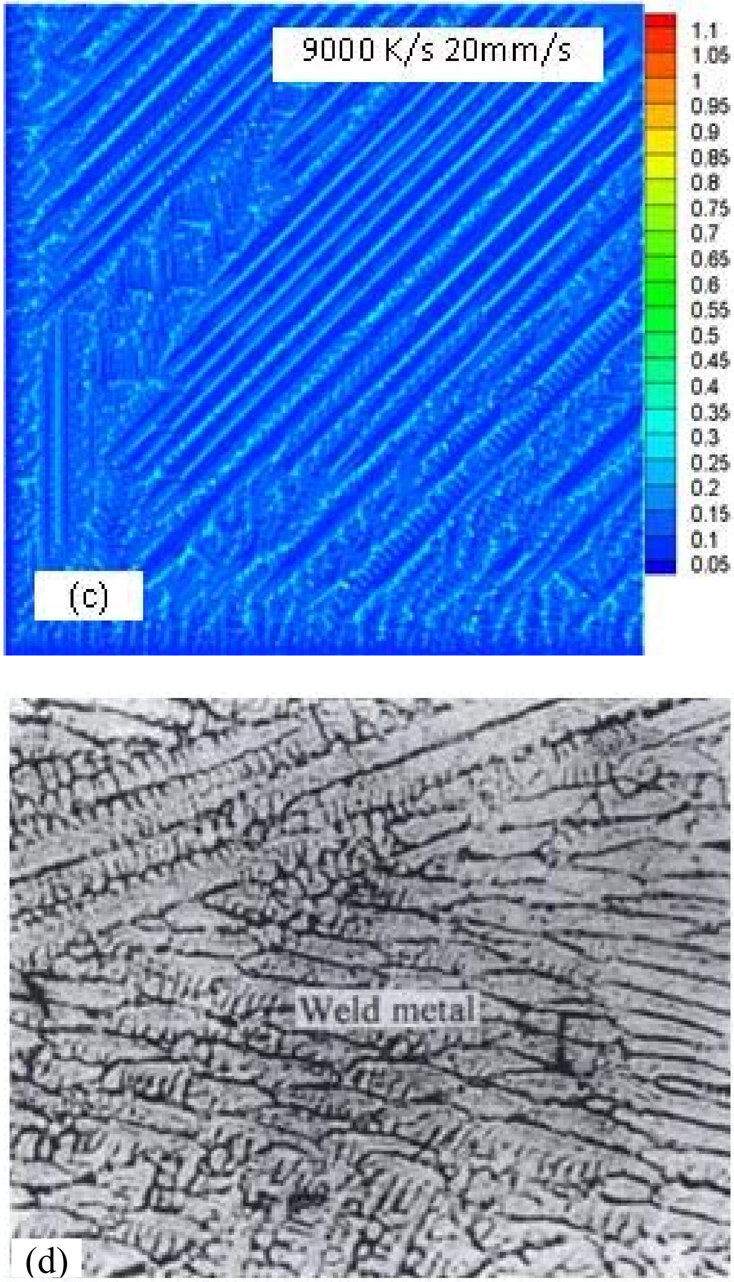

Figure 4.4 (Continued)

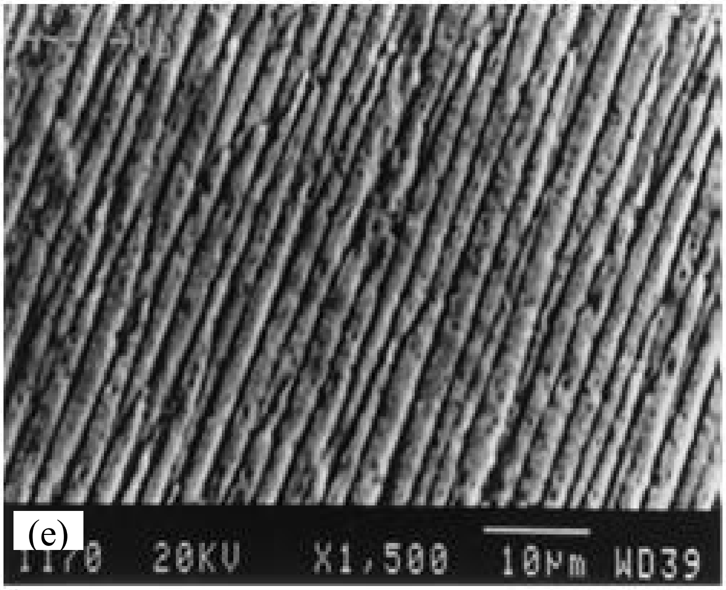

Figure 4.4 (Continued)

4.3.3 Layer thickness and dendrite morphology

Figure 4.5(a) and (b) show the dendrite structure in the small square domain located in the lower region of the molten pool (see Figure 4.1(b)) for a laser moving speed of 10mm/s and layer thickness 0.25mm (Figure 4.5(a)) and 0.5mm (Figure 4.5(b)). When increasing the deposited layer from 0.25 to 0.5mm (larger amount of powder metal) for a single pass, the corresponding laser power is also increased, and thus a larger molten pool is formed. A thicker layer needs higher laser power, which results in more latent heat removed from the molten pool. This produces a lower cooling rate as indicated in Figure 4.5, which is in agreement with the experimental observations in Refs. [13,16,91]. It can be observed in Figure 4.5 that the dendrites have larger PDAS and SDAS with higher laser power and larger pool size because of the lower cooling rate obtained when a larger amount of powder (thicker layer) is deposited. With a high laser power, as well as a larger amount of molten material being added, the solidifying material is held at a higher temperature for a longer time, and therefore, the local temperature gradients are smaller. This allows the grains to have more time to grow. It is interesting to see from Figure 4.5(b) that not all grains grow with an aligned columnar structure. Owing to the high rate of solidification, the grain growth becomes unstable. The dendrite tips may split and continue growing in two directions or the side arms grow faster than the main arm does [105]. Several experiments have also shown that a finer dendrite structure is obtained for lower power levels [16,75,91]. Mazumder *et al.* [75] performed experiments in which they deposited two samples with different layers of thickness to determine the influence on the microstructure. It was observed that the dendrite structure was finer when depositing a thinner layer (0.25mm) in comparison with a thicker layer (1.37mm).

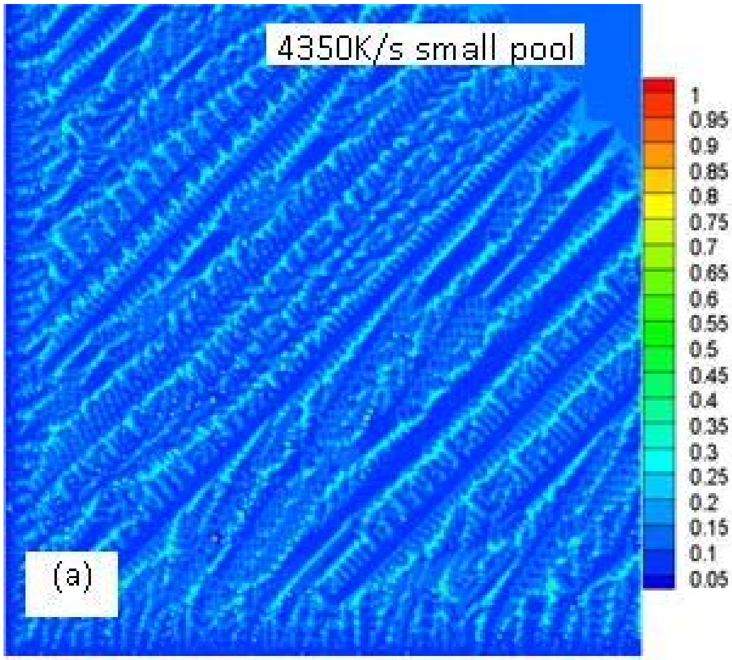

Figure 4.5 Dendrite structure with deposition layer thickness of (a) 0.25mm and (b) 0.5mm at a laser moving speed of 10mm/s. The color bar indicates solute concentration of C (wt%); Microstructure of LENS deposited H13 with (c) 1.37mm and (d) 0.25mm layer thickness, showing a finer dendritic structure for thinner layer [75]

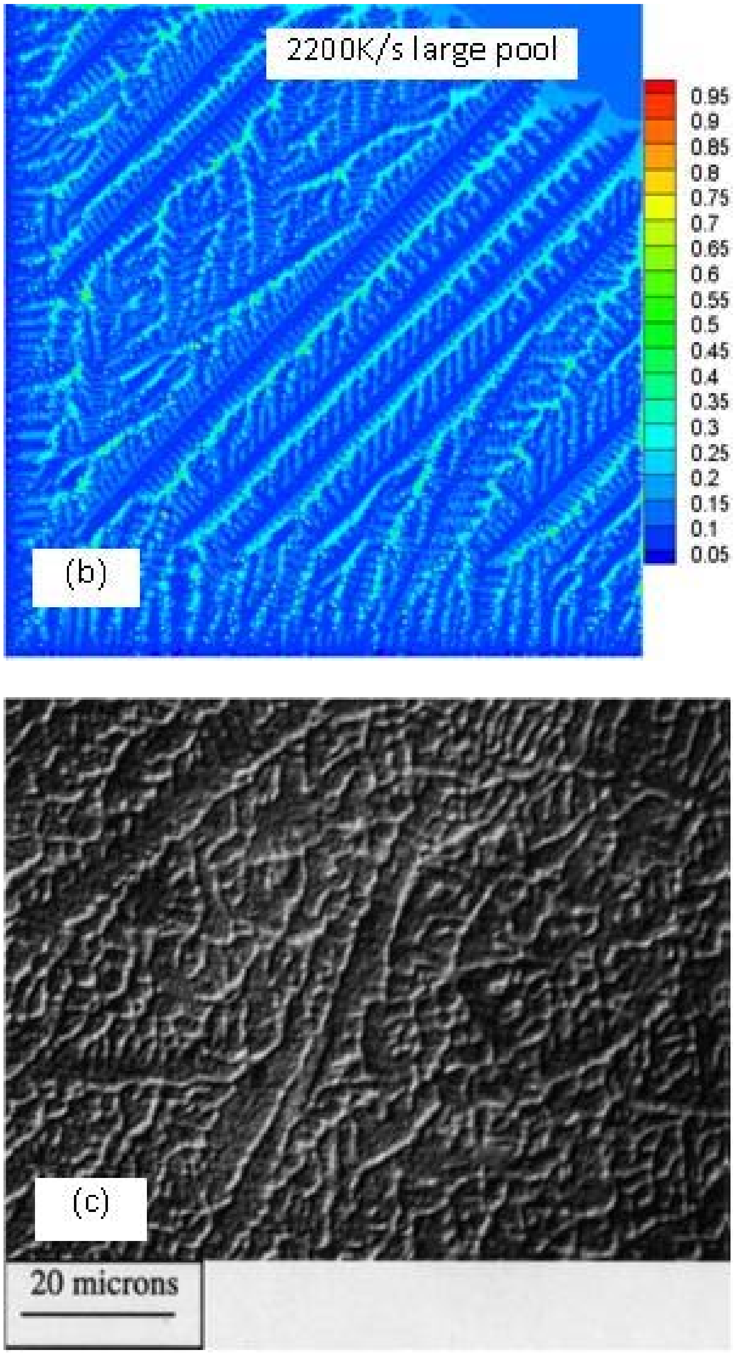

Figure 4.5 (Continued)

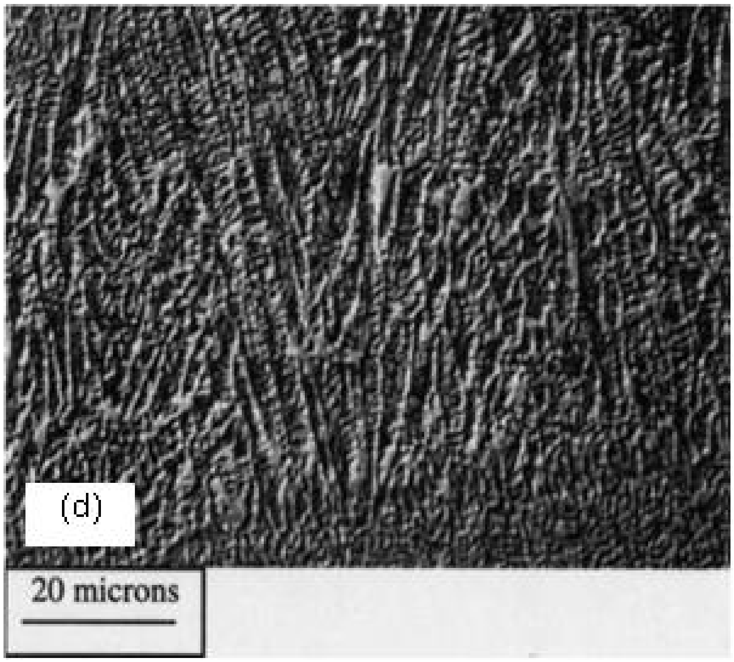

Figure 4.5 (Continued)

In Figure 4.6, I compare the simulated PDAS obtained by the present model for a layer thickness of 0.25mm and 0.5mm (hollow circles in Figure 4.6) with the data from Ref. [75], showing a very good agreement with the measured data. Microstructure of LENS deposited H13 with 1.37 mm (Figure 4.5(c)) and 0.25mm (Figure 4.5(d)) layer thickness, showing a finer dendritic structure for thinner layer [75].

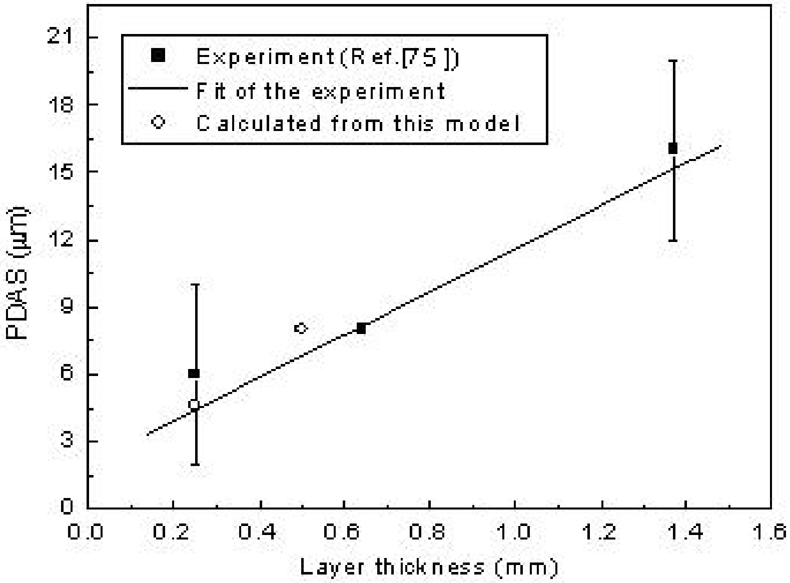

Figure 4.6 PDAS vs. layer thickness calculated from this model for alloy Fe-0.13wt%C and comparison with data for H13 from Ref. [75]

The experiments of Hofmeister *et al.* [16] showed that the cooling rates were substantially higher at low power levels when the molten zone was small. They also examined the microstructure of LENS deposited AISI316 for different laser power, reported in Table 4.1, which clearly shows a finer structure for lower laser power. Sparks *et al.* [91] measured the grain size of H13 Tool steel for different laser power, as listed in Table 4.2, again confirming the finer microstructure when laser power is reduced. All the above experimental reports support the simulated results obtained by our model. It must be noted that if the layer thickness is increased and the laser power is left unchanged, as it would usually occur in actual depositions, a higher cooling rate and finer dendrites would be obtained due to the rapid quenching effect of a larger powder feed rate.

Table 4.1 Laser power and grain mean intercept length [16]

Laser Power (W)	410	345	275	200	165	115
Mean intercept length (μm)	8.68	8.55	7.12	6.46	4.63	3.25

Table 4.2 Laser power and mean grain size [91]

Run order	Power (W)	Powder flow rate (grams/min)	Grain size (μm)	
			mean	stdev
1	750	6	6.43	2.86
4	1000	8	12.19	5.2

4.3.4 Substrate size and dendrite morphology

The effect of the size of the substrate on the microstructure is studied next by performing simulations of a single layer deposition on two substrates of thickness 5mm and 1.5mm. A laser speed of 5mm/s and a layer thickness of 0.5mm is used for both simulations. Figure 4.7 shows the simulated dendritic structures in the small square domain located in the lower region of the molten pool (see Figure 4.1(b)). It is observed that, as the substrate thickness decreases, more heat is extracted from the molten pool with higher temperture gradient because a constant temperature is set at the substrate bottom surface as boundary condition. Hence, a thin substrate results in higher cooling rate, which leads to fine dendrites with smaller PDAS and SDAS. These results agree with previous reports. Kobryn *et al.* [97] performed experiments to compare the grain width for thin and thick substrates, finding that grain width decreased for thinner substrates. They also concluded that this was due to a change in cooling rate produced by different substrate sizes. Hofmeister *et al.* [88] measured the microstructure at different locations for both AISI316 and H13 and observed that the mean intercept length was smaller at the initial layer than that at the layer 4mm above the substrate. The dendrites at the interface between the substrate and the molten pool was obtained by Pan *et al.* [77] with scanning speed of around 1.3mm/s. It can be said that a finer structure results from smaller substrates and that the preheat of the previous layers also exerts an influence on the microstructure evolution of the upper layers. Because of the high temperature gradient in the pool, the dendrites grow along the heat flow direction; the preferred crystal orientation of different grains also has remarkable influence on the direction of the growing dendrites.

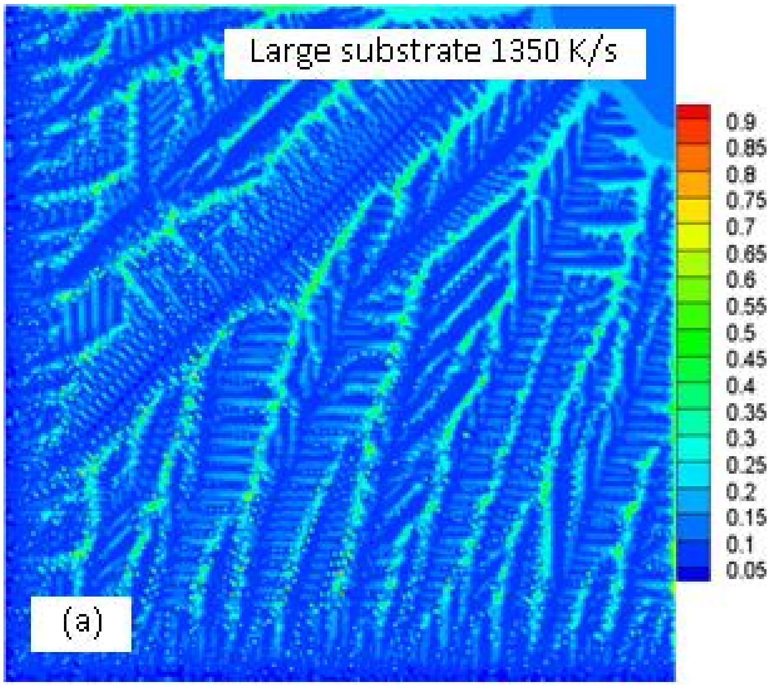

Figure 4.7 Dendritic structures for scan speed of 5mm/s and substrate thickness of (a) 5mm and (b) 1.5mm. Cooling rate is also shown. The color bar scale indicates solute concentration of C (wt%).(c) SEM micrograph of directionally solidified dendrites of copper alloy at the interface between the laser molten pool and the substrate (1.2-1.4mm/s) [77].

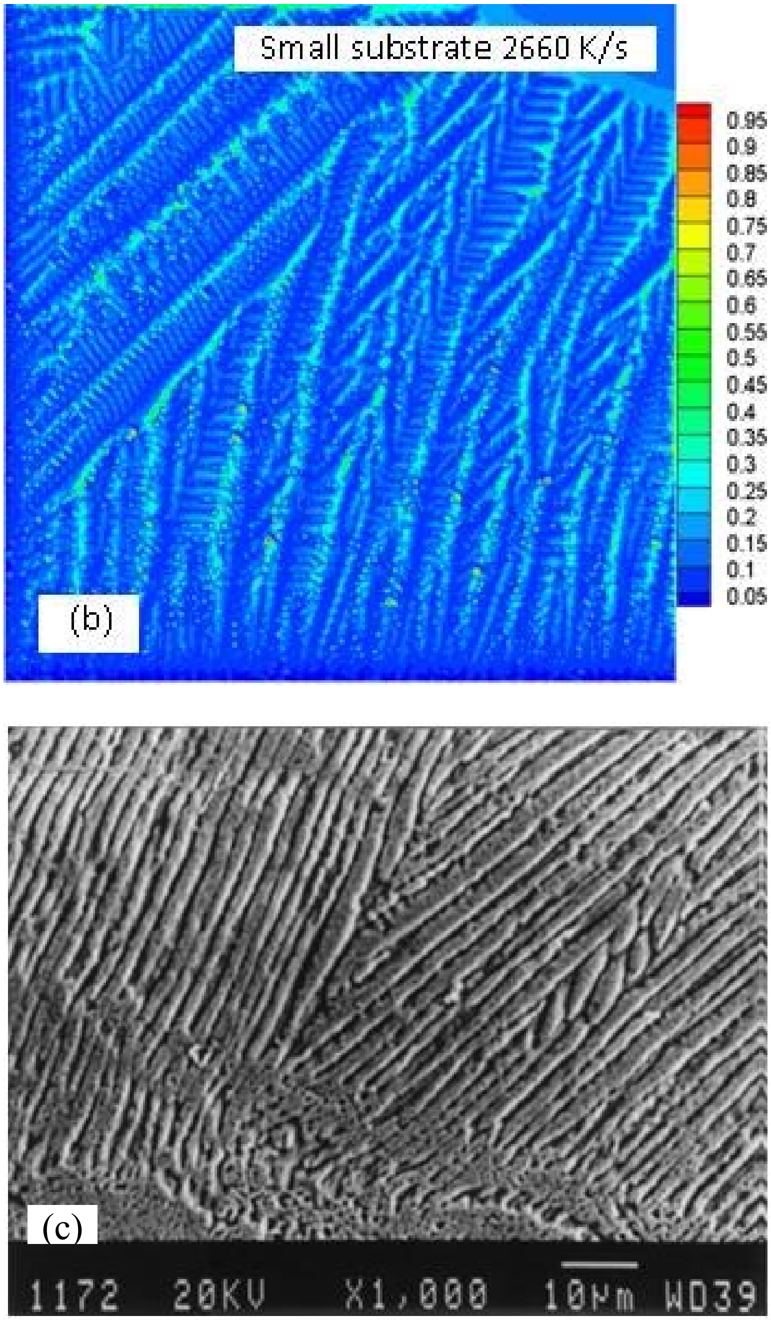

Figure 4.7 (Continued)

4.3.5 Dendrite morphology and temperature field at various locations

In this section, a comparison of simulated dendritic structures is performed for the two small square domains depicted in Figure 4.1(b), which represent locations close to the surface and the bottom of the molten pool. A thin 1.5mm thick substrate is used for all the simulations in this section. Figure 4.8(a) and (b) show the dendrite structure and temperature field for the square domain located next to the pool surface (referred as “top domain”), while Figure 4.8(c) and (d) show the same variables for the square domain located at the bottom of the molten pool (referred as “bottom domain”). A laser moving speed of 5mm/s is used for both simulations. A similar calculation in the bottom domain for a laser speed of 10mm/s produces the results shown in Figure 4.8(e) and (f).

Due to the nature of competitive dendrite growth for metals or alloys with cubic crystal structure, the developed columnar grains are oriented with the preferential direction <100>, being parallel to the direction of the highest temperature gradient. The growth of columnar grains occurs trying to follow the highest temperature gradient, while still maintaining their preferred direction, as observed in Figure 4.8. Some grains are stopped by other grains with preferential directions parallel to the highest temperature gradient direction. At the location close to the pool surface (“upper domain”), the highest temperature gradient is nearly along the laser movement direction (horizontal), as shown in Figure 4.8(b). At the bottom domain, with the combined effect of the laser beam moving direction and the heat conduction direction through the substrate, the maximum temperature gradient direction is nearly upright, as shown in Figure 4.8(d). When the speed of the laser beam increases to 10mm/s, the maximum temperature gradient direction moves closer toward the laser beam moving direction, as shown in Figure 4.8(f).

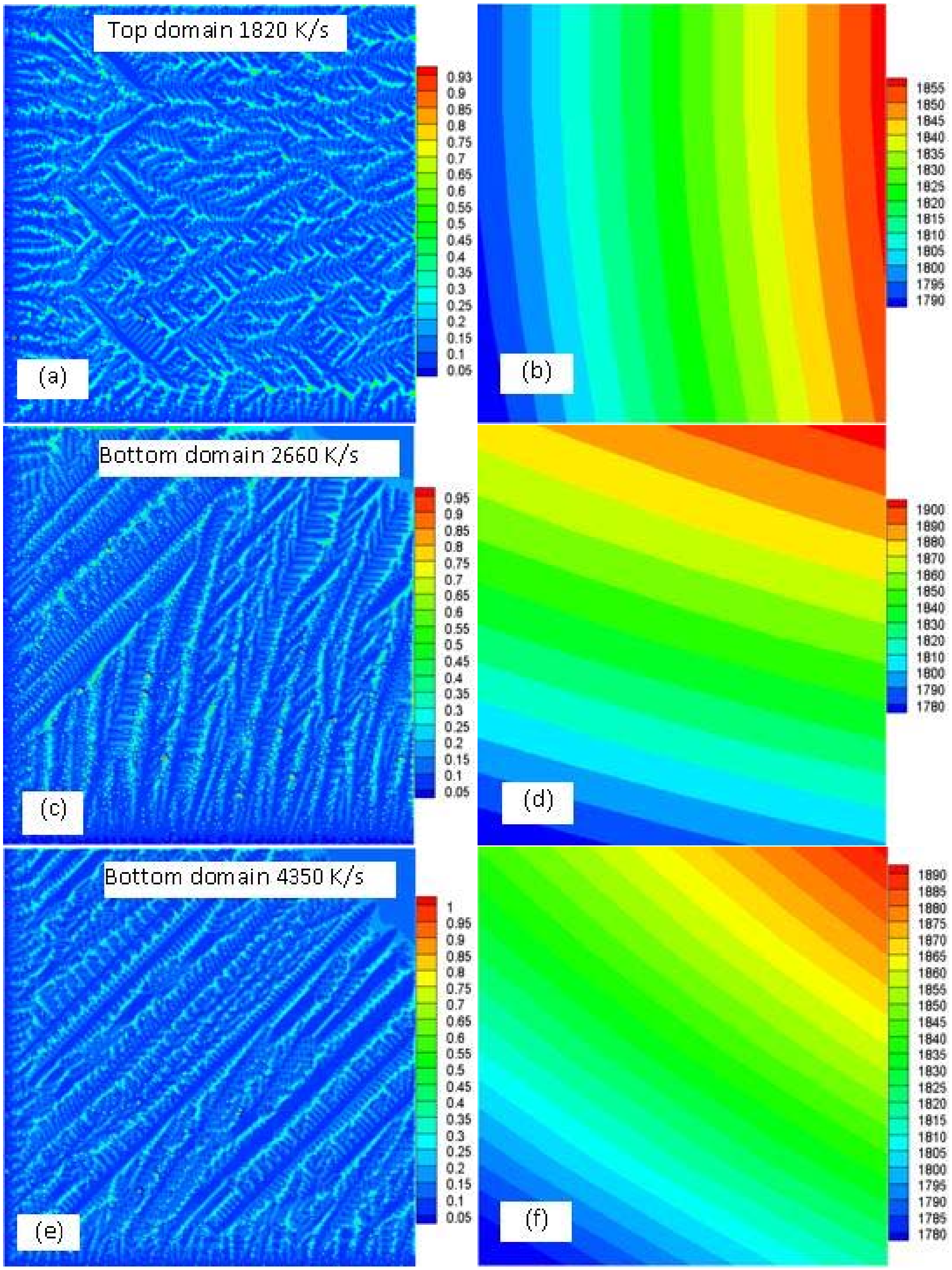

Figure 4.8 (a) Dendrite morphology and (b) temperature field at the upper domain with laser speed 5mm/s. (c) Dendrite morphology and (d) temperature field at the bottom domain with laser speed 5mm/s. (e) Dendrite morphology and (f) temperature field at the bottom domain with laser speed 10mm/s. Color bars show solute concentration of C in wt% and temperature in K.

The above simulated results are consistent with previously reported experiments [73, 59] showing that the grain growth direction varies at different locations of deposited parts. Choi and Chang [73] reported a near horizontal columnar structure at the top surface with a layer thickness of 0.245mm, while in the bottom region the dendrites were usually perpendicular to the layer boundaries, i.e., along the direction of higher temperature gradient as Figure 4.9 shows. From Figure 4.8 and 4.9, it is easily seen that preferential orientation and heat flow direction both exert influence on the dendrite growth direction.

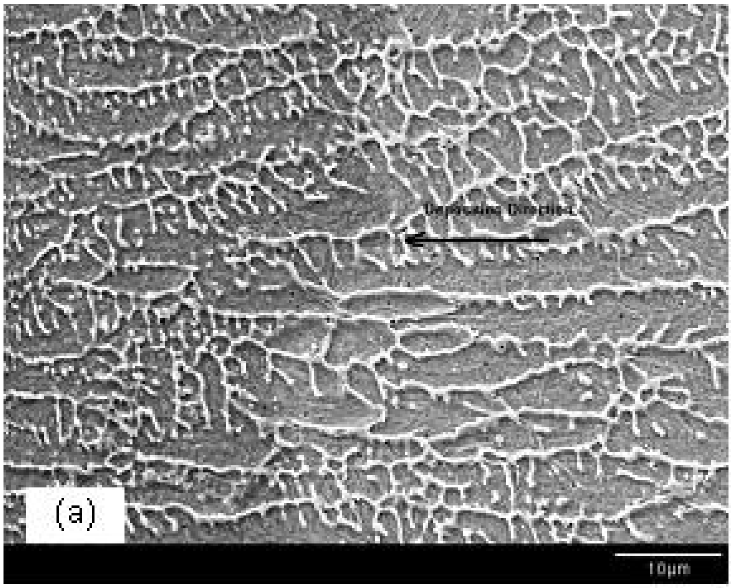

Figure 4.9 Columnar dendrites (a) near the top surface with growth direction along with deposition direction and (b) at the interface between two consecutive clad layers [73].

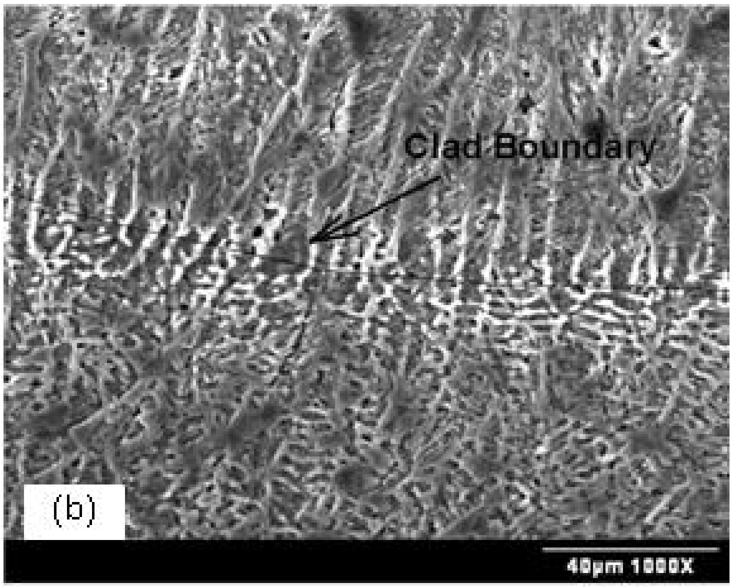

Figure 4.9 (Continued)

4.4 Conclusions

This work presented a new multiscale model to simulate the dendritic structure during solidification of a Fe-C alloy in the molten pool of the LENS laser deposition process. The model solved the energy equation by the FE method to calculate the temperature distribution in a macro region around the melt pool during deposition of one layer. The temperature field was then transferred to a micro region inside the mushy zone of the pool, where solute microsegregation and dendrite growth was calculated with a combined FE + CA technique. The effect of several process conditions on the solidification microstructure was investigated, in particular, laser moving speed, layer thickness, and substrate size. Confirming reports of previous experimental works, dendrite growth could occur even at the high cooling rates of the LENS process, with DAS as small as a few microns. A columnar growth from the bottom of the pool was observed, with varying DAS and orientation depending on the location in the pool and the moving speed of laser beam. For the highest laser speeds, secondary and tertiary arms could not form and a dendrite to cellular transition was observed. Calculated values of DAS and simulated microstructure variation with laser scanning speed, layer thickness and substrate size agreed rather well with previous observations. In its present stage, the model did not include convection, which would be a desirable extension given the strong Marangoni flow produced by the high temperature gradients in the melt pool. It must also be observed that, although I addressed multilayer deposition in previous chapters [167-169], the work described in this chapter was focused on the smaller scale of dendrite growth, which would become much more difficult in a multilayer setting. Therefore, the results of this work were relevant after a layer has been deposited. When more layers are deposited on top, dendrites will coarsen and may even remelt. Microstructure evolution during the thermal cycles and solid-solid phase transformation should be considered. In spite of these limitations, the developed model is a useful tool to study the response of the solidification microstructure to changes in process parameters. The calculated microstructure can also serve as an initial condition for a model that simulates solid phase transformations during subsequent cooling after solidification.

The work of this chapter was published in the Acta materialia in 2010 [171] and was also pre-viewed and presented in the conference TMS 2010 [172].

CHAPTER V

A CELLULAR AUTOMATON MODEL FOR DENDRITE GROWTH IN ALLOY AZ91

5.1 Background and introduction

In the last decade, numerical simulation has been widely used to predict microstructural changes during solidification in alloys. But most of the published papers in this area of research focus on dendritic growth of cubic crystal materials during solidification. Bottger *et al*. [173] used the PF method to simulate the microstructure during the equiaxed solidification of hexagonal crystal materials, particularly the magnesium alloy AZ31, but their results did not show the single dendritic morphology with six-fold symmetry. Liu *et al*. [174] simulated the 2D dendrite profiles by employing a mathematical construction method. But this mathematical description method of the grain contour did not consider the tertiary and above arm branching.

In this chapter, a model coupling the CA and FE methods is developed to simulate the dendritic growth of hexagonal metals during the solidification process. The model is applied to the simulation of small specimens with equiaxed and columnar grain growth under directional solidification, showing good performance in avoiding mesh-induced anisotropy. For the case of dendrite growth in a binary Mg-8.9wt%Al alloy, a simulated microstructure with perfect six-fold symmetry is obtained. The influences of certain factors on dendrite morphology, including cooling rate, mesh size, undercooling, surface tension, and anisotropy coefficient are discussed. Although the model is capable of predicting the six-fold geometry of the HCP crystal structure, in the present version the dendrite growth is limited to the grid orientation and arbitrary orientations are not currently possible.

5.2 Model development

5.2.1 Introduction to Mg-alloy dendrite growth simulation

The dendrite growth for Mg-8.9wt%Al alloy, which is similar in composition to alloy AZ91, is simulated. The properties of this alloy in the simulations are listed in Table A.3 in Appendix A [175-177]. Magnesium is a material with a HCP crystal structure, and its dendrite structural sketch can be found in Ref. [178] as shown in Figure 5.1.

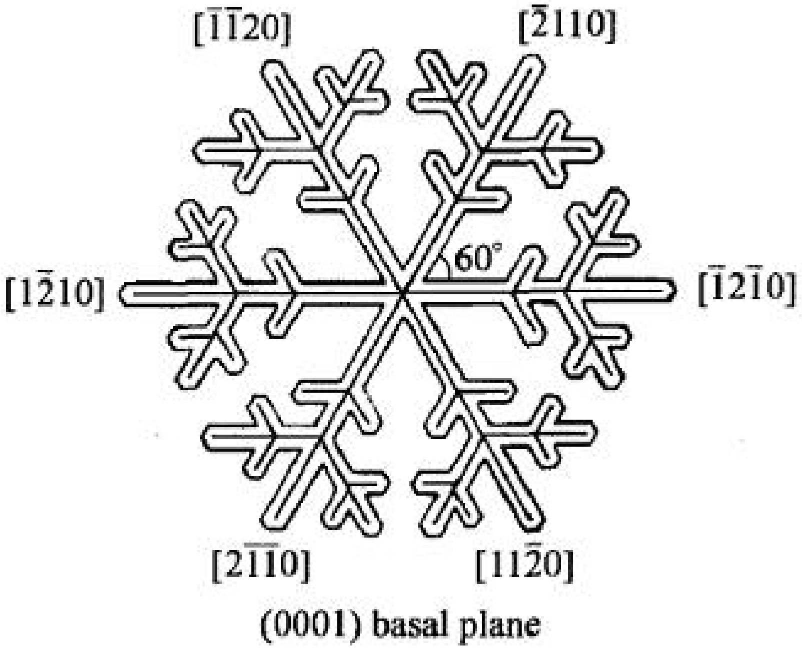

Figure 5.1 Dendritic structural schematics of basal plane of hexagonal crystal material: Mg

5.2.2 Temperature field and solute distribution calculation

The 2D transient differential equation governing the heat transfer within the calculation domain is given by:

$$\frac{\partial T}{\partial t} = \alpha \cdot \nabla^2 T + \frac{L}{\rho C_P}\frac{\partial f_S}{\partial t} \tag{Eq.5.1}$$

Where T is temperature, t is time, α is thermal diffusivity, L is latent heat of solidification, ρ is density, C_P is specific heat, and f_s is volume solid fraction. A forced boundary condition, heat flux q, is prescribed on the four walls (equiaxed grain growth simulation) or single wall (columnar grain growth simulation) as shown below:

$$q = -\lambda \frac{\partial T}{\partial n} \tag{Eq.5.2}$$

Where λ is the thermal conductivity; and n is the outward direction normal to the boundary. The FE method is employed to solve the Eq.5.1 and Eq.5.2 and thus obtaining the temperature field.

The calculation of solute distribution in solid and liquid phases and the concentration in solid/liquid interface can refer to the Chapter IV.

5.2.3 Kinetics parameters for the CA model

The solute distribution ahead of the interface is used as a driving force to simulate the dendrite growth in the CA model. The process of dendrite growth is predominantly controlled by the difference between the local interface equilibrium solute concentration and the local actual liquid solute concentration. The changing rate of solid fraction determines the velocity and morphology of grain growth. Based on the calculation of the local actual liquid concentration c_l from Eq.4.1 and the interface equilibrium composition c_l^* the increase of solid fraction, Δf_s at the interface cells can be obtained as:

$$\Delta f_s = (c_l^* - c_l)/\left(c_l^* \cdot (1-k)\right) \qquad \text{(Eq.5.3)}$$

The interface equilibrium composition is calculated by:

$$c_l^* = c_0 + \frac{T^* - T_l^{eq} + \Gamma \mathrm{K} \cdot f(\varphi, \theta_0)}{m_l} \qquad \text{(Eq.5.4)}$$

Where c_0 is the initial solute concentration, T_l^{eq} is the equilibrium liquidus temperature at the initial solute concentration, m_l is the liquidus slope, Γ is the Gibbs-Thomson coefficient, and K is the curvature of the S/L interface. The function accounting for the anisotropy of the surface tension is denoted by $f(\varphi, \theta_0)$ where φ is the growth angle between the normal to the interface and the x-axis, and θ_0 is the angle of the preferential growth direction with respect to the x-axis. The interface equilibrium temperature calculated by Eq.5.1 is denoted by T^*.

For hexagonal crystals, the function $f(\varphi, \theta_0)$ exhibits a six-fold anisotropy [173, 179]:

$$f(\varphi, \theta_0) = 1 - \delta \cdot \cos[6 \cdot (\varphi - \theta_0)] \qquad \text{(Eq.5.5)}$$

Where δ is the anisotropy coefficient, and the growth angle can be calculated from the following equation:

$$\varphi = \begin{cases} \cos^{-1}\left(\frac{\partial f_s/\partial x}{((\partial f_s/\partial x)^2 + (\partial f_s/\partial y)^2)^{1/2}}\right) & \frac{\partial f_s}{\partial y} \geq 0 \\ 2\pi - \cos^{-1}\left(\frac{\partial f_s/\partial x}{((\partial f_s/\partial x)^2 + (\partial f_s/\partial y)^2)^{1/2}}\right) & \frac{\partial f_s}{\partial y} < 0 \end{cases} \qquad \text{(Eq.5.6)}$$

The interface curvature of a cell with solid fraction f_s can be obtained by counting the nearest and second nearest neighboring cells [139], and it also shown in chapter IV, but for hexagonal mesh, $N = 19$:

Different time steps, Δt_T and Δt_c, are used for the calculation of heat transfer and mass transfer, respectively:

$$\Delta t_T = \frac{\rho C_P (m \cdot a)^2}{4.5\lambda} \qquad \text{(Eq.5.7a)}$$

$$\Delta t_c = \frac{a^2}{4.5 D_l} \qquad \text{(Eq.5.7b)}$$

Since the heat diffusivity is much faster than the solute diffusivity, Eq.5.1 is solved N_t ($N_t = \Delta t_c / \Delta t_T$) times with time step Δt_T, per each solution of Eq.4.1 with time step Δt_c in order to obtain converged temperature and solute concentration fields.

5.2.4 The rules of capturing interface cells

Each cell has three possible states: solid, liquid, and interface (partially solidified). Figure 5.2 shows a sketch of the grain growth model, illustrated for the case of a HCP structure material [130]. Because a HCP crystal material grows following six preferred directions and has a six-fold symmetry, a hexagon-shape solid seed is initially placed at the center of a cell and the seed is allowed to grow along its diagonals. Once the corners of the hexagon seed reach any of the six neighboring cells, the neighbor cell will be changed to an interface cell. A new hexagon seed, having the same preferential crystallographic orientation as the original cell, is generated and placed at the center of the new interface cell. The new hexagon seed starts to grow according to the change of the solid fraction in the new interface cell. After the original hexagon has changed all the neighboring cells into interface cells, the original cell continues to grow until its solid fraction becomes unity, after which the state of the original cell becomes solid and changes any surrounding liquid cells into interface cells. The length of the diagonal (d_s) of the seed is calculated based on the solid fraction f_s.

$$d_s = \frac{k_d \cdot f_s \cdot a}{\cos \theta_0} \qquad \text{(Eq.5.8)}$$

Where k_d is the diagonal length coefficient, and a is the cell side size.

5.2.5 Numerical implementation procedures

The simulation of the grain growth process can be summarized in the following steps:

(1) Solve Eq.5.1 to obtain the temperature field in the domain using time step Δt_T for N_t iterations with constant heat flux as boundary condition;

(2) Interpolate in each FE to obtain the temperature for all cells inside the element and then solve the Eq.4.1 with time step to obtain the solute field in the whole domain;

(3) Calculate the increase of solid fraction at the interface cells;

(4) Update the thermal field and solute fields based on the release of latent heat and the rejection of solute during solidification;

(5) Use the CA transition rules to capture the new interface cells.

5.3 Proposition of hexagonal mesh generation

A single nucleus with the preferential orientation of 0 degree is put at the center in the calculation domain (100×100μm) with regular FE mesh of quadrilateral bilinear elements. Figure 5.2(a) shows a sketch of the growth algorithm. Due to the hexagonal shape of magnesium crystal structure, I select a hexagonal-shaped seed which grows in six directions. When any of the seed diagonal reaches a neighboring cell, a new seed is placed at the center of this cell. The calculated composition field for a single equiaxed crystal is shown in Figure 5.2(b). It is observed that there are six primary arms, but the angle between the primary arms is not 60 degrees. Some arms grow aligning with the axis of the mesh, and others grow at 45 degrees. They should grow with perfect six-fold symmetrical, without hindrance from other grains or walls. Fu *et al*. [178] also experienced a similar problem and they attributed it to the methodology of defining neighboring cells as shown in Figure 5.2(c).

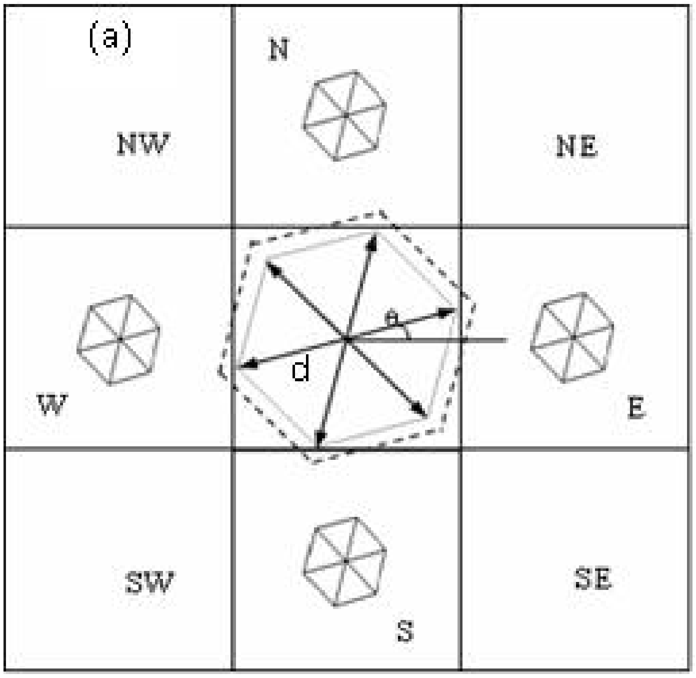

Figure 5.2 (a) Sketch of growth algorithm for hexagonal crystal material, (b) single equiaxed grain morphology during solidification of Mg alloy, and (c) single equiaxed grain growth calculated in Ref. [178]

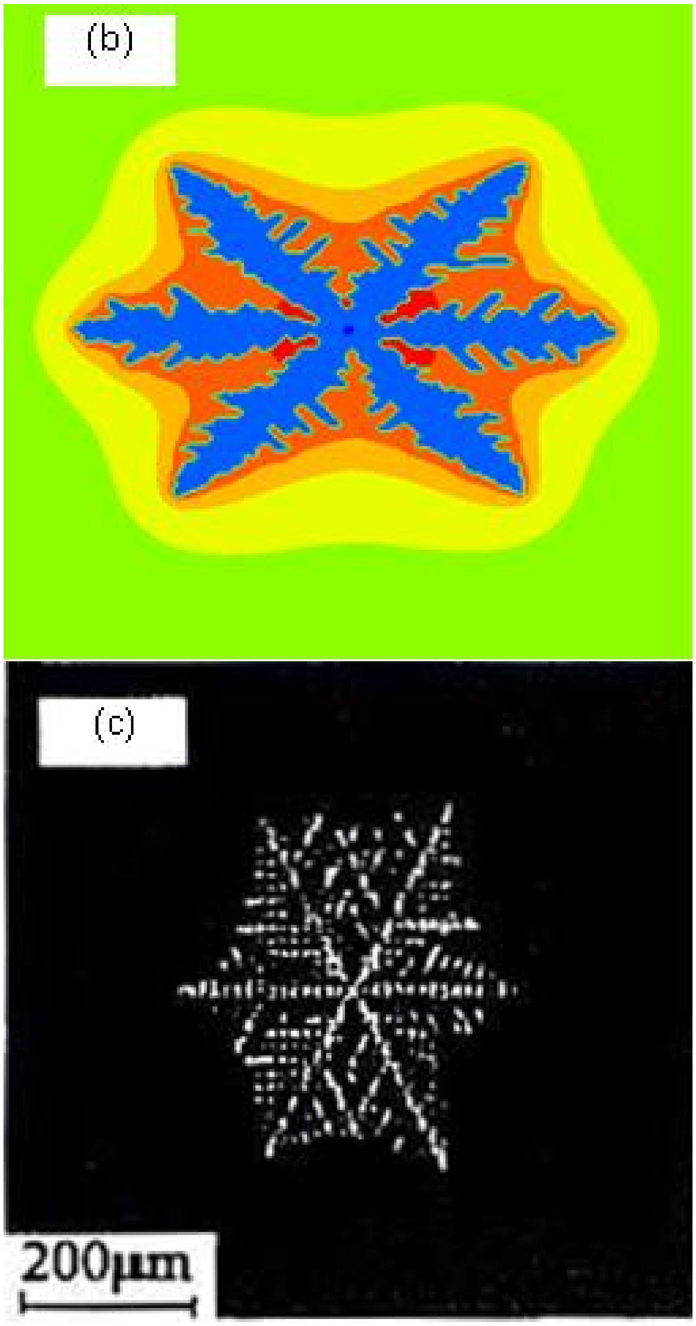

Figure 5.2 (Continued)

As evidenced in the previous example, the CA method used to simulate dendrite evolution has a disadvantage: grid dependent anisotropy [132, 180], which is that the grain growth process is very sensitive to the mesh shape and mesh size. For the simulation of dendrite growth with cubic crystal structure materials, meshes of rectangular elements have been widely used, and hexagonal meshes have also been introduced by some articles using PF methods [181, 182]. Based on the fact that Mg has an HCP crystal structure with six-fold symmetry and previous reports that the use of hexagonal elements seems to reduce mesh-induced anisotropy [180, 183], a FE mesh consisting of hexagonal elements is developed to solve this problem with the CA technique. A sketch of the mesh for thermal diffusion and CA calculations is shown respectively in Figure 5.3(a) and (b). The model is described in the following sections.

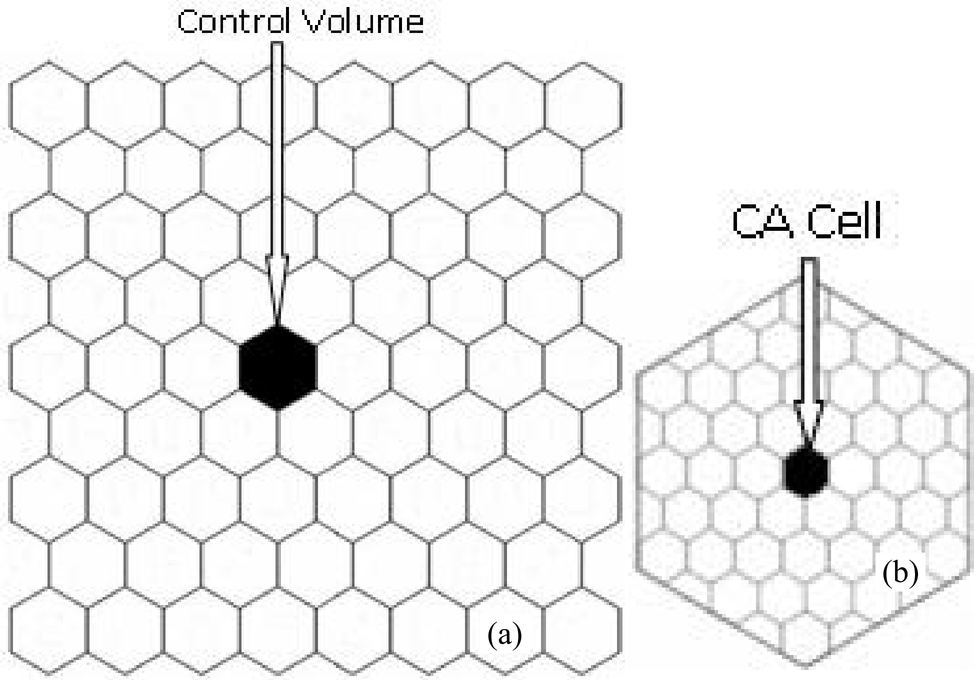

Figure 5.3 (a) Finite element hexagonal mesh for heat diffusion, and (b) cellular network for solute transfer and grain growth in the CA method

5.4 Model validation

The relationship between the PDAS and SDAS with the cooling rate has been amply documented and empirical relations have been proposed for several alloy systems

[162, 184]. Using our developed model, I simulate the growth of an individual dendrite under several intensities of cooling rate. The SDAS is then recorded for different values of cooling rate and plotted in Figure 5.4. The data on SDAS vs. cooling rate previously reported by Caceres *et al.* [185], Labrecque *et al.* [186], Dube *et al.* [187], and Sequeira *et al.* [188] are also included in Figure 5.4, showing a reasonable agreement with my calculated values.

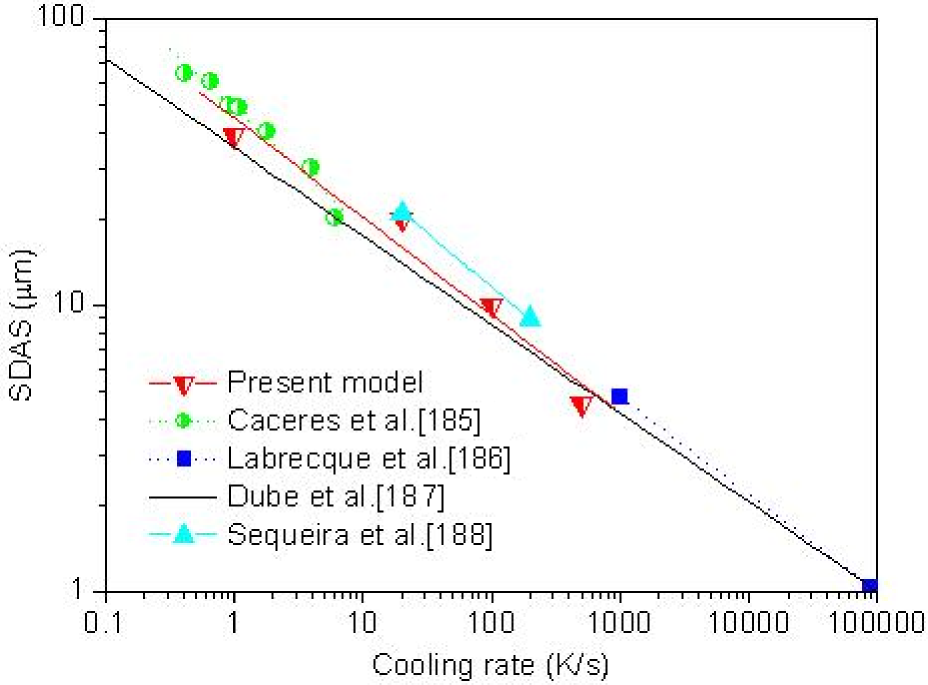

Figure 5.4 SDAS vs. cooling rate for alloy AZ91 calculated by the present model and comparison with the data from Refs. [185-188]

Lipton, Glicksman and Kurz [189] developed an analytical model (the LGK model) which described free dendrite growth at a given melt undercooling. The tip growth velocity with various undercoolings calculated by the LGK theory is shown in Figure 5.5, alongside values calculated by the present CA model. It is observed that our simulation results follow rather well the LGK predictions. It can also be observed that increasing the cooling rate enhances the branching of the dendrite arms, which is in agreement with the calculations reported by Bottger *et al*. [173] using the PF method.

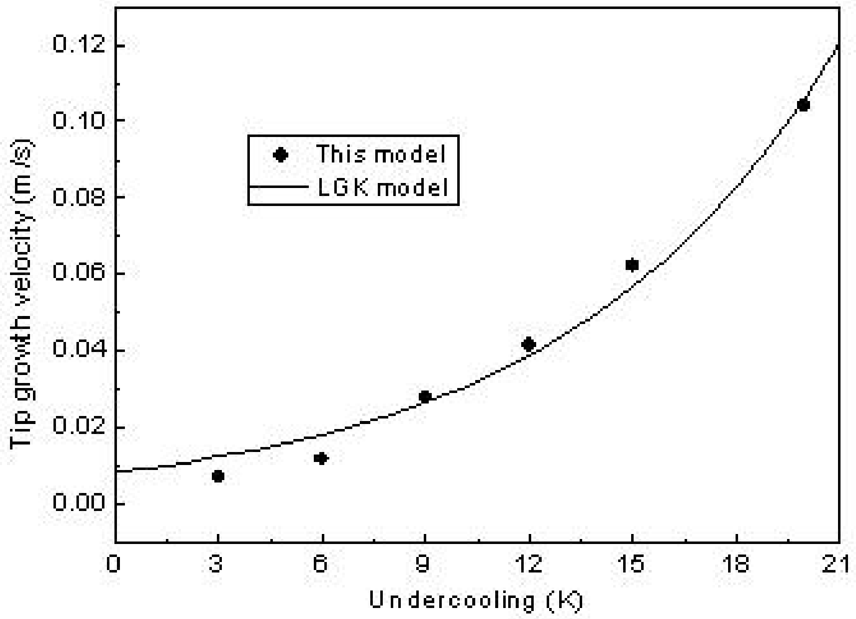

Figure 5.5 Tip growth velocity vs. undercooling calculated by the present model and comparison with the LGK theory [189].

5.5 Simulation results

A single nucleus is set at the calculation domain center to simulate the grain growth process during solidification. With constant heat flux (10kW/m^2), the calculation domain has uniform initial temperature and composition. The nucleus has an initial composition kC_0 and preferred growth orientations of zero degree with respect to the horizontal direction. The square domain has a 400×400 mesh with side lengths of 0.5µm. Figure 5.6(a), (b), and (c) show the simulated evolution of equiaxed dendrite growth at different simulation times of 0.0212s, 0.0424s, and 0.0636s, respectively. It can be seen that in the early stages of solidification, dendrites develop primary arms which follow the crystallographic orientations as shown in Figure 5.6(a). As solidification proceeds, the primary arms become larger and the secondary arms begin to occur (Figure 5.6(b)). With further solidification, some tertiary dendritic arms form on the secondary arms (Figure 5.6(c)). The simulated structure compares qualitatively well with the measured microstructure of an AZ91 dendrite reported in [178] as Figure 5.6(d) shows.

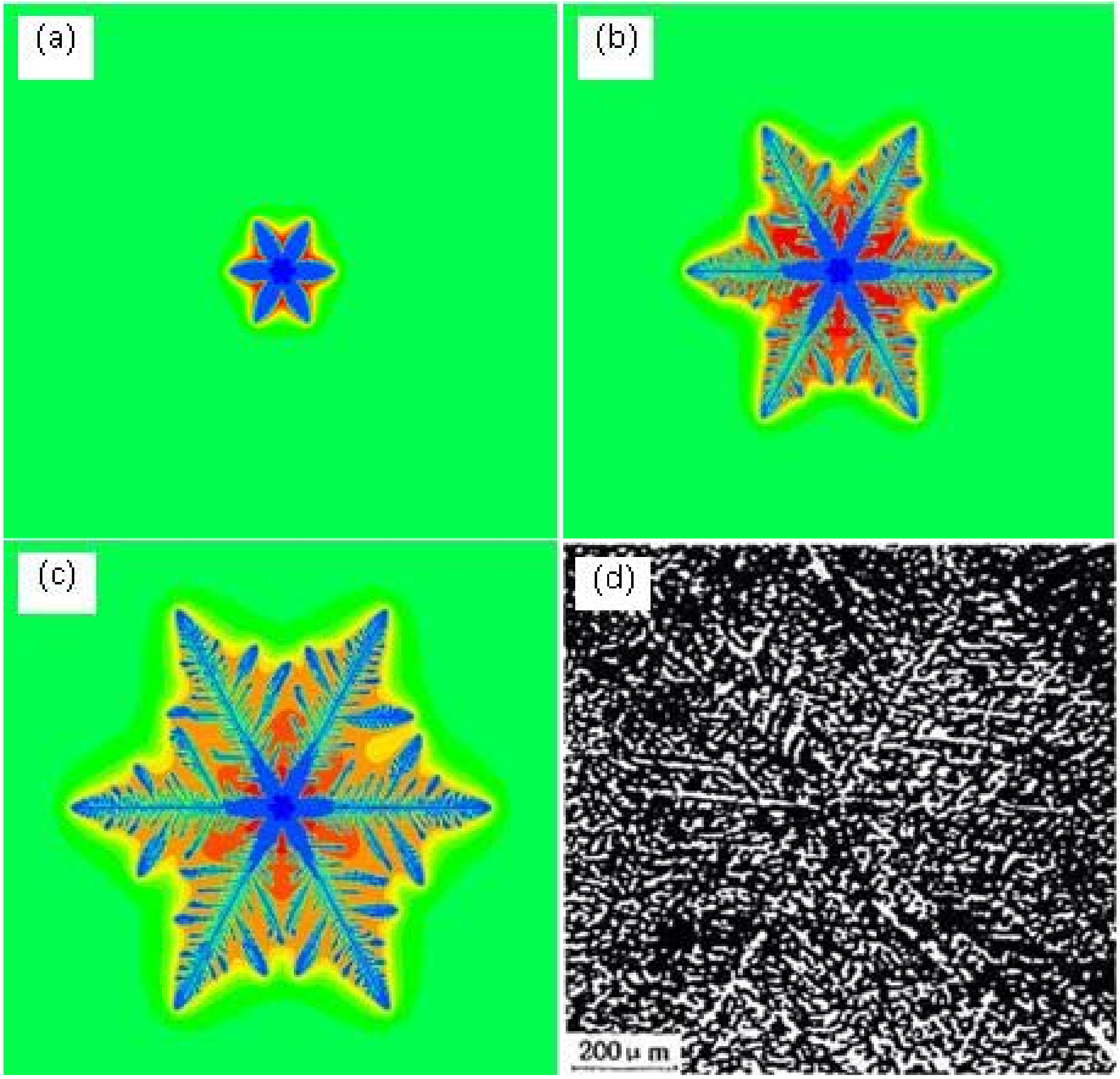

Figure 5.6 Solute map at different simulation times: (a) 0.0212s, (b) 0.0424s, (c) 0.0636s and (d) the measured microstructure of AZ91D dendrite [178]

In the following, a set of numerical simulations are performed to illustrate the influence of mesh size on the simulated dendrite structure. A square domain is generated with the four walls being cooled at a constant heat flux of 10kW/m^2. Figure 5.7 shows the solute maps with meshes of 200×200 (1μm element size), 400×400 (0.5μm), and 600×600 (0.33μm), respectively, each having a simulation time of 0.0636s. A single grain is initially placed at the center of the domain with uniform composition kC_0. No tertiary arms occur from the secondary arms in Figure 5.7(a); however, tertiary arms can be seen in Figure 5.7(b) and (c). The arm trunk is thinner in Figure 5.7(c) than that in Figure 5.7(b). In addition, the maximum composition obtained with the simulation in a coarse mesh is higher than that in fine mesh. Based on these figures, it is evident that mesh size affects the grain morphology; therefore, using a sufficiently fine mesh size is necessary to obtain converged results. In the remaining calculations, meshes with hexagonal cell sides of 0.25μm are employed to save computational time without losing significant accuracy of results.

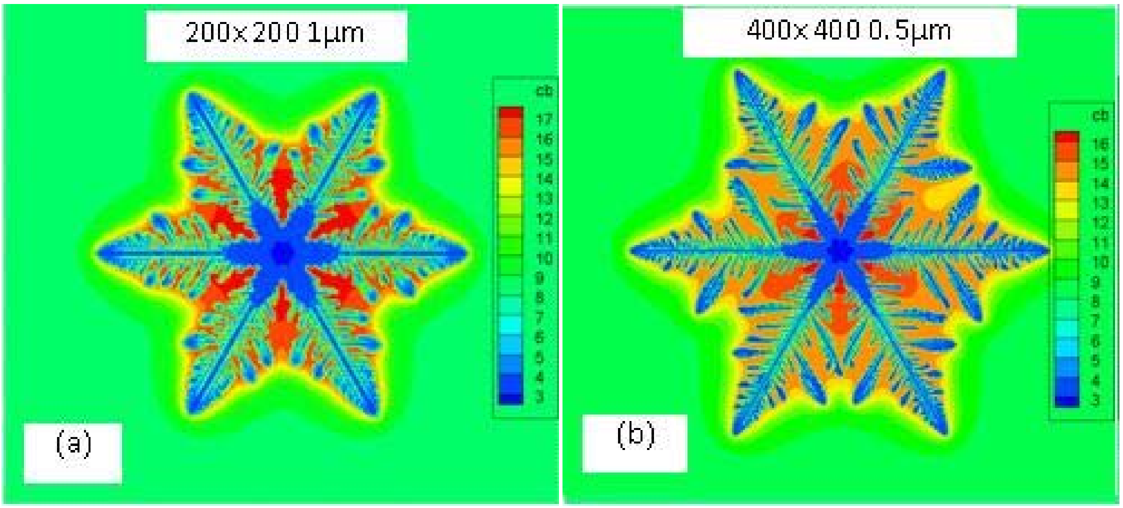

Figure 5.7 Solute map calculated with different mesh sizes: (a) 1.0μm, (b) 0.5μm and (c) 0.33μm

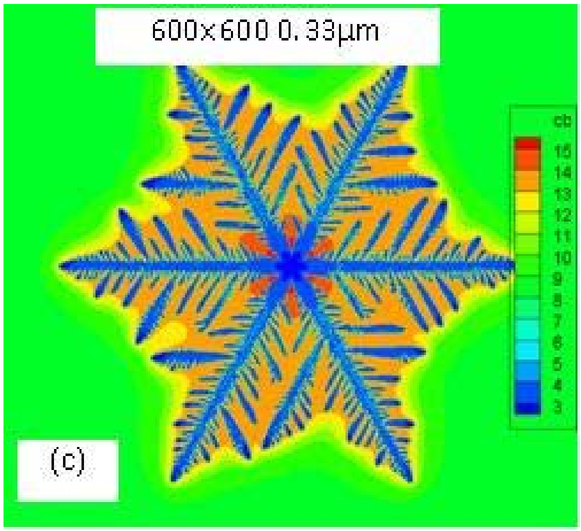

Figure 5.7 (Continued)

Four simulation cases with different magnitudes of the heat flux are performed in order to observe the influence of cooling rate on dendrite morphology. The calculation domains have the same 400×400 mesh with cell side lengths of 0.25μm. Large heat flux corresponds to a high cooling rate. Increasing the heat flux speeds up dendrite growth, but it is observed in Figure 5.8 that the primary arms have similar lengths for different cooling rates, which is due to the smaller simulation time corresponding to higher cooling rates. With lower cooling rates, the secondary arms have shorter lengths and eventually dissipate. When the heat flux is 2kW/m^2, only a few secondary arms occur as is shown in Figure 5.8(d). Since a larger heat flux increases the speed of grain growth, more solute is released from the solid and there is less time for solute diffusion, which increases the maximum composition in the liquid. Bottger *et al.* simulated the solidification microstructure of AZ31 by the PF method, and they found that the stronger cooling resulted in a higher branching of the dendrite arms [173] as shown in Figure 5.8(f). By comparison with the Figure 5.8(a) and (d), this model gives similar results.

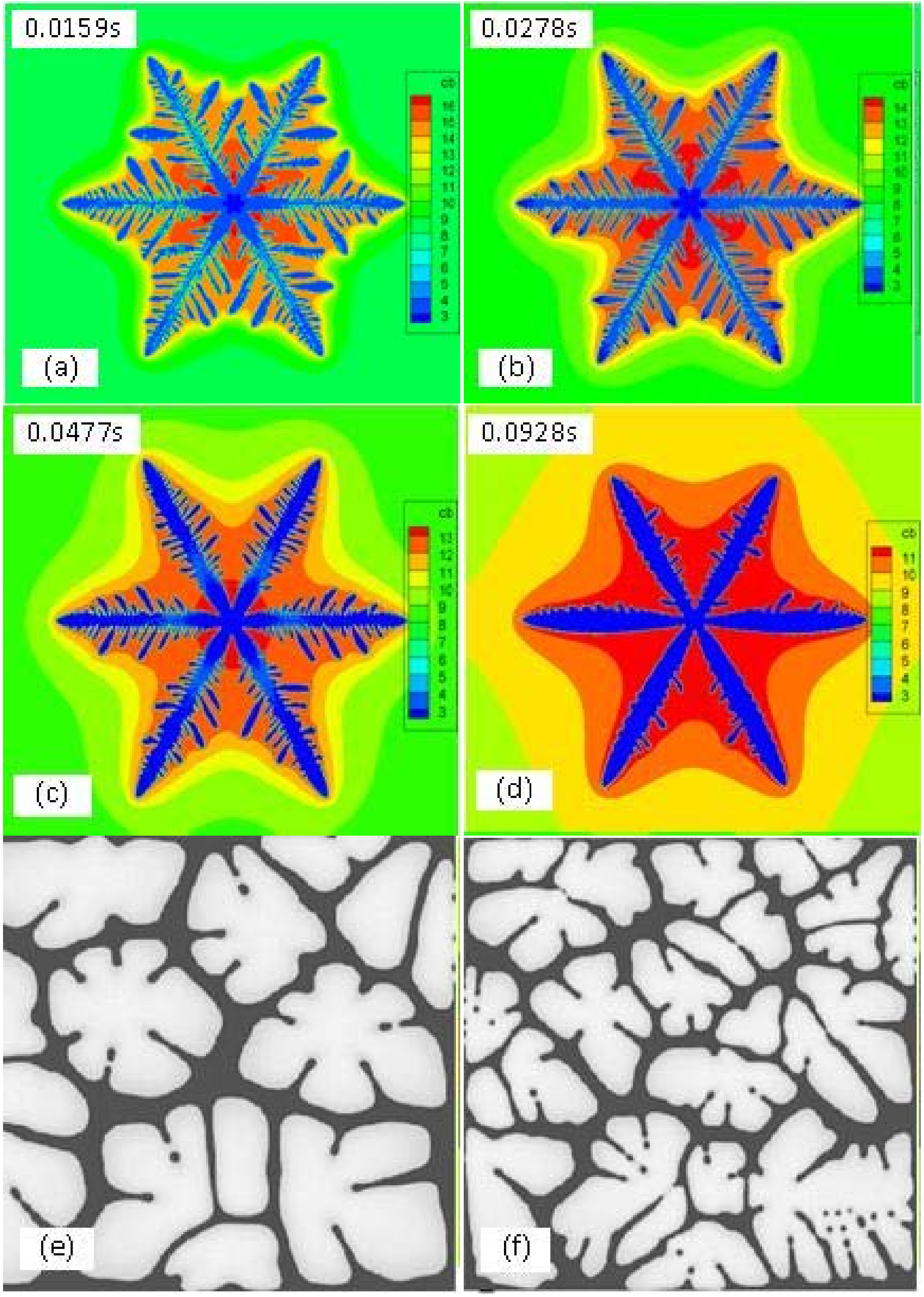

Figure 5.8 Solute map with various heat fluxes imposed at the four walls: (a) 20kW/m^2, (b) 10kW/m^2, (c) 5kW/m^2, and (d) 2kW/m^2; Equiaxed solidification with parameter variation: (e) AZ31 reference, (f) enhanced heat extraction rate (from 25(e) to 100Jcm^{-3}s^{-1}(f)) [173]

To demonstrate the influence of undercooling on dendrite growth, two simulations are conducted with undercoolings of 20K and 4K, with corresponding simulation times of 0.0053s and 0.0080s. The calculation domain, with a nuclei having preferential crystallographic orientation of zero degrees at its center, has a 400×400 mesh with cell side lengths of 0.25μm. The larger circles in both Figure 5.9(a) and (b) respectively represent the dendrite envelopes with undercoolings at 20K and 4K. The solid circles show the locations where the grains begin to bifurcate to form primary arms. It is noticed that the larger undercooling helps the formation of the primary arms. Smaller undercooling leads to lower velocity of grain growth, which results in more time for the transfer of solute from the S/L interface to the bulk liquid region. This is the reason that small undercooling results in lower maximum composition.

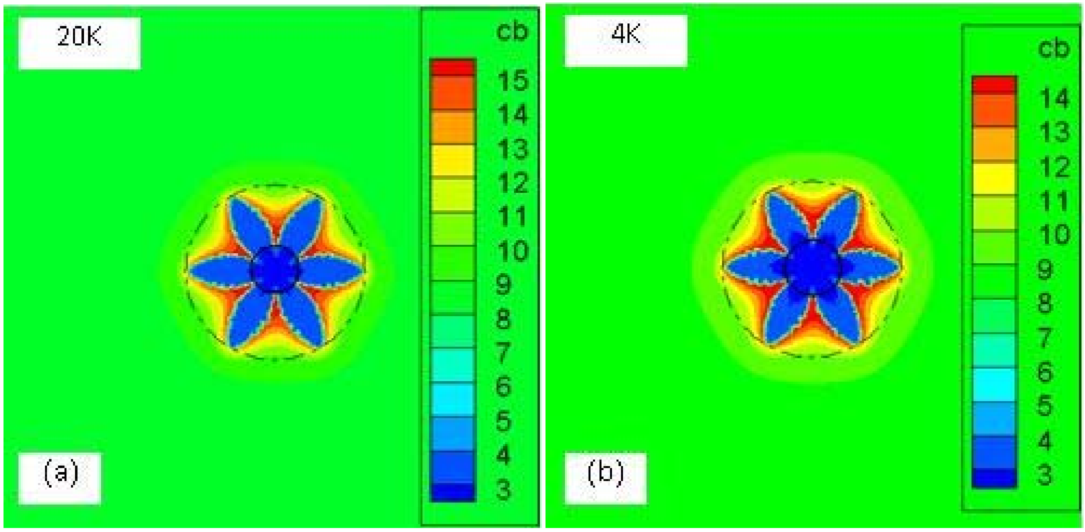

Figure 5.9 Solute map for undercooling of (a) 20K and (b) 4K

Figure 5.10 shows simulations with two different values of the Gibbs-Thomson coefficient for the same simulation time of 0.0238s and with the same parameters used in the previous calculations. The calculation domain has a 400×400 mesh with cell sides of

0.25μm. The Gibbs-Thomson coefficients for Figure 5.10(a) and (b) are 4.0×10^{-7}K•m and 0.5×10^{-7}K•m, respectively. By comparing the simulation results, the influence of the Gibbs-Thomson coefficient on the grain morphology can be observed. The lengths of the primary and secondary arms do not change much when increasing the coefficient. However, a larger Gibbs-Thomson coefficient results in a higher volume of solid (shown in blue in Figure 5.10). Also, it is observed that less branching takes place for the case of higher surface tension, a trend also reported in Ref. [182].

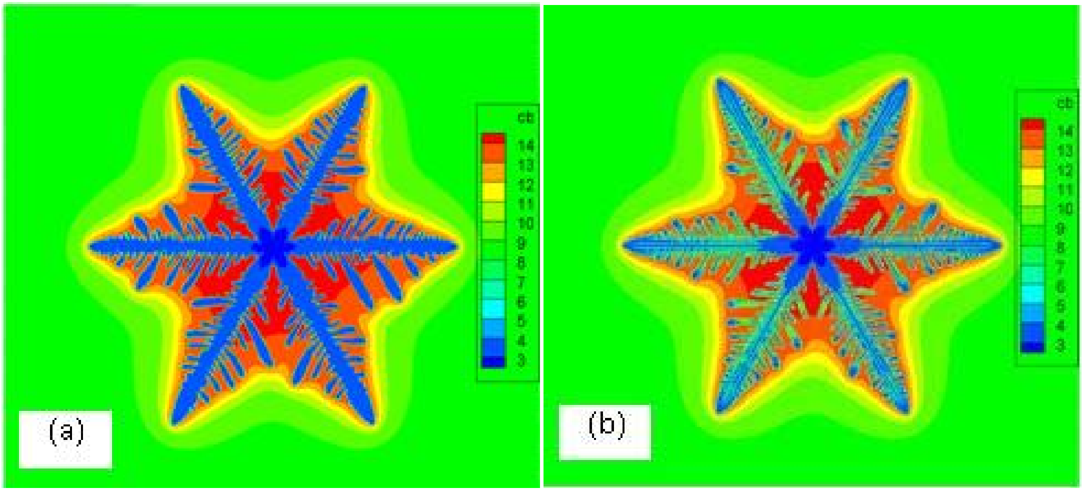

Figure 5.10 Solute map with Gibbs-Thomson coefficient of (a) 4.0×10^{-7}K•m and (b) 0.5×10^{-7}K•m

The influence of the anisotropy coefficient on the dendritic growth is also studied by the model. The calculation results are shown in Figure 5.11(a), (b), and (c) with anisotropy coefficients of 2.1, 1.6, and 0.6, respectively, at the same simulation time of 0.2968s. Small anisotropy coefficients lead to large dendritic trunks, while large anisotropy coefficients result in thin arms, which aid in the formation of secondary and tertiary arms. High anisotropy coefficients promote grain growth with the characteristic hexagonal shape and assist in the formation of the secondary and tertiary arms.

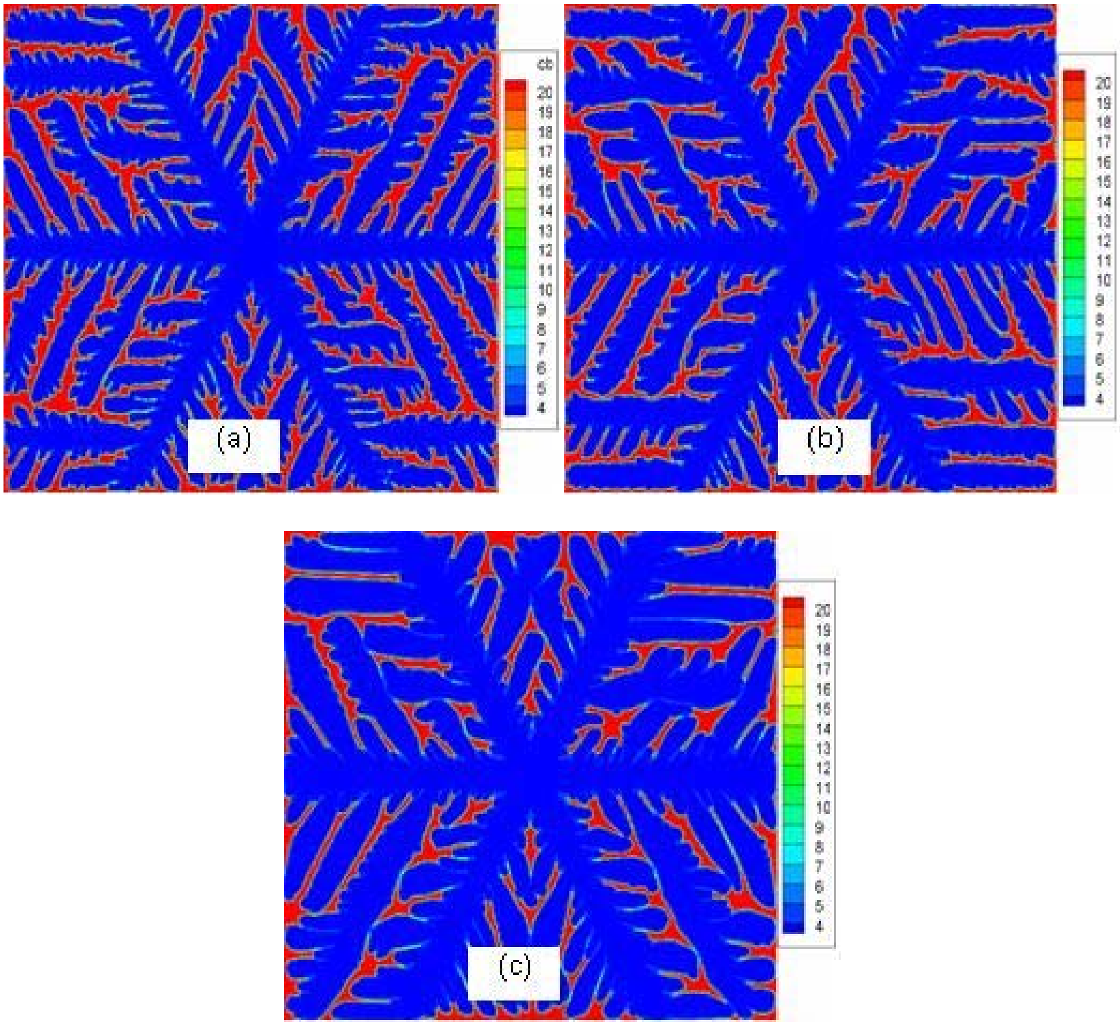

Figure 5.11 Solute map with anisotropy coefficient of (a) 2.1, (b) 1.6, and (c) 0.6

Columnar dendrite growth was also simulated with the AZ91 alloy directionally solidified under constant heat flux applied on the left boundary. The calculation domain has a 400×200 mesh with an element size of 0.25µm. At the beginning of the simulation, two nuclei are placed at the left wall with the same crystallographic orientation aligned with the temperature gradient. Figure 5.12(a) and (b) show the simulated columnar dendrites under a heat flux of 80kW/m^2 and 20kW/m^2, respectively, at corresponding simulation times of 0.0339s and 0.1166s. The primary arms whose morphology orientations are not parallel to the heat transfer direction are stopped by the growth of the arm which is parallel to the heat transfer direction. The growth of some main arms is suppressed by nearby dendrites. High liquid composition between the two columnar grains makes the secondary arms comparatively short due to the small separation between them. The simulation results agree qualitatively well with the measured columnar microstructure of the AZ31 alloy reported in Ref. [190].

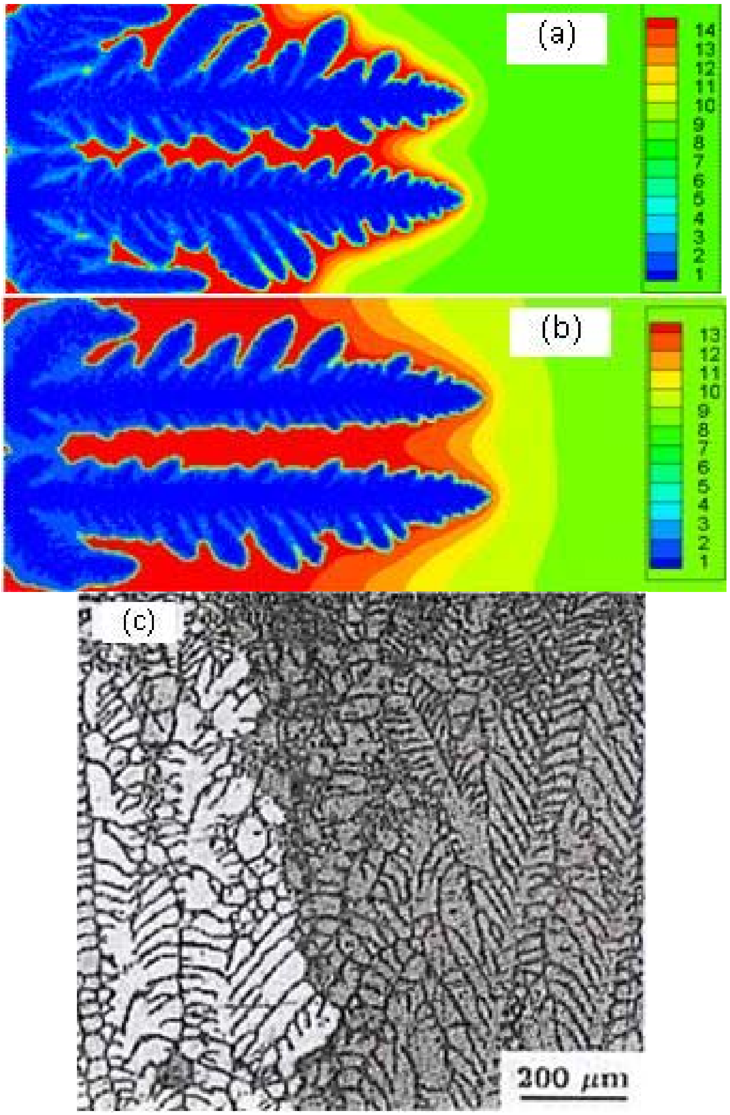

Figure 5.12 Solute maps with (a) heat flux of 80kW/m2 and simulation time 0.0339s, (b) heat flux of 20kW/m2 and simulation time 0.1166s, and (c) experiment morphology [190]

5.6 Discussion

5.6.1 Influence of mesh size on the grain morphology

The mesh size may have a significant effect on the simulated microstructure. Stefanescu [136] and Zhu [137] discussed the influence of mesh size on the convergence of tip velocity, but they reached different conclusions. Stefanescu conducted simulations for a Fe-0.6wt%C alloy with varying mesh size to demonstrate its influence. His calculations indicated that the tip velocity tends to stabilize at about 58µm/s when the mesh size is approximately less than 0.3µm, which implies convergence of the model. However, the model developed by Zhu converges when the mesh size is less than 1µm at which the stable velocity of the tip is 117µm/s for Al-4wt%Cu. For the present model, the influence of mesh size on the morphology is shown in Figure 5.7. The microstructure shown in Figure 5.7(a) gradually converges to the one shown in Figure 5.7(c) for a mesh size of 0.33µm, which is closer to the value obtained by Stefanescu.

5.6.2 Influence of undercooling on the grain morphology

Zhu and Stefanescu [137] compared the dendritic morphologies for Al dendrites grown at different undercoolings, finding that the dendrite arms at smaller undercooling were thicker than those for the larger undercooling. In the present model, similar results are obtained, as Figure 5.9 shows, but it is not as obvious as found in Ref. [137]. This is due to the fact that in our simulation the temperature continuously decreases with constant heat extraction, and therefore the undercooling keeps changing. But, in the simulation of Ref. [137], the heat extraction rate was changed according to the amount of latent heat rejected during dendritic growth in order to keep the heat balance, thus obtaining a constant undercooling of the melt in the domain.

5.6.3 Influence of diagonal size d on the grain morphology

In this model, it is evident that the diagonal size of the cell determines when the neighboring cells are captured and become interface cells, which influences the growth velocity. It is indicated from Eq.5.8 that the diagonal size can be large even for a small solid fraction if the diagonal length coefficient k_d is large enough. By comparing Figure 5.13(a) and (b), the primary arm is longer for larger k_d values. As the diagonal size increases, the neighboring cells can be captured sooner, and more cells are changed to interface cells. This results in the release of more latent heat, which causes remelting and lower solute concentration as observed in Figure 5.13(a).

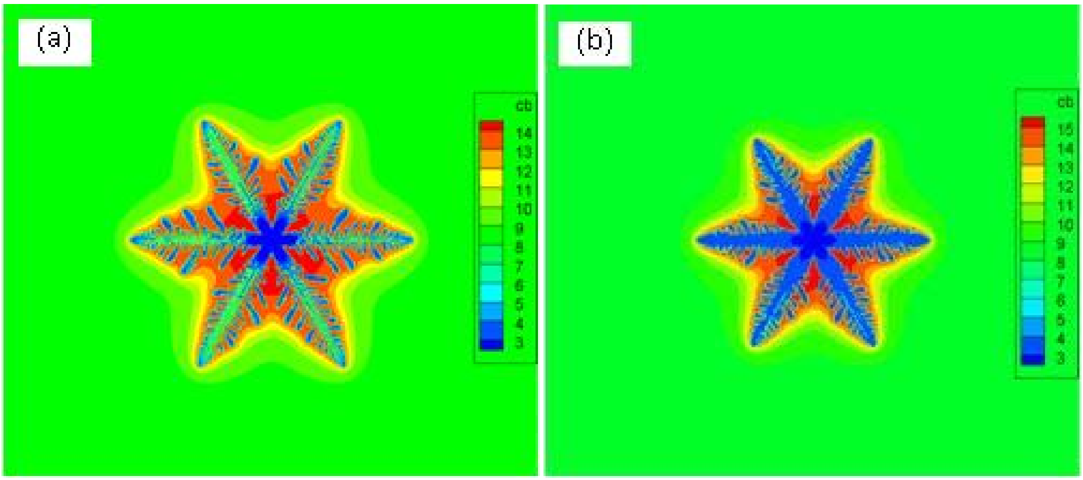

Figure 5.13 Solute maps obtained with diagonal length coefficient of (a) 0.962 and (b) 0.912

5.7 Conclusions

A 2D model coupling the CA and FE methods was developed to simulate solute controlled dendrite growth in hexagonal crystal metals. The model simulations compared reasonably well with previously published experimental and computational results of dendrite growth in hexagonal structure materials, including reported trends with cooling rate. A study of the effect of model parameters showed different degrees of sensitivity to mesh size, surface tension, undercooling, and anisotropy. By using a honeycomb-like FE mesh and hexagonal CA cells, the model was able to predict the six-fold symmetry of dendritic growth in magnesium alloy AZ91 (approximated with the binary Mg-8.9wt%Al). To the my knowledge, this is the first report of a FE-CA coupled model capable of simulating the free growth of a perfect six-fold dendrite starting from a solid seed, both in equiaxial and columnar structures. Although this is an encouraging result, the model still needs further testing and developing, particularly in handling the interaction of multiple six-fold dendrites growing in arbitrary orientations and a more comprehensive study of the convergence properties for different mesh size and growth rates.

The work of this chapter was published in the Modelling Simulation of Materials Science and Engineering in 2009 [191] and was also pre-viewed and presented in the conference TMS 2009 [192].

CHAPTER VI

SOLIDIFICATION MODEL WITH COUPLED LATTICE BOLTZMANN AND CELLULAR AUTOMATON METHOD

6.1 Introduction

The traditional computational fluid dynamics (CFD) methods solve the conservation equations of macroscopic properties numerically, such as mass, momentum, and energy, using a FD method, FV method, or FE method as the previous chapters discussed. All those solvers are continuum-based approaches, and it is difficult to handle the discontinuity of flow velocity at the moving SL interface. Moreover, the fluid flow simulation is difficult to converge as the dendrite morphology becomes complicated with increasing solid fraction. However, in lattice Boltzmann (LB) method models, the fluid is treated as consisting of fictive particles, which perform consecutive propagation/ streaming and collision/relaxation processes over a discrete lattice mesh. For 2D model with quadrangle mesh, each lattice node is connected to its neighbors by 9 lattice velocities. Through a Chapman-Enskog analysis, one can recover the governing continuity and Navier-Stokes equations from the LB algorithm. In addition, the pressure field is also directly available from the density distributions and hence, there is no extra Poisson equation to be solved as in traditional CFD methods [193-195].

Over the last two decades, the LB method has rapidly emerged as a comparatively powerful technique with great potential for numerically solving momentum [196-202], energy and/or composition equations [203-207]. Miller [208, 209] built LB-PF models to simulate the flows of binary-alloys with liquid-solid phase-transition. Cellular growth was simulated with shear flow but without giving much details of the growth process and without considering the temperature field. A 2D LB-CA model was also built to simulate the dendrite growth [210]. In the model, the LB method was adopted to simulate the solute distribution and fluid flow. CA technique was used to predict the dendrite growth, but the model did not consider the calculation of temperature field. The present 2D model, which coupled the LB and CA methods, is built to simulate the temperature field, solute concentration, fluid flow, and dendrite growth.

6.2 Model description

6.2.1 D2Q9 model

For fluid flow instance, a 2D incompressible fluid flow with density ρ and kinematic viscosity ν is considered in a rectangular domain. The calculation domain is divided into a regular arrange of lattice as shown in Figure 6.1(a) [193]. The fluid is represented as a group of fluid particles residing at lattice nodes that move to its eight immediate neighboring nodes along eight different directions with given eight different discrete velocities at e_a, $(a = 0, \dots 8)$ discrete times as shown Figure 6.1(b).

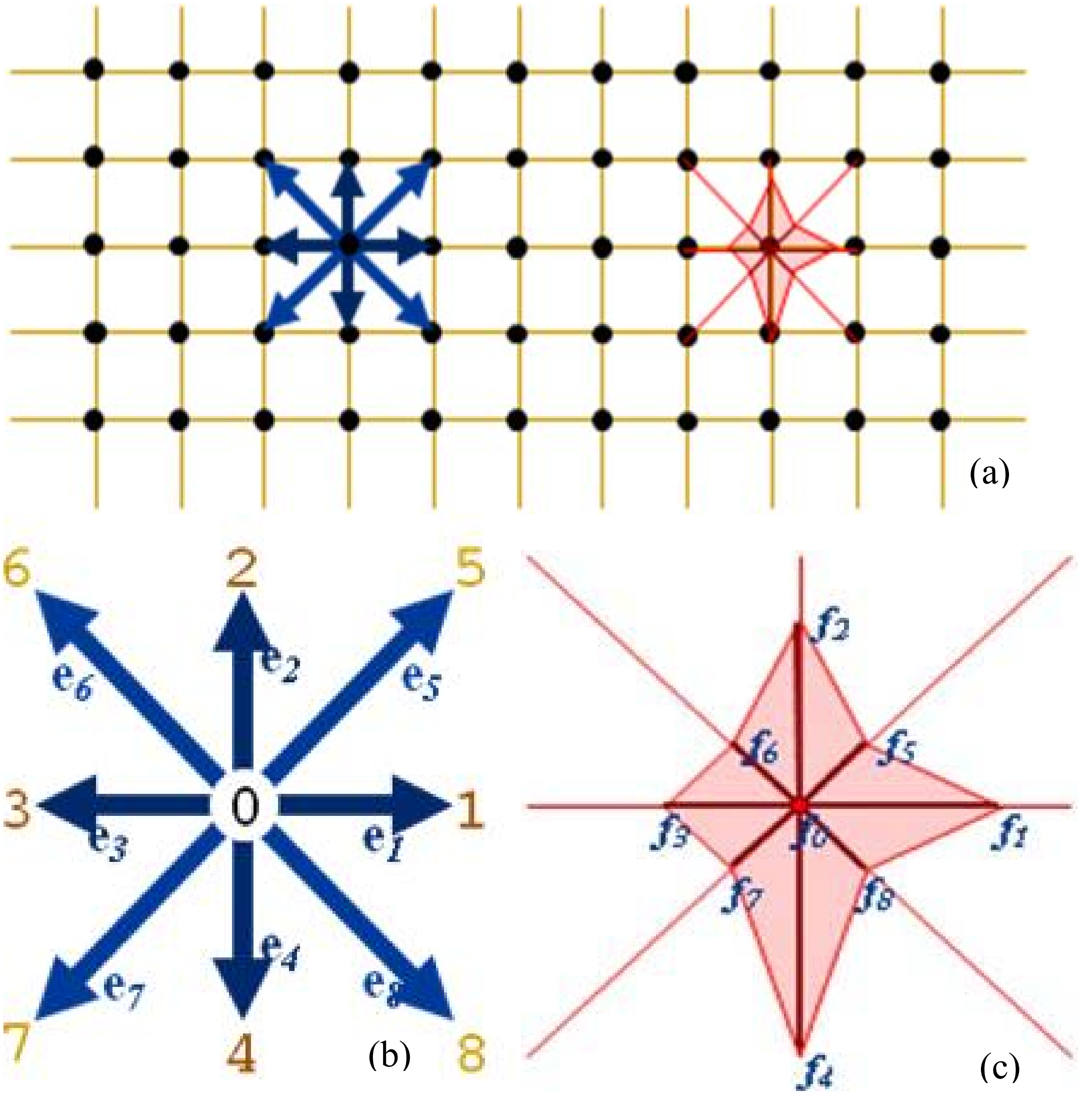

Figure 6.1 (a) D2Q9 model for LB method with quadrangle lattice having 9 discrete (b) velocities and (c) density functions

The primary variables in the LB formulation are the so-called fluid density distribution function (Figure 6.1(c)), each relating to the probable number of fluid particles moving with velocity e_a, along the a^{th} direction at each node. Following the single relaxation time BGK (Bhatnagar-Gross-Krook) formulation, the evolution of density distribution functions at each time step is given by [211,212]:

$$f_a(X+e_a\Delta t,t+1)=f_a(X,t)-\frac{f_a(X,t)-f_a^{eq}(X,t)}{\tau_v} \qquad \text{(Eq.6.1)}$$

Where $X+e_a\Delta t$ is the nearest node of X along the direction a, and τ_v is the relaxation time ($\tau_v=3\nu+0.5$), and f_a^{eq} is the equilibrium distribution functions.

$$f_a^{eq}(X)=w_a\rho(X)\left[1+3\frac{e_a\cdot u}{c^2}+\frac{9}{2}\frac{(e_a\cdot u)^2}{c^4}-\frac{3}{2}\frac{u^2}{c^2}\right] \qquad \text{(Eq.6.2)}$$

$$e_a=\begin{cases}(0,0) & a=0\\ (\cos[(a-1)\pi/2],\sin[(a-1)\pi/2])c & a=1-4\\ (\cos[(a-1)\pi/2],\sin[(a-1)\pi/2])c & a=5-8\end{cases} \qquad \text{(Eq.6.3)}$$

Two steps are needed for the computation with LB method: collision $f_a(X+e_a\Delta t,t+1)=f_a(X,t)$ and streaming $f_a(X,t)-f_a^{eq}(X,t)/\tau_v$. The collision operation computes the right hand side of Eq.6.1 that only involves the variables associated with each node X, and it is a local operation. The streaming step is to explicitly propagate the direction-specific distribution functions (the updated f_a after collision) to its nearest neighbor lattice nodes, where clearly no computations are required and only data exchange between neighboring nodes is necessary.

The macroscopic fluid variables, density ρ and velocity u, can be obtained from the moments of distribution function f_a as below:

$$\rho=\sum_{a=0}^{8} f_a \qquad \text{(Eq.6.4)}$$

$$u=\frac{1}{\rho}\sum_{a=0}^{8} f_a e_a \qquad \text{(Eq.6.5)}$$

6.2.2 Boundary conditions

Bounce back boundary would be applied at the slit wall [193, 196]. This kind of boundary is particularly simple and has played a major role in making LB method popular in simulating fluids in domains characterized by complex geometries such as those found in porous media. It only needs to designate a particular node as a solid obstacle and no special programming treatment is required, and the bounce back process is shown in Figure 6.2.

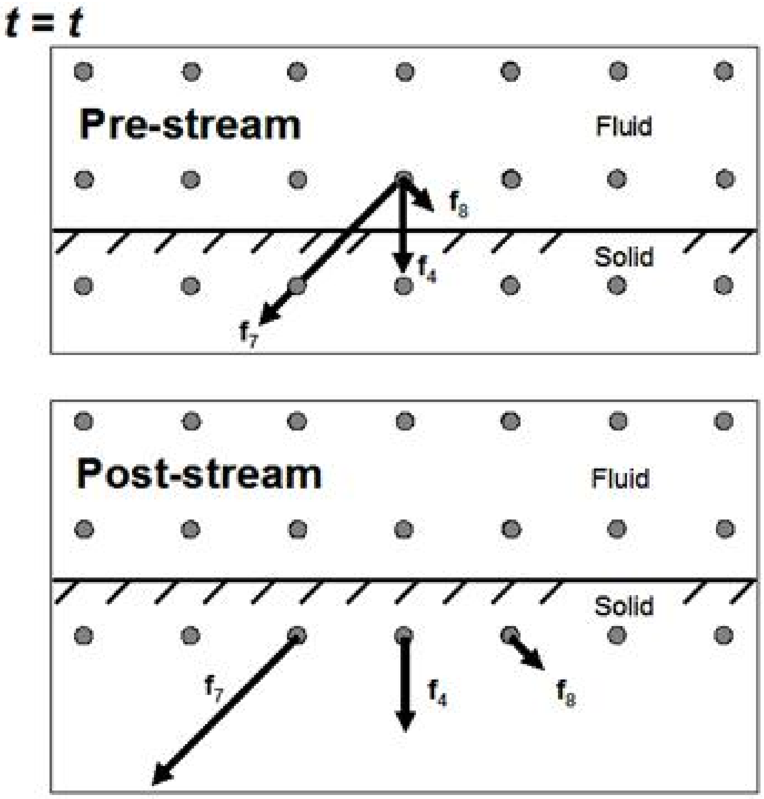

Figure 6.2 Illustration of mid-plane bounce-back movement of direction specific densities [193]

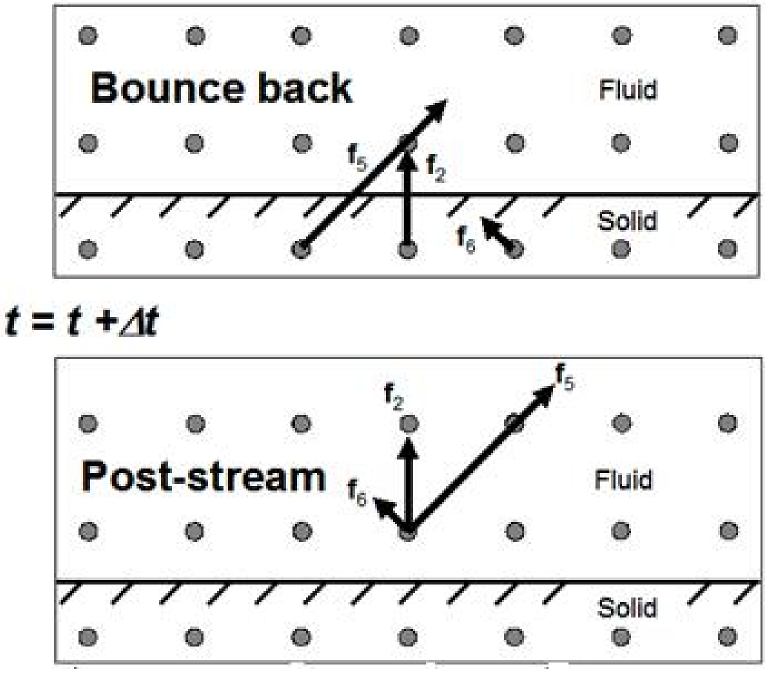

Figure 6.2 (Continued)

Von Neumann boundary conditions constrain the flux at the boundaries. For example at the north side of the calculation as shown in Figure 6.3, and the velocity vector consists of zero x-component, and y-component is v_0,

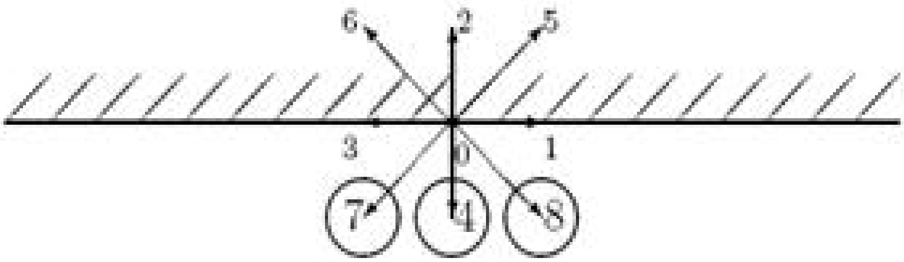

Figure 6.3 Direction-specific density are unknown after streaming at a north boundary

The contributions from f_a for $a = 0,1,2,3,5,6$ are already known because they arrive from other nodes inside the domain. Four variables, including ρ, f_4, f_7, and f_8 are needed to be solved, which means four equations are needed.

The macroscopic density formula is the one equation:

$$\rho = f_0 + f_1 + f_2 + f_3 + f_4 + f_5 + f_6 + f_7 + f_8 \qquad \text{(Eq.6.6)}$$

The macroscopic velocity in x- and y- directions:

$$0 = f_1 - f_3 + f_5 - f_6 - f_7 + f_8 \qquad \text{(Eq.6.7)}$$

$$\rho v_0 = f_2 - f_4 + f_5 + f_6 - f_7 - f_8 \qquad \text{(Eq.6.8)}$$

A fourth equation can be written by assuming that the bounce back condition holds in the direction normal to the boundary.

$$f_2 - f_2^{eq} = f_4 - f_4^{eq} \qquad \text{(Eq.6.9)}$$

However, based on the equilibrium distribution function:

$$f_4 = f_2 - f_2^{eq} + f_4^{eq} = f_2 - \frac{2}{3}\rho v_0 \qquad \text{(Eq.6.10)}$$

Solve the Eq.6.5-6.7 together with the Eq.6.9, and the other three variables can be obtained as below:

$$\rho = \frac{f_0 + f_1 + f_3 + 2(f_2 + f_5 + f_6)}{1 + v_0} \qquad \text{(Eq.6.11)}$$

$$f_7 = f_5 + \frac{1}{2}(f_1 - f_3) - \frac{1}{6}\rho v_0 \qquad \text{(Eq.6.12)}$$

$$f_8 = f_6 - \frac{1}{2}(f_1 - f_3) - \frac{1}{6}\rho v_0 \qquad \text{(Eq.6.13)}$$

6.2.3 Thermal and concentration calculation

The thermal energy distribution solves the following kinetic equations for the distribution function $f_{T,a}$ [211, 212]:

$$f_{T,a}(X + e_a \Delta t, t+1) = f_{T,a}(X,t) - \frac{f_{T,a}(X,t) - f_{T,a}^{eq}(X,t)}{\tau_\alpha} \qquad \text{(Eq.6.14)}$$

Where $\tau_\alpha = 3\alpha + 0.5$, α is thermal diffusivity. The macroscopic energy is defined as $e = \sum_a T_a/\rho$, and similarly the equilibrium distribution functions for the thermal energy distribution $f_{T,a}^{eq}$ can be written as:

$$\begin{cases} f_{T,0}^{eq} = -\frac{2\rho e}{3}\frac{u^2}{c^2} & \\ f_{T,a}^{eq} = \frac{\rho e}{9}\left[\frac{3}{2} + \frac{3}{2}\frac{e_a \cdot u}{c^2} + \frac{9}{2}\frac{(e_a \cdot u)^2}{c^4} - \frac{3}{2}\frac{u^2}{c^2}\right] & (a = 1,2,3,4) \\ f_{T,a}^{eq} = \frac{\rho e}{36}\left[3 + \frac{6 e_a \cdot u}{c^2} + \frac{9}{2}\frac{(e_a \cdot u)^2}{c^4} - \frac{3}{2}\frac{u^2}{c^2}\right] & (a = 5,6,7,8) \end{cases} \qquad \text{(Eq.6.15)}$$

The solute transport solves the following equation for the distribution g_a [193]:

$$g_a(X + e_a \Delta t, t+1) = g_a(X,t) - \frac{g_a(X,t) - g_a^{eq}(X,t)}{\tau_c} \qquad \text{(Eq.6.16)}$$

Where $\tau_c = 3D_l + 0.5$, D_l is the solute diffusivity. The concentration is $c_\sigma = \sum_a g_a$, and so the equilibrium distribution is given by [193]:

$$g_a^{eq} = w_a c_\sigma (1 + 3e_a \cdot u) \qquad \text{(Eq.6.17)}$$

Constant concentration boundary $\bar{c}_\sigma$ is imposed to solve the solute transport [193]. For example at the north side boundary (Figure 6.3), assume the unknown directional densities g_a for a in $\{4, 7, 8\}$ are of the form $g_a = w_a g'_\sigma$, which denotes the residual amount of concentration needed to satisfy the specified concentration condition $\bar{c}_\sigma$.

$$\begin{aligned} \bar{c}_\sigma &= \textstyle\sum_a g_a \\ &= g_0 + g_1 + g_2 + g_3 + g_5 + g_6 + g'_\sigma(w_4 + w_7 + w_8) \end{aligned} \qquad \text{(Eq.6.18)}$$

So the residual concentration can be computed as below:

$$g'_\sigma = \frac{\bar{C}_\sigma - (g_0+g_1+g_2+g_3+g_5+g_6)}{w_4+w_7+w_8} \qquad \text{(Eq.6.19)}$$

The unknown directional densities are:

$$g_4 = w_4 g'_\sigma = \frac{1}{9} g'_\sigma \qquad \text{(Eq.6.20)}$$

$$g_7 = w_7 g'_\sigma = \frac{1}{36} g'_\sigma \qquad \text{(Eq.6.21)}$$

$$g_8 = w_8 g'_\sigma = \frac{1}{36} g'_\sigma \qquad \text{(Eq.6.22)}$$

Other boundaries for temperature and concentration calculations can refer to the published articles [213-215].

6.3 Calculation results with 2D model

Evaluation of this model for heat and mass transfer and fluid flow has been done by comparing to analytical solution and/or published results.

6.3.1 Heat and mass evaluation of LB method

A 2D model was built with constant higher temperature and composition at left side and with lower ones at the right to simulate the heat and mass transfer from the left side to the right side. The calculation domain is 0.002×0.001m with mesh of 200 × 100 as Figure 6.4 shows. The simulation material has solute diffusivity:D_l = 5.0×10^{-9}m^2/s and thermal diffusivity:α = 1/12×10^{-4}m^2/s. The two equations below are the analytical solutions for temperature and solute concentration at a certain time and location as below:

$$c = c_0 + (c_H - c_0) \times (1 - \mathrm{erf}(\frac{x}{2\sqrt{D_l t}})) \qquad \text{(Eq.6.23)}$$

$$T = T_0 + (T_H - T_0) \times (1 - \mathrm{erf}(\frac{x}{2\sqrt{\alpha t}})) \qquad \text{(Eq.6.24)}$$

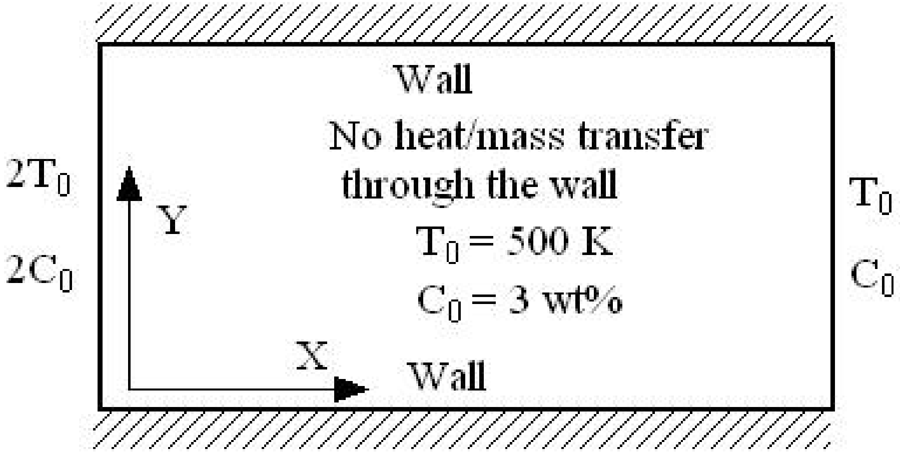

Figure 6.4 Schematic of two dimensional model for heat/mass transfer

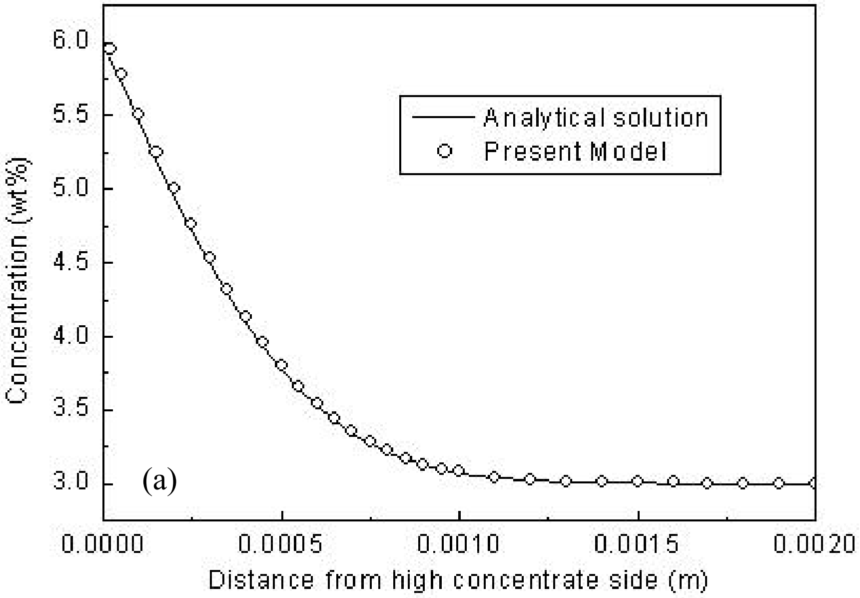

Figure 6.5 (a) Composition profile along x-direction at time of 19.355s, and (b) temperature profile along x-direction at time of 3.871×10^{-2}s

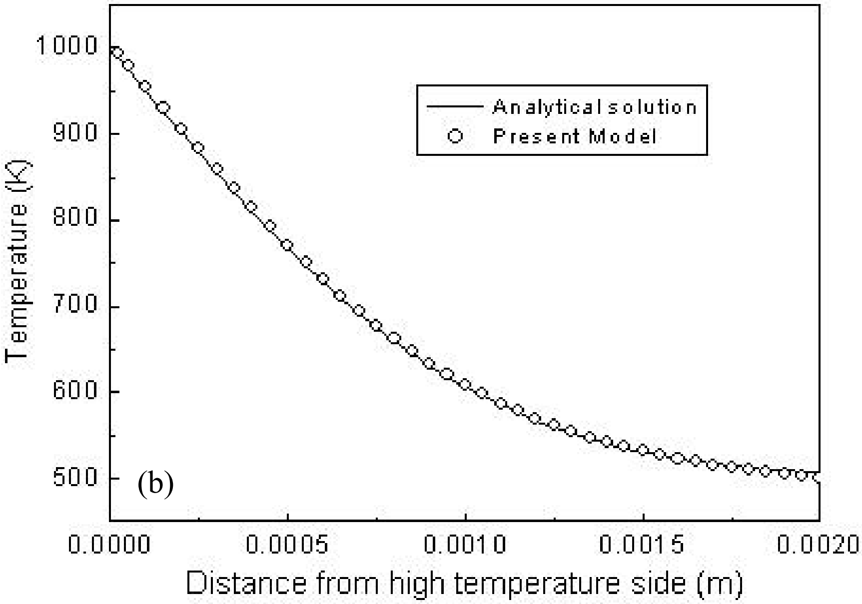

Figure 6.5 (Continued)

The Figure 6.5 shows good agreements between the simulation results of concentration and temperature profiles by present model and those from the analytical solutions, which give the evaluation of the model with LB method for heat and mass transfer.

6.3.2 Lid-driven flow evaluation of LB method

A lid-driven cavity flow is built to test the flow problem with LB method. The objective of this model is to implement and evaluate the LB method by comparing the results of an upper, lid-driven cavity flow with previous published results. The calculation domain is 0.02×0.02m with the mesh of 200×200 as Figure 6.6 shows. The simulation materials have the viscosity of 0.006Pa·s and density of 6000Kg/m^3, and velocity U_0 is applied at the surface. Different lid moving velocities resulting in different Reynolds numbers are adopted to examine the flow pattern in the cavity.

Bounce back boundary conditions are applied to the three stationary walls as Figure 6.2 shows. The Von Neumann boundary is imposed to the top wall of the cavity. The equilibrium distribution function at the upper moving plate is computed by substituting the uniform plate velocity into the Eq.6.2. After the streaming, the velocity at the top plate is reinforced to be the uniform plate velocity and then the equilibrium distribution function is reevaluated using the fixed plate velocity and the updated density at the plate. The upper two corner lattice points are considered as the part of the moving plate.

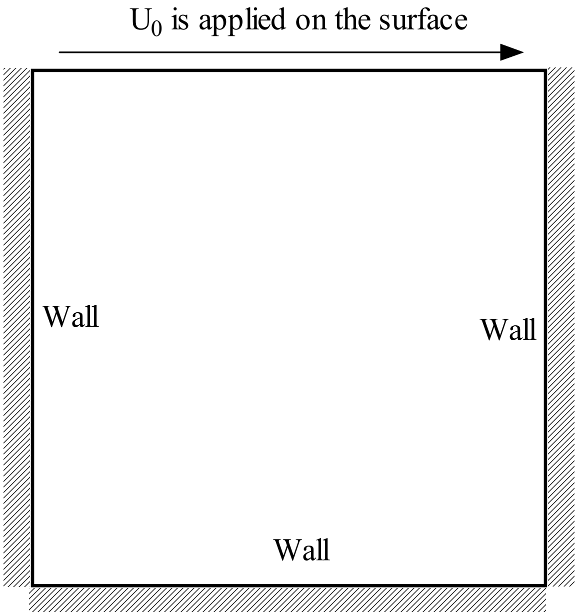

Figure 6.6 Schematic of lid-driven model with constant velocity U_0 at upper side

The uniform top velocity is $U_0 = 0.005$ and 0.05m/s considering the validity of using LB method in simulating near-incompressible flows, and the Reynolds numbers are 100 and 1000 respectively. Figure 6.7 shows the simulated streamline for Reynolds numbers of 100 and 1000. There is a major vortex in the center, which circulates in clockwise direction as expected because the upper plate moves into the right-hand direction. In addition to the one major vortex, there appear two minor vortices circulating counterclockwise in the two lower cavity corners. Besides, the sizes of the minor vortices increase with increasing Reynolds numbers – here, from 100 to 1000. By comparison of the simulation results for different Reynolds numbers, generally speaking, the overall flow structures (streamlines) predicted by the models are very similar to those predicted by Wu and Shao [216].

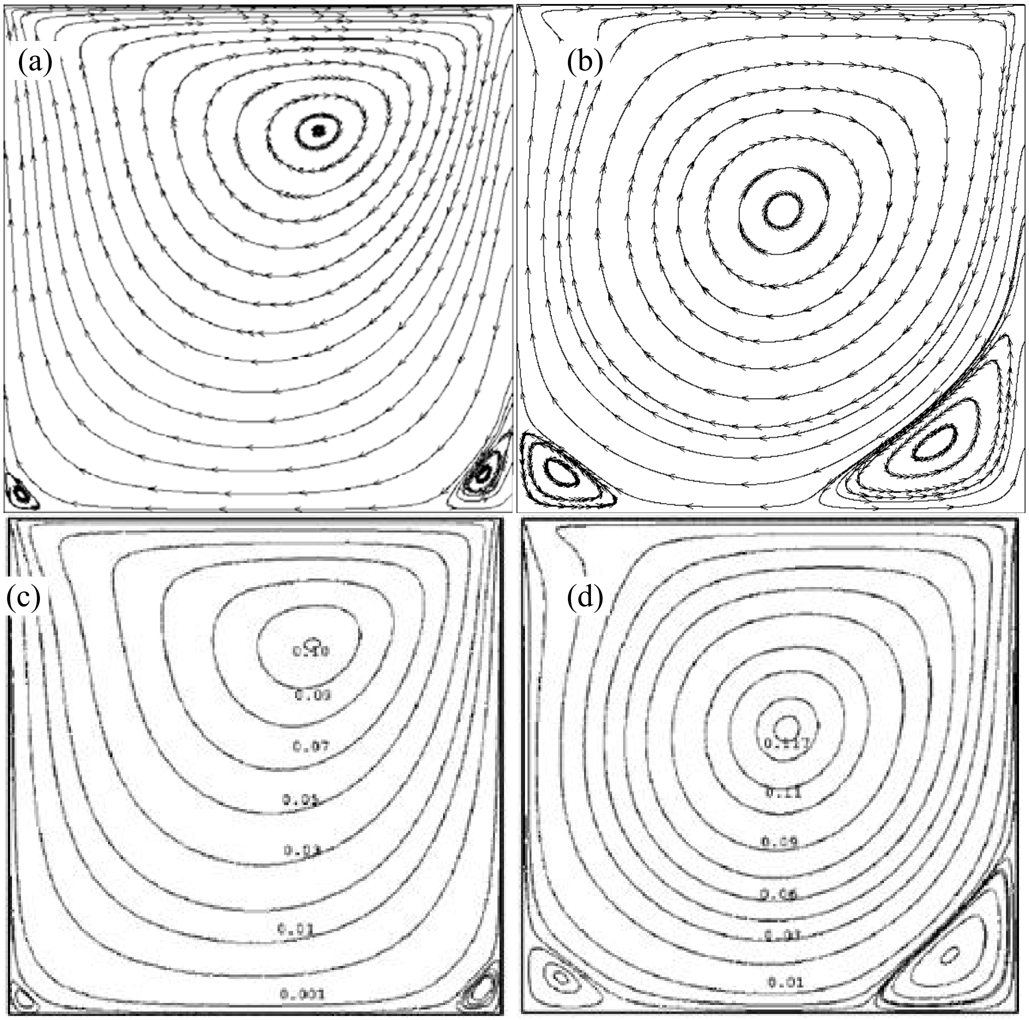

Figure 6.7 The calculation streamlines by present model for (a) U_0 = 0.005m/s or Re=100 and for (b) U_0 = 0.05m/s or Re = 1000; (c) and (d) are the published results with LB method for Reynolds numbers of 100 and 1000, respectively [216].

6.4 Solidification model with LB method and CA technique

A 2D LB-CA model is built to simulate the dendrite growth in convection. The model adopts the LB method to describe the transport phenomena and fluid flow, such as the energy and solute, and CA is adopted to simulate the dendrite growth process. The simulation material is binary alloy Al-3.0wt% Cu, and the main thermal properties used in the simulation are listed in Table A.4 in Appendix A. Figure 6.8 illustrates the physical system under consideration with domain of 90×90μm and with mesh number of 300×300. The forced flow is generated by imposing a uniform inlet flow velocity indicated as U_0 at the left side of the domain. This model also can calculate the temperature field by imposing the temperature gradient at the boundary sides to examine the influence of cooling rate on the dendrite growth.

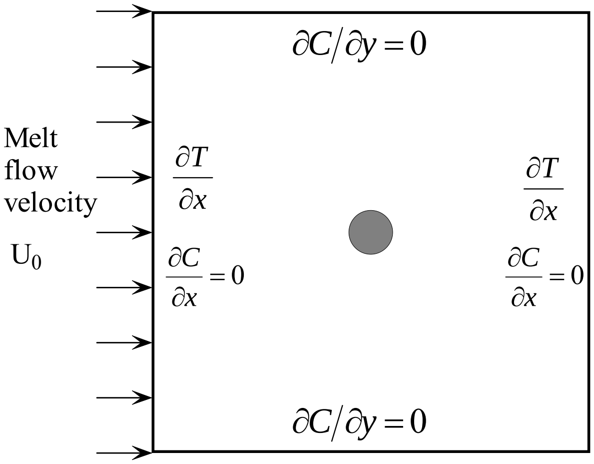

Figure 6.8 Illustration of the physical system and boundary conditions for solidification modeling

Initially, one nucleus is placed at the center of the domain, and the temperature field inside the domain is considered to be uniform with a constant undercooling and without the inflow velocity at left side. These two pictures evaluate the model quantitatively by comparing the numerical simulations with the LGK predictions for the steady-state tip parameters as function of the melt undercooling. Figure 6.9(a) shows the comparison of tip velocity against uncercooling calculated by current model with LGK analytical solution. And Figure 6.9(b) shows the comparison of equilibrium liquid composition at the tip against undercooling by current model with LGK analytical solution. As the Figure 6.9 shows, both the steady-state tip velocity and the equilibrium composition increase with increasing undercooling. The predicted tip velocity by the present model is a little higher, but the composition is slightly lower than the LGK analytical solutions [189]. However, the numerical simulation results are all close to the theoretical solutions.

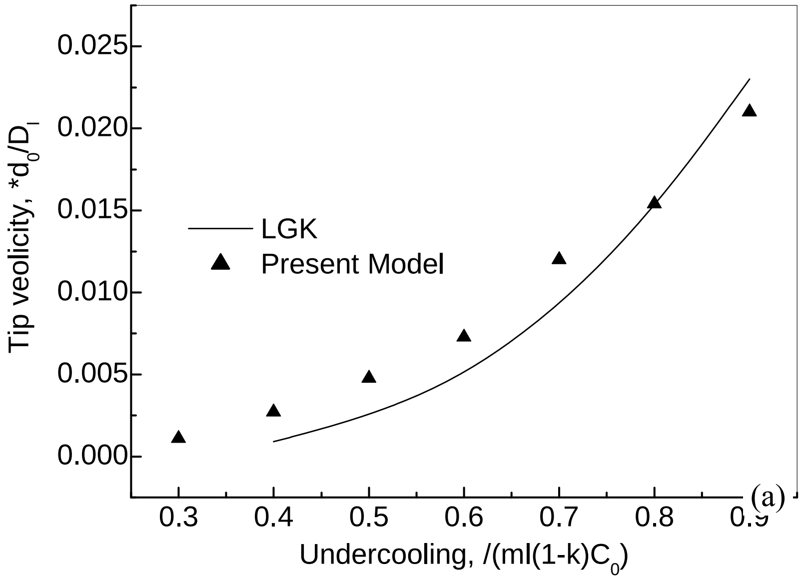

Figure 6.9 Comparisons of the present model to LGK analytical solutions for (a) tip velocities with various under cooling and (b) equilibrium liquid composition at tip against the under cooling

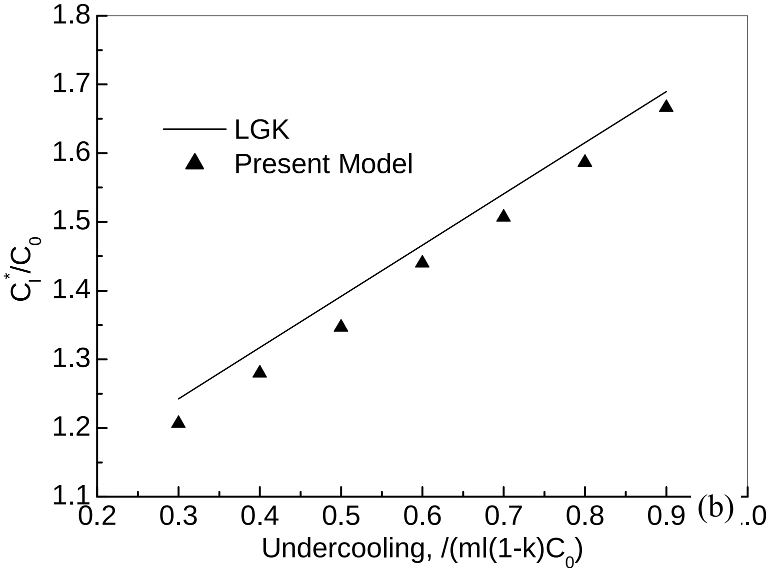

Figure 6.9 (Continued)

To simulate the free dendrite growth in a forced flow and to investigate the influence of convection on the dendrite growth, an inlet flow with constant velocity could be imposed on the left boundary of the domain, but with constant undercooling. The dendrite morphology with different preferential orientations, 30 and 60 degrees, were also calculated, both of them follow the crystallographic orientations as Figure 6.10 shows. Figure 6.10(b) and (d) show the dendrite morphologies considering the influence of convection. By comparing the dendrite morphologies with and without fluid flow from Figure 6.10, it is apparent that the dendrite shape is significantly influenced by the fluid flow for such calculation conditions. The growth of the dendrite enhances on the upstream side and decreases on the downstream side. When the dendrite grows in the presence of convection, the solute rejected at the SL interface is washed away from the upstream to the downstream direction by the flowing melt, resulting in an asymmetrical solute profile in liquid, i.e. the concentration in the upstream region is lower than that in the downstream. The decreased local actual solute concentration at the interface results in a higher increment in solid fraction and thereby a higher tip velocity.

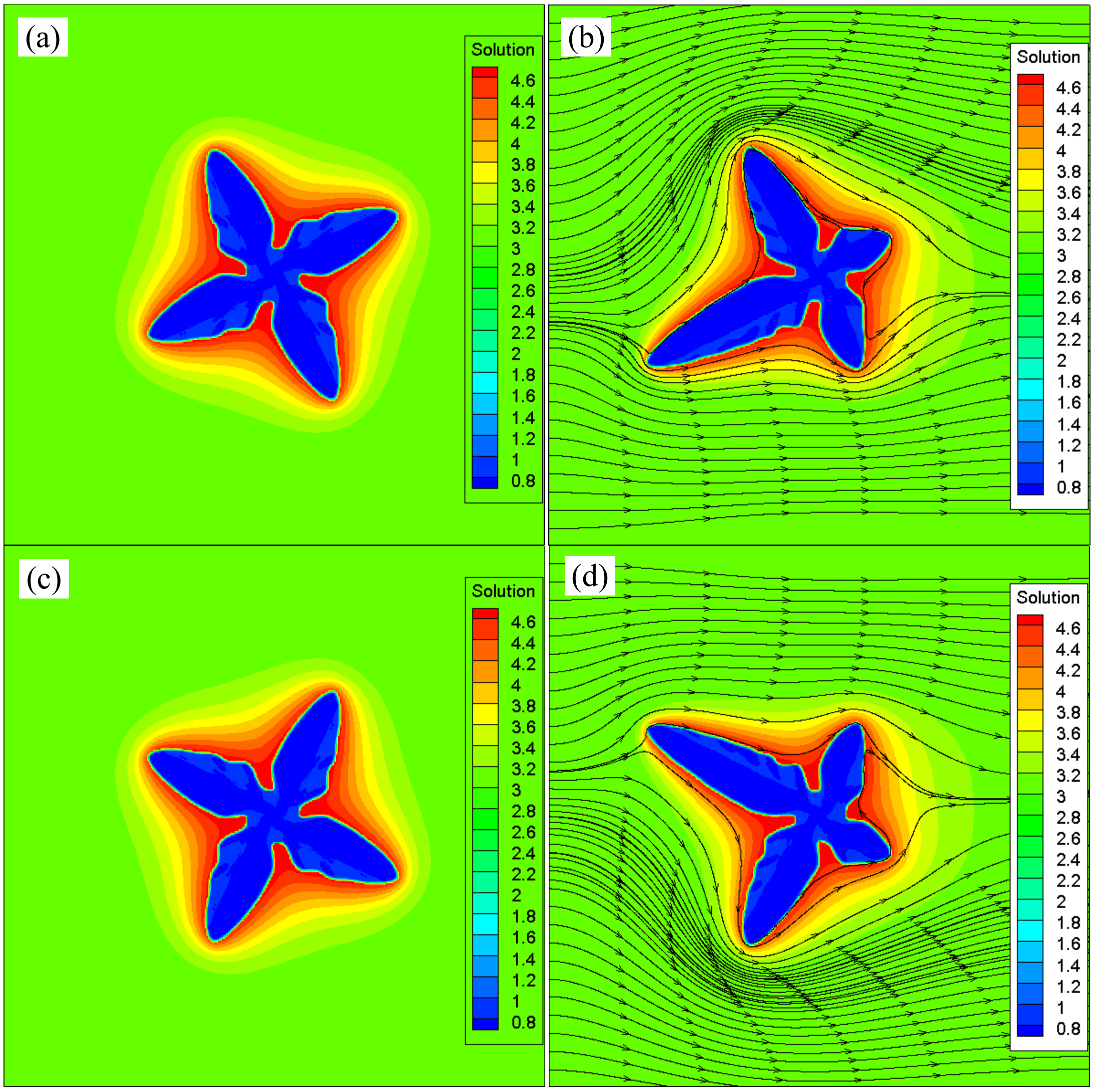

Figure 6.10 Single dendrite morphology with preferential directions of 30 ((a) and (b)) and 60 ((c) and (d)) for free dendrite growth ((a) and (c)) and for dendrite growth in convection ((b) and (d))

Figure 6.11(a) shows the dendrite morphology with preferential direction of 0 degrees at constant under cooling and without the convection. Four-fold symmetrical shape is obtained with the primary dendrite arms. Figure 6.11(b) shows the dendrite morphology in convection imposed at the left side with the same other simulation parameter as adopted in Figure 6.11(a) shown. It is clearly shown that convection enhances the dendrite growth. To study the influence of cooling rate on the dendrite growth, constant temperature gradient is imposed on the boundaries to obtain the non-uniform temperature field with cooling rate in the domain. By comparing the Figure 6.11(a) and (c), it is obvious that secondary arms form from the primary dendrite arm if there exists a cooling rate in the calculation domain, that means the cooling rate enhances the branching of dendrite arms. When increasing the anisotropy degree coefficient from 0.4 (simulation results shown in Figure 6.11(c)) to 0.8(simulation results shown in Figure 6.11(d)), SDAS is more obvious by comparing the Figure 6.11(c) and (d).

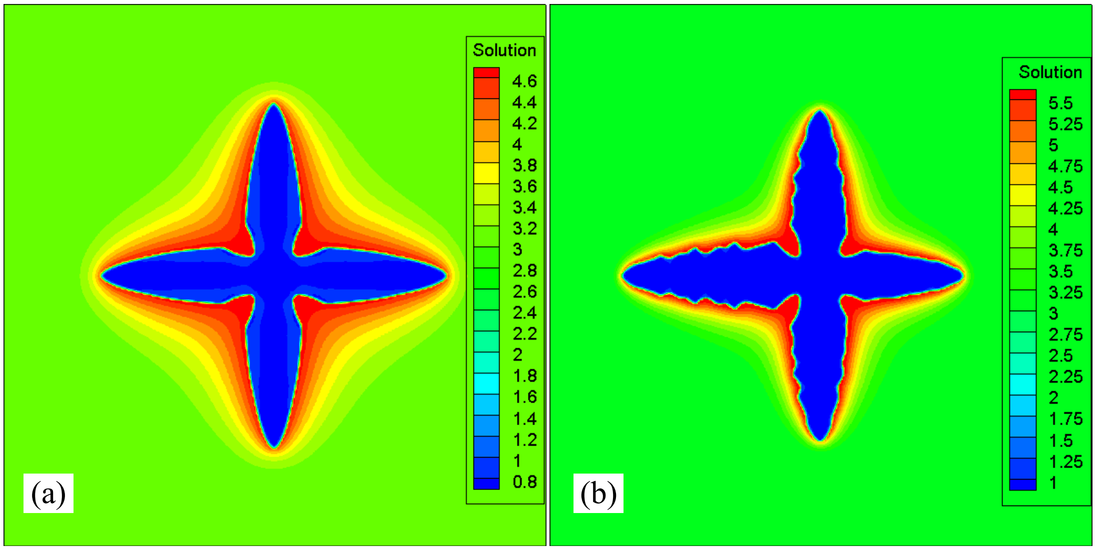

Figure 6.11 Single dendrite morphology with 0 preferential direction (a) at constant undercooling and (b) at constant inflow at left wall and (c) at constant temperature gradient at the boundaries and (d) with a higher anisotropy coefficient

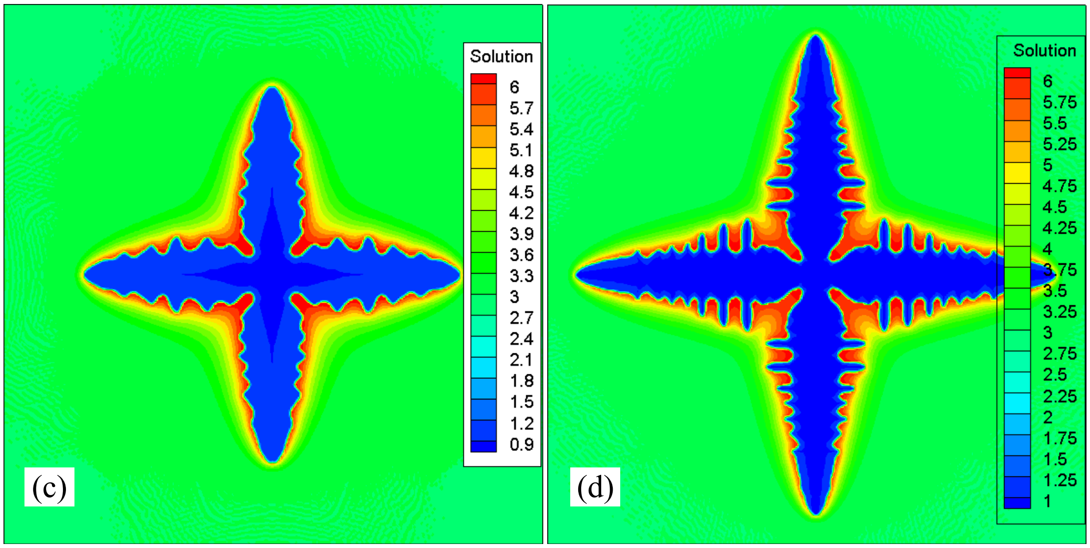

Figure 6.11 (Continued)

6.5 Conclusions

A 2D model, which coupled the LB method and CA technique, was developed to simulate dendrite growth during the solidification. LB method was adopted to simulate the temperature field, solute concentration, and fluid flow, while the CA was used to simulate the dendrite growth. The model of the energy and solute calculations was evaluated by comparing the present simulation results of temperature and composition profiles to analytical solutions. The lid-driven fluid flow was also calculated and compared to the published simulation. In addition, the dendrite growth simulation was carried out and evaluated by comparing the tip velocity and the equilibrium liquid solute to the analytical solutions. Besides, the influence of cooling rate, stream velocity, and anisotropy coefficient on the dendrite growth was also discussed.

CHAPTER VII

SUMMARY AND FUTURE WORK

7.1 Summary

A multi-scale model was developed to simulate the dendritic structure during solidification of a Fe-C binary alloy in the molten pool of the LENS laser deposition process. The model could calculate temperature distribution and thermal history for LENS process with multi-layer deposition by solving the energy equation with the FE method. The fluid flow in the molten pool during LENS process was also predicted with FE method by solving momentum and concentration conservation equations. The influences on the heat transfer and fluid flow of surface tension induced Marangoni convection were also discussed. The solidification dendrite structure in the molten pool was also predicted based on the CA technique and the simulation results on temperature and composition. A columnar growth from the bottom of the pool was observed, with varying DAS and orientation depending on the location in the pool and the moving speed of laser beam. Confirming reports of previous experimental works, dendrite growth could occur even at the high cooling rates of the LENS process, with DAS as small as a few microns and transition from dendrite to cellular grain in high enough cooling rate. The effect of process conditions, in particular, the laser moving speed, the layer thickness, and the substrate size, on the solidification microstructure was investigated.

The model was also adopted to simulate solute controlled dendrite growth in hexagonal crystal metals – magnesium alloy AZ91 (approximated with the binary Mg-

8.9wt%Al), and perfect six-fold symmetrical dendrite shape was predicted by using a honeycomb-like FE mesh and hexagonal CA cells. Additionally, a 2D model, which coupled LB method and CA technique, was developed to simulate dendrite growth during the solidification. LB method was adopted to simulate the temperature field, solute concentration, and fluid flow, while the CA was used to simulate the dendrite growth. Besides, the dendrite growth in convection was also predicted in LB-CA model.

7.2 Future works

7.2.1 Dendrite growth in whole molten pool

In this research, the dendrite growth in the molten pool during LENS process is simulated, but it is only for small square calculation domain in the pool. Actually the nucleation occurs at the S/L boundaries and continuously grows in the whole pool (see Figure 7.1(a)). So simulation of the dendrite growth for the whole pool can be more reasonable. Figure 7.1(b) shows the solute concentration predicted by present solidification model for the whole pool, indicating that the growth directions are different at the locations close to the surface from those close to the bottom. However, the details of dendrite arm cannot be seen since the coarse mesh size (~5μm) adopted in this simulation comparing to the fine DAS (<5μm).

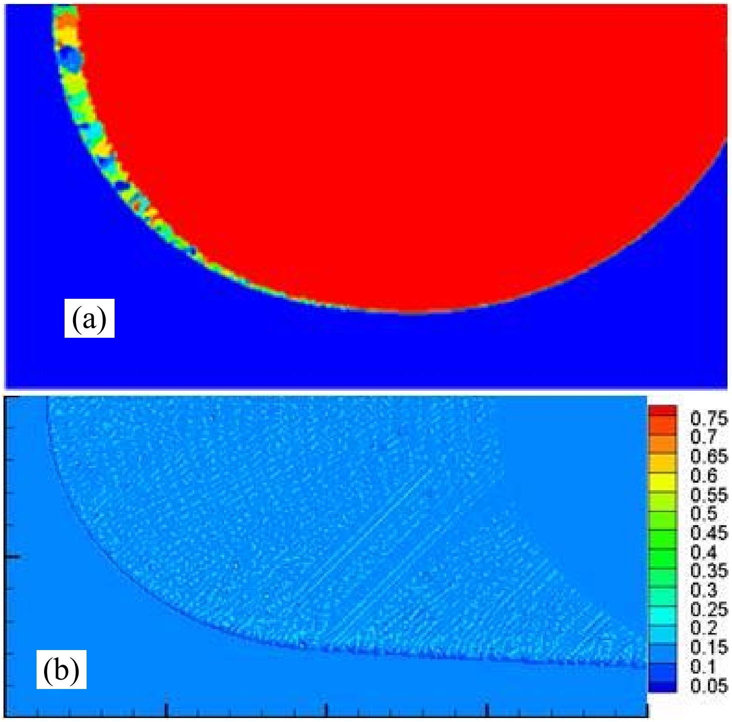

Figure 7.1 (a) Nucleation occur at S/L boundary, and (b) solute concentration of C

7.2.2 Dendrite growth in convection

The simulation of dendrite growth in the convection is one of the popular research topics for the solidification microstructure evolution modeling. A single nucleus is set at the center of the calculation domain to simulate the dendrite growth in the convection with uniform and constant inlet flow velocity at the left side. Figure 7.2 shows the dendrite morphologies with inflow velocity at 0.005 m/s (Figure 7.2(a)) and 0.03 m/s (Figure 7.2(b)). At the S/L in the upstream direction, the flow takes away the composition and increases equilibrium temperature, thus increasing the solid fraction and tip velocity. So, the higher inflow velocity leads to larger tip velocity and makes the dendrite morphology more asymmetric.

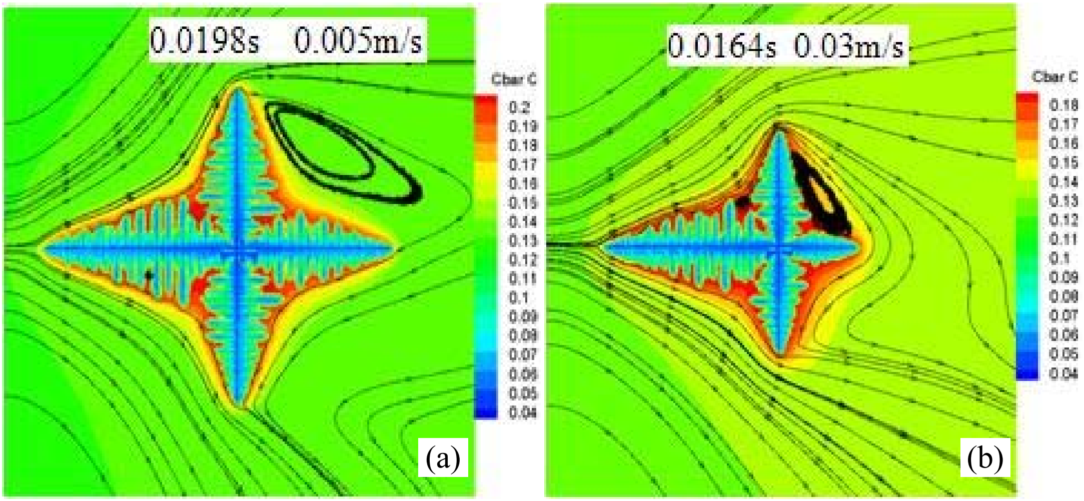

Figure 7.2 Single dendrite morphology in convection at inflow velocity of (a) 0.005m/s and (b) 0.03m/s

The influence of convection on the dendrite growth at the bottom of the molten pool is examined for different moving speeds of laser beam (see Figure 7.3(a)). Figure 7.3(b) and (c) show the dendrite structure with and without convection at the laser moving speed of 10mm/s. The dendrite growth direction and morphology is obviously different considering the convection from that without it. Figure 7.3(d) and (e) show the dendrite structure with and without convection at the laser moving speed of 20mm/s. There is not much difference in the dendrite microstructure whether or not the convection is considered. Higher laser scanning speed corresponds to higher cooling rate and solidification velocity, so it can be said that solidification microstructure is affected by convection, but the magnitude of the influence is determined partly by the solidification velocity.

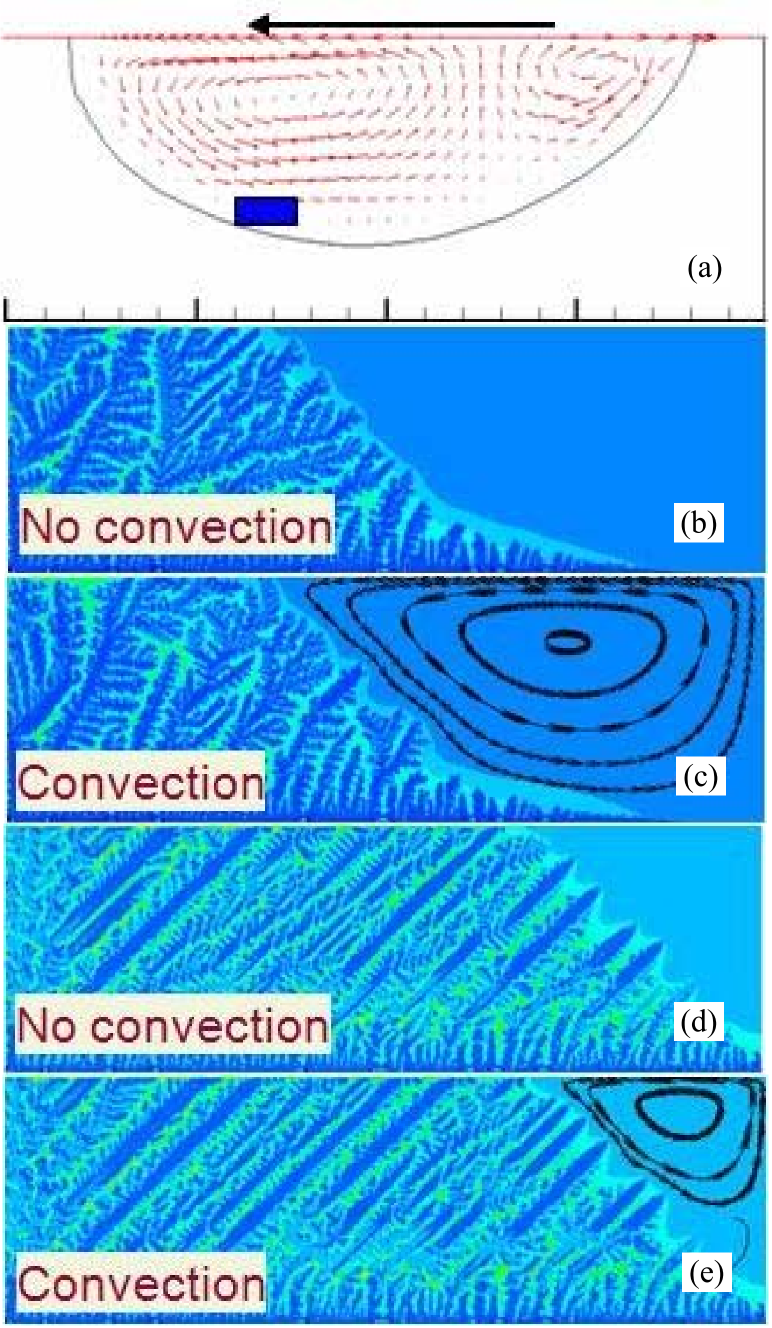

Figure 7.3 Calculation domain close to bottom in pool (a); dendrite morphologies without ((b) and (d)) or with ((c) and (e)) considering convection at laser moving speed of 10mm/s ((b) and (c)) and 20mm/s ((d) and (e))

7.2.3 3D model of dendrite with LB method

The 2D single dendrite growth simulation is carried out as discussed in Chapter VI, which couples the LB method and CA technique. The calculation of fluid flow with LB method can save much time. Also this method is easy to be implemented in parallel algorithm, so, it is possible to develop a 3D LB-CA solidification model to simulate the heat/mass transfer, fluid flow, and dendrite growth. Additionally, the application of this 3D model to the dendrite growth in the molten pool during LENS process will be another challenging topic.

7.2.4 Dendrite growth simulation of HCP materials

Chapter V presents the modeling development with hexagonal mesh for HCP crystal structure materials (Mg-Al binary alloy). Single dendrite (preferential direction of 0) growth process is simulated. However, the crystallographic orientation is random, so a solidification model that can predict the dendrite growth in any direction could be of future research interest.

REFERENCES

[1] http://www.matter.org.uk/steelmatter/metallurgy/strength/6_1_1.html

[2] http://www.freepatentsonline.com/6908516.html

[3] H B Dong, "Analysis of grain selection during directional solidification of gas turbine blades," Proceedings of the World Congress on Engineering Vol II, WCE, 2007 July 2-4, 2007, London, UK.

[4] C L Atwood, M L Griffith, M E Schlienger, L D Harwell, M T Ensz, D M Keicher, M E Schlienger, J A Romero, and J E Smugeresky, 1998, "Laser engineered net shaping (LENS): a tool for direct fabrication of metal parts," Proceedings of ICALEO '98, November 16-19, 1998, Orlando, FL, pp. E-1.

[5] G Richard, "Laser engineered net shapes," *Advanced Materials & processes*, 161(1), 2003, pp. 45-46.

[6] J W Sears, "Solid freeform fabrication technologies: Rapid prototyping- rapid manufacturing," *Int. J. Powder Metall*., 37(2), 2001, pp. 29-30.

[7] W Kurz, "Solidification Microstructure-Processing Maps: Theory and Application," *Adv. Eng. Mater*., 3(7), 2001, pp. 443-452.

[8] S M Kelly and S L Kampe, "Microstructural evolution in laser-deposited multilayer Ti-6Al-4V builds: Part II Thermal Modeling," *Metall. Mater. Trans. A*, 35(6), 2004, pp. 1869-1879.

[9] R Colaco and R Vilar, "Effect of the processing parameters on the proportion of retained austenite in laser surface melted tool steels," *J. mater. Sci. Lett*., 17(7), 1998, pp. 563-567.

[10] R Colaco and R Vilar, "Effect of laser surface melting on the tempering behavior of DIN X42Cr13 stainless tool steel," *Scr. Mater*., 38(1), 1998, pp. 107-113.

[11] M L Griffith, M E Schlienger, L D Harwell, M S Oliver, M D Baldwin, M T Ensz, J E Smugeresky, M Essien, J Brooks, C V Robino, W H Hofmeister, M J Wert, and D V Nelson, Proceedings of the Solid Freeform Fabrication Symposium, The University of Texas at Austin, Austin, TX, 1998, pp. 89-97.

[12] M L Griffith, M E Schlienger, L D Harwell, M S Oliver, M D Baldwin, M T Ensz, M Essien, J Brooks, C V Robino, J E Smugeresky, W H Hofmeister, M J Wert, and D V Nelson, “Understanding thermal behavior in the LENS process,” *Materials and Design*, 20(2), 1999, pp. 107-113.

[13] M L Griffith, M T Ensz, J D Puskar, C V Robino, J A Brooks, J A Philliber, J E Smugeresky, and W H Hofimeister, “Understanding the Microstructure and Properties of Components Fabricated by Laser Engineered Net Shaping (LENS)” MRS Spring Meeting, San Francisco, CA, 04/24-27, 2000.

[14] A J Pinkertona, M Karadge, W Syed, and L Li, “Thermal and microstructural aspects of the laser direct metal deposition of waspaloy,” *Journal of Laser Applications*, 18(3), 2006, pp. 216-226.

[15] P Peyre, P Aubry, R Fabbro, R Neveu, and A Longuet, “Analytical and numerical modeling of the direct metal deposition laser process,” *J. Phys. D: Appl. Phys.*, 41(2), 2008, pp. 025403.

[16] W Hofmeister, M Wert, J Smugeresky, J Philliber, Griffith, and M Ensz, “Investigating Solidification with the Laser-Engineered Net Shaping (LENS^{TM}) Process,” *JOM-e*, 51(7), 1999, http://www.tms.org/pubs/journals/JOM/9907/Hofmeister/Hofmeister-9907.html

[17] D Hu and R Kovacevic, “Modelling and measuring the thermal behavior of the molten pool in closed-loop controlled laser-based additive manufacturing,” *Proc. Instn Mech. Engrs Part B: J. Engineering Manufacture*, 217, 2003, pp. 441-452.

[18] L Han, F W Liou, and S Musti, “Thermal Behavior and Geometry Model of Melt Pool in Laser Material Process,” *Journal of Heat Transfer*, 127(9), 2005, pp. 1005-1014.

[19] M Grujicic, G Gao, and R S Figliola, “Computer simulations of the evolution of solidification microstructure in the LENS rapid fabrication process,” *Appl. Surf. Sci.*, 183(1-2), 2001, pp. 43-57.

[20] M Grujicic, Y Hu, G M Fadel, and D M Keicher, “Optimization of the LENS rapid fabrication process for in-flight melting of feed powder,” *J. Mater. Synth. Process.*, 9(5), 2002, pp. 223-233.

[21] R Jendrzejewski, I Kreja, and G Sliwinski, “Temperature distribution in laser-clad multi-layers,” *Materials Science and Engineering A*, 379, 2004, pp. 313-320.

[22] L Wang and S Felicelli, “Analysis of thermal phenomena in LENS deposition,” *Materials Science and Engineering A*, 435-436(5), 2006, pp. 625-631.

[23] R Ye, John E. Smugeresky, B Zheng, Y Zhou, and Enrique J Lavernia, “Numerical modeling of the thermal behavior during the LENS process,” *Materials Science and Engineering A*, 428(1-2), 2006, pp. 47-53.

[24] L Costa, R Vilar, T Reti, and A M Deus, “Rapid tooling by laser powder deposition: Process simulation using finite element analysis,” *Acta Mater*., 53(14), 2005, pp. 3987-3999.

[25] M Alimardani, E Toyserkani, and J P Huissoon, “A 3D dynamic numerical approach for temperature and thermal stress distributions in multilayer laser solid freeform fabrication process,” *Optics and Lasers in Engineering*, 45(12), 2007, pp. 1115-1130.

[26] K Dai and L Shaw, “Finite element analysis of the effect of volume shrinkage during laser densification,” *Acta Materialia*, 53, 2005, pp. 4743-4754.

[27] M Labudovic, D Hu, and R Kovacevic, “A three dimensional model for direct laser metal powder deposition and rapid prototyping,” *Journal of Materials Science*, 38(1), 2003, pp. 35-49.

[28] L Wang, S Felicelli, Y Gooroochurn, P T Wang, and M F Horstemeyer, “Numerical simulation of the temperature distribution and solid-phase evolution in the LENS process” Proceedings of SFF 2006 – 17th Solid Freeform Fabrication Symposium, Austin, Texas (U.S.A.), August 2006, pp. 453-463.

[29] X He, T DebRoy, and P W Fuerschbach, “Alloying element vaporization during laser spot welding of stainless steel,” *J. Phys. D: Appl. Phys*., 36, 2003, pp. 3079-3088.

[30] X He, J T Norris, P W Fuerschbach, and T DebRoy, “Liquid metal expulsion during laser spot welding of 304 stainless steel,” *J. Phys. D: Appl. Phys*., 39, 2006, pp. 525-534.

[31] N Allalou, E H Amara, N Mebani, L Achab, and F Hamadi, “Modeling of Heat Transfer and Fluid Flow during Laser Welding of Aluminum,” CAOL 2005, 12-17 Sept. Yalta, Crimea, Ukraine, pp. 98-101.

[32] W Sudnik, D Radaj, S Breitschwerdt, and W Erofeew, “Numerical simulation of weld pool geometry in laser beam welding,” *J. Phys. D: Appl. Phys*., 33, 2000, pp. 662-671.

[33] A De and T Debroy, “Reliable Calculations of Heat and Fluid Flow during Conduction Mode Laser Welding,” *Welding Journal*, July 2005, pp. S101-112.

[34] H Du, L Hu, J Liu, and X Hu, “A study on the metal flow in full penetration laser beam welding for titanium alloy,” *Computational Materials Science*, 29, 2004, pp. 419-427.

[35] Shakeel Safdar, Lin Li, and M A Sheikh, “Numerical analysis of the effects of non-conventional laser beam geometries during laser melting of metallic materials,” *J. Phys. D: Appl. Phys*., 40, 2007, pp. 593-603.

[36] M Sundar, A K Nath, D K Bandyopadhyay, S P Chaudhuri, P K Dey, and D Misra, “Numerical simulation of melting and solidification in laser welding of mild steel,” *Int. J. Computational Materials Science and Surface Engineering*, 1(6), 2007, pp. 717-733.

[37] X H Ye and X Chen, “Three-dimensional modelling of heat transfer and fluid flow in laser full-penetration welding,” *J. Phys. D: Appl. Phys*., 35, 2002, pp. 1049-1056.

[38] M Hughes, G A Taylor, and K Pericleous, “Thermocapillary and Magnetohydrodynamic Effects in Modelling the Thermodynamics of Stationary Welding Processes,” http://people.brunel.ac.uk/~eesrgat/research/pdf_pubs/phoenics00.pdf

[39] X He, J W Elmer, and T DebRoy, “Heat transfer and fluid flow in laser microwelding,” *Journal of Applied Physics*, 97, 2005, pp. 084909-1-9.

[40] R Rai, G G Roy, and T DebRoy, “A computationally efficient model of convective heat transfer and solidification characteristics,” *Journal of Applied Physics*, 101, 2007, pp. 054909-1-11.

[41] X He, P W Fuerschbach, and T DebRoy, “Heat transfer and fluid flow during laser spot welding of 304 stainless steel,” *J. Phys. D: Appl. Phys*., 36, 2003, pp. 1388-1398.

[42] A Kumar and T. Debroy, “Tailoring Complex Weld Geometry through Reliable Heat-Transfer and Fluid-Flow Calculations and a Genetic Algorithm,” *Metall. Mater. Trans. A*, 36, 2005, pp. 2725-2735.

[43] N Chakraborty and S Chakraborty, “Modelling of turbulent molten pool convection in laser welding of a copper-nickel dissimilar couple,” *Int. J. of Heat and Mass Transfer*, 50, 2007, pp. 1805-1822.

[44] G G Roy, J W Elmer, and T DebRoy, “Mathematical modeling of heat transfer, fluid flow, and solidification during linear welding with a pulsed laser beam,” *J. of Appl. Physics*, 100, 2006, pp. 034903-1-7.

[45] G Phanikumar, K Chattopadhyay, and P Dutta, “Modelling of transport phenomena in laser welding of dissimilar metals,” *Int. J. of Numerical Methods for Heat and Fluid Flow*, 11(2), 2001, pp. 156-171.

[46] W Zhang, C H Kim, and T DebRoy, “Heat and fluid flow in complex joints during gas metal arc welding—Part I Numerical model of fillet welding,” *J. of Applied Physics*, 95(9), 2004, pp. 5210-5219.

[47] H Ki, P S. Mohanty, and J Mazumder, “A Numerical Method for Multiphase Incompressible Thermal Flows with Solid-Liquid and Liquid-Vapor Phase Transformations,” *Numerical Heat Transfer, PartB: Fundamentals*, 48(2), 2005, pp. 125-145.

[48] E J Ha and W S Kim, “A study of low-power density laser welding process with evolution of free surface,” *International Journal of Heat and Fluid Flow*, 26, 2005, pp. 613-621.

[49] H Qi, J Mazumder, and H Ki, “Numerical simulation of heat transfer and fluid flow in coaxial laser cladding process for direct metal deposition,” *J. of Applied Physics*, 100(2), 2006, pp. 024903.

[50] L HAN, F W Liou, and K M Phatak, “Modeling of Laser Cladding with Powder Injection,” *Metall. Mater. Trans. B*, 35B, 2004, pp. 1139-1150.

[51] J Choi, L Han, and Y Hua, “Modeling and Experiments of Laser Cladding with Droplet Injection,” *Journal of Heat Transfer*, 127(9), 2005, pp. 978-986.

[52] Y P Lei, H Murakawab, Y W Shi, and X Y Li, “Numerical analysis of the competitive influence of Marangoni flow and evaportation to theat surface temperature and molten pool shape in laser remelting,” *Computational Materials Science*, 21(3), 2001, pp. 276-290.

[53] L X Yang, X F Peng, and B X Wang, “Numerical modeling and experimental investigation on the characteristics of molten pool during laser processing,” *International Journal of Heat and Mass Transfer*, 44(23), 2001, pp. 4465-4473.

[54] J Brooks, C Robino, T Headley, S Goods, and M Griffith, “Microstructure and Property Optimization of LENS Deposited H13,” 2000, Solid freeform fabrication proceeding, pp. 200-208.

[55] T Miokovic, V Schulze, O Vohringer, and D Lohe, “Influence of cyclic temperature changes on the microstructure of AISI 4140,” *Acta Materialia*, 55, 2007 pp. 589-599.

[56] Y Xiong, J E Smugeresky, L Ajdelsztajn, and J M Schoenung, “Fabrication of WC-Co cermets by laser engineered net shaping,” *Materials Science and Engineering A*, 493(1-2), 2008, pp. 261-266.

[57] B Zheng, Y Zhou, J E Smugeresky, and E J Lavernia, “Processing and behavior of Fe-based metallic glass components via Laser-Engineered Net Shaping,” *Metall. Mater. Trans. A*, 40, 2009, pp. 1235-1245.

[58] M J Tobar, C Álvarez, J M Amado, A Ramil, E Saavedra, and A Yáñez, “Laser transformation hardening of a tool steel: Simulation based parameter optimization and experimental results,” *Surface & Coatings Technology*, 200, 2006, pp. 6362-6367.

[59] B. Zheng, Y. Zhou, J E Smugeresky, J M Schoenung, and E J Lavernia, “Thermal behavior and microstructure evolution during laser deposition with Laser-Engineered Net Shaping: Part II Experimental Investigation and Discussion,” *Metall. Mater. Trans. A*, 39, 2008, pp. 2237-2245.

[60] D Gill, J Smugeresky, and C J. Atwood, “Repeatability analysis of 304L deposition by the LENS ® Process,” 2006, Solid Freeform Fabrication Proceedings, pp. 782-788.

[61] C L Atwood, M L Griffith, L D Harwell, D L Greene, D E Reckaway, M T Ensz, D M Keicher, M E Schlienger, J A Romero, M S Oliver, F P Jeantette, and J E Smugeresky, “Laser spray Fabrication for Net-Shape Rapid 316SS,” Sandia Report, 1999

[62] M L Grffith, M T Ensz, D L Greene, D E Reckaway, J A Morin, T E Bucheit, T B Crenshaw, D A Lavan, V Tikare, and J A Romero, “Laser Wire Deposition for fully Dense Shapes LDRD,” Sandia Report, 1999

[63] J W Sears, “Direct Laser Powder Deposition State of the Art,” Sandia Report, 2000.

[64] D D Gill, J E Smugeresky, C V Robino, M F Harris, and M L Griffith, “On the Interface Between LENS Deposited Stainless Steel 304L Repair Geometry and Cast or Machined Components,” Sandia Report, 2004

[65] David D Gill, John E Smugeresky, Clinton J Atwood, Michael D Jew, and Simon Scheffel, “Process Qualification and Testing of LENS Deposited AY1E0125 D-Bottle Brackets,” Sandia Report, 2006

[66] Y Zhang, M Xi, S Gao, and L Shi, “Characterization of laser direct deposited metallic parts,” *Journal of Materials Processing Technology*, 142, 2003, pp. 582-585.

[67] V Neela and A De, “Numerical modeling of LENS process using special element features,” Abaqus India Regional Users’ Meet, 2007, pp. 1-11.

[68] S Ghosh and J Choi, “Modeling and Experimental verification of transient/residual stresses and microstructure formation of multi-layer laser aided DMD process,” *J. Heat Trans.*, 128(7), 2006, pp. 662-679.

[69] B Zheng, Y Zhou, J E Smugeresky, J M Schoenung, and EJ Lavernia. “Thermal behavior and micro-structural evolution during laser deposition with laser engineered net shaping: Part I. Numerical calculations,” *Metall. Mater. Trans. A*, 39, 2008, pp. 2228-2236.

[70] W Hofmeister, M Griffith, M Ensz, and J Smugeresky, “Solidification in Direct Metal Deposition by LENS Processing,” *JOM*, 2001, pp. 30-34.

[71] W Hofmeister, M Wert, J Smugeresky, J A Philliber, M Griffith, and M Ensz, “Investigation of Solidification in the Laser Engineered Net Shaping (LENS^{TM}) Process,” *JOMe*, 1999, pp. 1-7.

[72] W Syed, A J Pinkerton, and L Li, “A comparative study of wire feeding and powder feeding in direct diode laser deposition for rapid prototyping,” *Applied Surface Science*, 247(1-4), 2005, pp. 268-276.

[73] J Choi and Y Chang, “Characterisitics of laser aided direct metal material deposition process for tool steel,” *Int. J. of Machine Tools & Manufacture*, 45(4-5), 2005, pp. 597-607.

[74] G Bi, A Gasser, K Wissenbach, A Drenker, and R Poprawe, “Characterization of the process control for the direct laser metallic powder deposition,” *Surface & Coatings Technology*, 201(6), 2006, pp. 2676-2683.

[75] J Mazumder, A Schifferer, and J Choi, “Direct materials deposition designed macro and microstructure,” *Mater. Res. Innovat*, 3(3), 1999, pp. 118-131.

[76] G P Dina, A K Dasgupta, and J Mazumder, “Laser aided direct metal deposition of Inconel 625 superalloy Microstructural evolution and thermal stability,” *Materials Science and Engineering A*, 509(1-2), 2009, pp. 98-104.

[77] Q Y Pan, X Lin, W D Huang, Y H Zhou, and G L Zhang, “Microstructure evolution of Cu-Mn alloy under laser rapid solidification conditions,” *Materials Research Bulletin*, 33(11), 1998, pp. 1621-1633.

[78] K Zhang, W Liu, and X Shang, “Research on the processing experiments of laser metal deposition shaping,” *Optics & Laser Technology*, 39, 2007, pp. 549-557.

[79] W Liu and J N DuPONT, “Direct laser deposition of a single-crystal Ni3Al-based IC221W alloy,” *Metall. Mater. Trans. A*, 36, 2005, pp. 3397-3406.

[80] Y Bao, J Ruan, T E Sparks, J Anand, J Newkirk, and F Liou, “Evaluation of Mechanical Properties and Microstructure for Laser Deposition Process and Welding Process,” Solid Freeform Fabrication Proceedings, 2006, pp. 280-289.

[81] W Liu and J N DuPONT, “In-situ reactive processing of nickel aluminides by laser-engineered net Shaping,” *Metall. Mater. Trans. A*, 34(11), 2003, pp. 2633-2641.

[82] W Hofmeister, M Wert, J Smugeresky, J A Philliber, M Griffith, and M Ensz, “Investigation of Solidification in the Laser Engineered Net Shaping (LENS^{TM}) Process,” *JOMe*, 1999, pp. 1-7.

[83] G Bi, A Gasser, K Wissenbach, A Drenker, R Poprawe, “Investigation on the direct laser metallic powder deposition process via temperature measurement,” *Applied Surface Science*, 253(3), 2006, pp. 1411-1416.

[84] G K Lewisa, and E Schlienger, “Practical Considerations and capabilities for laser assisted direct metal deposition,” *Materials and Design*, 21(4), 2000, pp.417-423.

[85] J Song, Q Deng, C Chen, D Hu, and Y Li, “Rebuilding of metal components with laser cladding forming,” *Applied Surface Science*, 252, 2006, pp. 7934-7940.

[86] M L Griffith, M T Ensz, D L Greene, D E Reckaway, J A Romero, T B Crenshaw, L D Harwell, T E Buchheit, and V Tikare, “Solid Freeform Fabrication using the Wirefeed Process,” Sandia Report, Aug. 1999.

[87] M L Griffith, M T Ensz, D L Greene, D E Reckaway, J A Morin, T E Buchheit, T B Crenshaw, D A Lavan, V Tikare, and J A Romero, “Laser Wire Deposition (WireFeed) for Fully Dense Shapes LDRD,” Sandia Report, Nov.1999.

[88] W H Hofmeister, M L Griffith, M T Ensz, and J E Smugeresky, “Solidification in direct metal deposition by LENS processing,” *JOM*, 53(9), 2001, pp. 30-34.

[89] J A Brooks, T J Headley, and C V Robino, “Microstructures of Laser Deposited 304L Austenitic Stainless Steel,” Sandia report, Jun. 2000.

[90] J E Smugeresky, D M Keicher, J A Romero, M L Griffith, and L D Harwell, “Laser Engineered Net Shaping (LEMSTM) Process: Optimization of Surface Finish and Microstructural Properties,” Sandia Report, Sept. 1997.

[91] T Sparks, J Ruan, Z Fan, Y Bao, and F Liou, “Effect of structured laser pulses on grain growth in H13 tool steel, Solid Freeform Fabrication Proceedings,” 2006, pp. 261-267.

[92] M Gaumann, C Bezencon, P Canalis, and W Kurz,” Single-crystal laser deposition of superalloys: Processing-microstructure maps,” *Acta Mater*., 49(6), 2001, pp. 1051-1062.

[93] W Liu and J N DuPont, “Effects of melt-pool geometry on crystal growth and microstructure development in laser surface-melted superalloy single crystals: Part I Mathematical modeling of single-crystal growth in a melt pool,” *Acta Materialia*, 52(16), 2004, pp. 4833-4847.

[94] S Bontha, N W Klingbeil, P A Kobryn, and H L Fraser, “Thermal process maps for predicting solidification microstructure in laser fabrication of thin-wall structures,” *J. of Mater. Processing Tech.*, 178(1-3), 2006, pp. 135-142.

[95] P A Kobryn and S L Semiatin, “Microstructure and texture evolution during solidification processing of Ti-6Al-4V,” *Journal of Materials Processing Technology*, 135, 2003, pp. 330-339.

[96] P C Collins, R Banerjee, S Banerjee, and H L Fraser, “Laser deposition of compositionally graded titanium-vanadium and titanium-molybdenum alloys,” *Mater. Sci. Eng. A*, 352(1-2), 2003, pp. 118-128.

[97] P A Kobryn, E H Moore, and S L Semiatin, “Effect of laser power and traverse speed on microstructure, porosity, and build height in laser-deposited Ti-6Al-4V,” *Scripta Mater.*, 43(4), 2000, pp. 299-305.

[98] P S Korinko and T M Adams, “Hydrogen Effects on Laser Engineered Net Shape (LENS) Repaired Weldments,” 8th Global Innovations Symposium: Trends in Materials and Manufacturing Technologies for Energy Production Edited by TMS (The Minerals, Metals & Materials Society), 2007, pp. 57-65.

[99] V Pavlyk and U Dilthey, “Simulation of weld solidification microstructure and its coupling to the macroscopic heat and fluid flow modeling,” *Modelling Simul. Mater. Sci. Eng.*, 12, 2004, pp. S33-S45.

[100] R S Miller, G Cao, and M Grujicic, “Monte Carlo Simulation of Three-Dimensional Nonisothermal Grain-Microstructure Evolution: Application to LENS Rapid Fabrication,” *Journal of Materials Synthesis and Processing*, 9(6), 2001, pp. 329-345.

[101] H Hu and S A Argyropoulos, “Mathematical modeling of solidification and melting: a Review,” *Modelling Simul. Mater. Sci. Eng.*, 4, 1996, pp. 371-396.

[102] M Rappaz, “Modelling of microstructure formation in solidification process,” *Int. Materials Reviews*, 34(3), 1989, pp. 93-123.

[103] D M STEFANESCU, “Methodologies for modeling of solidification microstructure and their capabilities,” *ISIJ International*, 35(6), 1995, pp. 637-650.

[104] W J Boettinger, S R Coriell, A L Greer, A Karma, W Kurz, M Rappaz, and R Trivedi, “Solidification Microstructure: Recent Developments, Future Directions,” *Acta Mater.*, 48, 2000, pp. 43-70.

[105] M Asta, C Beckermann, A Karma, W Kurz, R Napolitano, M Plapp, G Purdy, M Rappaz, and R Trivedi, “Solidification microstructures and solid-state parallels: Recent developments, future directions,” *Acta Materialia*, 57, 2009, pp. 941-971.

[106] C Y Li, S V Garimella, and J E Simpson, “Fixed-grid front-tracking algorithm for solidification problems, Part I: method and validation,” *Numerical Heat Transfer, Part B*, 43, 2003, pp. 117-141.

[107] P Zhao and J C Heinrich, “Front-Tracking Finite Element Method for Dendritic Solidification,” *J. of Computational Physics*, 173, 2001, pp. 765-796.

[108] D Juric and G Tryggvason, “Front-Tracking Method for Dendritic Solidification,” *Journal of Computational Physics*, 123, 1996, pp. 127-148.

[109]. J. Langer 1978, http://en.wikipedia.org/wiki/Phase_field_models

[110] J A Warren and W J Boettinger, “Prediction of dendritic growth and microsegregation patterns in a binary alloy using the phase-field method,” *Acta Metall. Mater*., 43(2), 1995 pp. 689-703.

[111] J A Warren, W J Boettinger, C Beckermann, and A Karma, “Phase-field simulation of solidification,” *Annu. Rev. Mater. Res*., 32, 2002, pp. 163-194.

[112] X Tong, C Beckermann, A Karma, and Q Li, “Phase-field simulations of dendritic crystal growth in a forced flow,” *Phys. Rev. E*, 63(6), 2001, pp.061601-1-16.

[113] R Kobayashi, “Modeling and numerical simulations of dendritic crystal growth,” *Physica D*, 63(3-4), 1993, pp. 410-423.

[114] A A Wheeler, W J Boettinger, and G B McFadden, ”Phase-field model for isothermal phase transitions in binary alloys,” *Phys. Rev. A*, 45(10), 1992 pp. 7424-7439.

[115] L Tan and N Zabaras, “A level set simulation of dendritic solidification with combined features of front-tracking and fixed-domain methods,” *Journal of Computational Physics*, 211, 2006, pp. 36-63.

[116] F Gibou, R Fedkiw, R Caflisch, and S Osher, “A Level Set Approach for the Numerical Simulation of Dendritic Growth,” *Journal of Scientific Computing*, 19, 2003, pp. 1-3.

[117] Y T Kim, N Goldenfeld, and J Dantzig, “Computation of dendritic microstructures using a level set method,” *Physical Review E*, 62(2), 2000, pp. 2471-2474.

[118] Von Neumann and Burk, http://en.wikipedia.org/wiki/Cellular_automaton

[119] Z Gürdal and T Brian, “Cellular Automata for Design of Truss Structures with Linear and Nonlinear Response,” 41st AIAA/ASME/ASCE/ AHS/ASC Structures, Structural Dynamics and Materials Conference & Exhibit, April 3-6, 2000 Atlanta, Georgia

[120] D Raabe, "Cellular automata in materials science with particular reference to recrystallization simulation," *Annual Review of Materials Research*, 32, 2002, pp. 53-76.

[121] W Wang, P D Lee, and M McLean, "A model of solidification microstructures in nickel-based superalloys: predicting primary dendrite spacing selection," *Acta Materialia*, 51(10), 2003, pp.2971-2987.

[122] M F Zhu and C P Hong, "A Modified Cellular Automaton Model for the Simulation of Dendritic Growth in Solidification of Alloys," *ISIJ International*, 41(5), 2001, pp. 436-445.

[123] S Raghavan and S S Sahay, "Modeling the grain growth kinetics by cellular automaton," *Mater. Sci. Eng. A*, 445-446, 2007, pp. 203-206.

[124] W Yu, C D Wright, S P Banks, and E J Palmiere, "Cellular automata method for simulating microstructure evolution," *IEE Proc.-Sci. Meas. Technol.*, 150(5), 2003, pp. 211-213.

[125] K Kremeyer, "Cellular Automata Investigations of Binary Solidification," J. *of Computational Physics*, 142(1), 1998, pp. 243-262.

[126] A Burbelko, E Fras, W Kapturkiewicz, and E Olejnik, "Cellular Automata Diffusion-Kinetic Model of Dendritic Growth," P.M.A. Sloot, B. Chopard, and A.G. Hoekstra (Eds.): ACRI 2004, LNCS 3305, 2004, pp. 355-364.

[127] M B Cortie, "Simulation of Metal Solidification Using a Cellular Automaton," *Metall. Trans. B*, 24, 1993, pp. 1045-1053.

[128] L Nastac, S Sundarraj, K O Yu, and Y Pang, "The Stochastic Modeling of Solidification Structures in Alloy 718 Remelt Ingots," *JOM*, 1998, pp. 30-35.

[129] KY Lee and C P Hong, "Stochastic Modeling of Solidification Grain Structures of Al-Cu Crystalline Ribbons in Planar Flow Casting," *ISIJ International*, 37(1), 1997, pp. 38-46.

[130] M Nakagawa, Y Natsume, and K Ohsasa, "Dendrite Growth Model Using Front Tracking Technique with New Growth Algorithm," *ISIJ International*, 46(6), 2006, pp. 909-913.

[131] M Yamazaki, Y Natsume, H Harada, and K Ohsasa, "Numerical Simulation of Solidification Structure Formation during Continuous Casting in Fe-0.7mass%C Alloy Using Cellular Automaton Method," *ISIJ International*, 46(6), 2006, pp. 903-908.

[132] M J M Krane, D R Johnson, and S Raghavan, "The development of cellular automaton-finite volume model for dendritic growth," *Appl. Math. Model.*, 33, 2009, pp. 2234-2247.

[133] M Rappaz and Ch A Gandin, "Probabilistic modelling of microstructure formation in solidification processes, *Acta Metall. Mater.*, 41(2), 1993, pp. 345-360.

[134] Ch A Gandin and M Rappaz, "Coupled finite element-cellular automation model for the prediction of dendritic grain structures in solidification processes," *Acta Metall. Mater.*, 42(7), 1994, pp. 2233-2246.

[135] L B Sanchez and D M Stefanescu, "Growth of solutal dendrites: A cellular automaton model and its quantitative capabilities," *Metall. Mater. Trans. A*, 34(2), 2003, pp. 367-382.

[136] L B Sanchez and D M Stefanescu, "A quantitative dendrite growth model and analysis of stability concepts," *Metall. Mater. Trans. A*, 35(8), 2004, pp. 2471-2485.

[137] M F Zhu and D M Stefanescu, "Virtual front tracking model for the quantitative modeling of dendritic growth in solidification of alloys," *Acta Mater.*, 55(5), 2007, pp. 1741-1755.

[138] M F Zhu and C P Hong, "Modeling of irregular eutectic microstructures in solidification of Al-Si alloys," *Metall. Mater. Trans. A*, 35(5), 2004, pp. 1555-1563.

[139]L Nastac, "Numerical modeling of solidification morphologies and segregation patterns in cast dendritic alloys," *Acta Mater.*, 47(17), 1999, pp. 4253-4262.

[140] H B Dong and P D Lee, "Simulation of the columnar-to-equiaxed transition in directionally solidified Al-Cu alloys," *Acta Mater.*, 53, 2005, pp. 659-668.

[141] R C Atwood, P D Lee, R S Minisandram, and R.M.Forbes Jones, "Multiscale modeling of microstructure formation during vacuum arc remelting of titanium 6-4," *J. of Mater. Sci.*, 39, 2004, pp. 7193-7197.

[142] W Wang, A Kermanpur, P D Lee, and M Mclean, "Simulation of dendritic growth in the plotform region of single crystal superalloy turbine baldes," *J. Mater. Sci.*, 38, 2003, pp. 4385-4391.

[143] M F Zhu, S Y Lee, and C P Hong, "Modified cellular automaton model for the prediction of dendritic growth with melt convection," *Phys. Rev. E*, 69(61), 2004, pp. 061610-1-12.

[144] Y H Shin and C P Hong, "Modeling of dendritic growth with convection using a modified cellular automation model with a diffuse interface," *ISIJ Int.*, 42(4), 2002, pp. 359-367.

[145] M F Zhu, C P Hong, D M Stefanescu, and Y A Chang, "Computational Modeling of Microstructure Evolution in Solidification of Aluminum Alloys," *Metall. Mater. Trans. B*, 38, 2007, pp. 517-524.

[146] A M Mullis, "Growth Induced Dendritic Bending and Rosette Formation during Solidification in a Shearing Flow," *Acta Mater.*, 47(6), 1999, pp.1783-1789.

[147] Ch A Gandin, J L Desbiolles, M Rappaz, and Ph Thevoz, "Three-dimensional cellular automaton-finite element model for the prediction of solidification grain structures," *Metall. Mater. Trans. A*, 30(12), 1999, pp. 3153-3165.

[148] S G R Brown and N B Bruce, "Three-dimensional cellular automaton models of microstructural evolution during solidification," *J. of Mater. Sci.*, 30(5), 1995, pp. 1144-1150.

[149] Ch A Gandin and M Rappaz, "A 3D Cellular Automaton Algorithm For The Prediction Of Dendritic Grain Growth," *Acta Mater.*, 45(5), 1997, pp. 2187-2195.

[150] B Liu, S Xiong, and Q Xu, "Study on Macro- and Micromodeling of the Solidification Process of Aluminum Shape Casting," *Metall. Maters. Trans. B*, 38, 2007, pp. 525-532.

[151] Y H Chang, S M Lee, K Y Lee, and C P Hong, "There-dimensional Simulation of Dendritic Grain Structures of Gas-atomized Al-Cu Alloy Droplets," *ISIJ International*, 38(1), 1998, pp. 63-70.

[152] Ch A Gandin, M Rappaz, and R Tintillier, "Three-dimensional probabilistic simulation of solidification grain structures: application to superalloy precision casting," *Metall. Trans A*, 24, 1993, pp. 467-479.

[153] M F Zhu and C P Hong, "A three dimensional modified cellular automaton model for the prediction of solidification microstructure," *ISIJ International*, 42(5), 2002, pp. 520-526.

[154] P D Lee, A Chirazi, R C Atwood, and W Wang, "Multiscale modeling of solidification microstructures, including microsegregation and microporosity in an Al-Si-Cu alloy," *Mater. Sci. and Eng. A*, 365, 2004, pp. 57-65.

[155] R Ye, Y Zhou, W Wei, J E Smugeresky, and E J Lavernia, "Numerical modeling of the thermal behavior during the LENS process," TMS, 2003, pp. 369-376.

[156] H Yin, S D Felicelli, and L Wang, "Comparison of 2D and 3D Thermal Models of the LENS Process," ASME *Journal of Heat Transfer*, 130(10), 2008, pp. 102101-1-7.

[157] A F Hoadley, M Rappaz, and M Zimmermann, "Heat-flow simulation of laser remelting with experimental validation," *Metall. Trans. B*, 22, 1991, pp. 101-109.

[158] S D Felicelli, D R Poirier, and P K Sung, "A model for prediction of pressure and redistribution of gas-forming elements in multicomponent casting alloys," *Metall. and Materials Trans. B.*, 31, 2000, pp. 1283-1292.

[159] L Wang and S Felicelli, "Thermal modeling and experimental validation in the LENS process", Solid Freeform Fabrication Symposium, Houston, TX, August 6-8, 2007.

[160] T DebRoy and S A David, "Physical processes in fusion welding", *Rev. Mod. Phys.*, 67, 1995, pp. 85-112.

[161] H. Yin, S. Felicelli, and L. Wang, Fluid Flow, Heat and Mass Transfer in the Molten Pool of LENS Processes. Materials Processing Fundamentals, edited by P. Anyalebechi, TMS, 2008, Warrendale, PA, 261-270.

[162] M C Flemings, Solidification Processing, McGraw-Hill, New York, NY, 1974, p. 148-154.

[163] S Katayama and A Matsunawa, "Solidification microstructure of laser welded stainless steels," Proc. of Mater. Processing Symposium, Laser Inst. of America. ICALEO, 44, 1984, pp.60

[164] Ph Thevoz, J L Desbiolles, and M Rappaz, "Modeling of equiaxed microstructure formation in casting," *Metall. Trans. A*, 20(2), 1989, pp. 311-322.

[165] J W Elmer, S M Allen, and T W Eager, "Microstructural development during solidification of stainless steel alloys," *Metall. Trans. A*, 20(10), 1989, pp. 2117-2131.

[166] J Choi and J Mazumder, "Numerical and experimental analysis for solidification and residual stress in the GMAW process for AISI 304 stainless steel," *J. Mater Sci.*, 37(10), 2002, pp. 2143-2158.

[167] L Wang and S Felicelli, "Process modeling in laser deposition of multilayer SS410 steel," *J. Manuf Sci Eng.*, 129(6), 2007, pp.1028-1034.

[168] L Wang, S Felicelli, Y Gooroochurn, P Wang, M Horstemeyer, "Optimization of the LENS® process for steady molten pool size," *Mater. Sci. Eng. A*, 474(1-2), 2008, pp. 148-156.

[169] L Wang, S D Felicelli, and J Craig, "Experimental and numerical study of the LENS rapid fabrication process," *J. Manuf. Sci. Eng.*, 131(4), 2009, pp. doi:10.1115/1.3173952.

[170] T K Pal, "The structure and properties of laser beam welded stainless steels," Proc. of Mater, Processing Symposium, Laser Inst. of America. ICALEO, 89, 2000, pp. C192.

[171] H. Yin and S. D. Felicelli, "Dendrite growth simulation during solidification in the LENS process" *Acta Mater*., 58, 2010, pp. 1455-1465.

[172] H. Yin and S.D. Felicelli, Multi-scale solidification model for laser engineered net shaping (LENS) Process, Materials Processing Fundamentals, edited by P. Anyalebechi, TMS, 2010, Warrendale, PA.

[173] B Bottger, J Eiken, and I Steinbach, "Phase field simulation of equiaxed solidification in technical alloys," *Acta Mater*., 54(10), 2006, pp. 2697-2704.

[174] Z Y Liu, Q Y Xu, and B C Liu, "Dendrite growth modelling of cast magnesium alloy," *Int. J. of Cast Metals Research*, 20(3), 2007, pp.109-112.

[175] N Ricketts, Properties of Cast Magnesium Alloys, http://members.tripod.com/Mg/asm_prop.htm

[176] H Yan, W Zhuang, Y Hu, Q Zhang, and H Jin, "Numerical simulation of AZ91D alloy automobile plug in pressure die casting process," *J. of Mater. Processing Tech*., 187-188, 2007, pp. 349-353.

[177] H Hu and A Yu, "Numerical simulation of squeeze cast magnesium alloy AZ91D," *Modelling Simul. Mater. Sci. Eng*., 10(1), 2002, pp.1-11.

[178] Z Fu, Q Xu and S Xiong, "Microstructure simulation of die casting magnesium alloy," *Materials Science Forum*, 546-549, 2007, pp.133-137.

[179] T Borzsonyi, A Buka, and L Kramer, "Effect of the anisotropic surface tension, crystallization kinetics, and heat diffusion on nonequilibrium growth of liquid crystals," *Physical Review E*, 58(5), 1998, pp. 6236-6245.

[180] G S Grest, D J Srolovitz, and M P Anderson, "Cimputer simulation of grain growth – IV Anisotropic grain boundary energies," *Acta Metall*., 33(3), 1985, pp. 509-520.

[181] A Jacot and M Rappaz, "A pseudo-front tracking technique for the modelling of solidification microstructures in multi-component alloys," *Acta Mater*. 50(8), 2002, pp. 1909-1926.

[182] Q Du, and A Jacot, “A two-dimensional microsegregation model for the description of microstructure formation during solidification in multicomponent alloys: Formulation and behaviour of the model,” *Acta Mater*., 53(12), 2005, pp. 3479-3493.

[183] W Yang, L Chen, and G L Messing, “Computer simulation of anisotropic grain growth,” *Mater. Sci. Eng. A*, 195(1-2), 1995, pp. 179-187.

[184] J D Hunt and S Z Lu, “Numerical modeling of cellular/dendritic array growth: spacing and structure predictions,” *Metall. Maters. Trans. A*, 27(3), 1996, pp. 611-623.

[185] C H Caceres, C J Davidson, J R Griffiths, and C L Newton, “Effects of solidification rate and ageing on the microstructure and mechanical properties of AZ91 alloy,” *Mater. Sci. Eng. A*, 325(1-2), 2002, pp.344-355.

[186] C Labrecque, R Angers, R Tremblay, and D Dube, “Inverted disk centrifugal atomization of AZ91 magnesium alloy,” *Can. Metall. Q*., 36(3), 1997, pp. 169-175.

[187] D Dube, A Couture, Y Carbonneau, M Fiset, R. Angers, and R Tremblay, “Secondary dendrite arm spacings in magnesium alloy AZ91D: From plaster moulding to laser remelting,” *Int. J. Cast Metals Res*., 11(3), 1998, pp. 139-144.

[188] W P Sequeira, M T Murray, G L Dunlop, and D H StJohn, Proc. TMS Symposium on automotive alloys (Feburary 9-13, Orlando, FA.), The Minerals Metals and Materials Society (TMS), Warrendale, PA, 1997, pp.169-183.

[189] J Lipton, M E Glicksman, and W Kurz, “Dendritic growth into undercooled alloy melts,” *Mater. Sci. Eng*., 65(1), 1984, pp. 57-63.

[190] B Bottger, J Eiken, M Ohno, G Klaus, M Fehlbier, R Schmid-Fetzer, I Steinbach, and A Buhrig-Polaczek, “Controlling microstructure in magnesium alloys: A combined thermodynamic, experimental and simulation approach,” *Advanced Engineering Materials*, 8(4), 2006, pp. 241-247.

[191] H. Yin and S. D. Felicelli, “A Cellular Automaton Model for Dendrite Growth in Magnesium Alloy AZ91,” *Modelling Simul. Mater. Sci. Eng*., 17, 2009, pp. 075011.

[192] H. Yin and S.D. Felicelli, “Simulation of microstructure evolution during solidification of magnesium alloys,” Materials Processing Fundamentals, edited by P. Anyalebechi, TMS, 2009, Warrendale, PA, 627-634.

[193] M C Sukop and D T Thorne, Lattice Boltzmann Modeling: An Introduction for Geoscientists and Engineers, Springer-Verlag Berline Heidelberg, 2006.

[194] S Succi, The Lattice Boltzmann Equation for Fluid Dynamics and Beyond, Oxford University Press Inc., 2001.

[195] http://en.wikipedia.org/wiki/Lattice_Boltzmann_methods

[196] S Chen and G D Doolen, "Lattice Boltzmann method for fluid flows," *Annu. Rev. Fluid Mech*., 30, 1998, pp. 329-64.

[197] J M V A Koelman, "A Simple Lattice Boltzmann Scheme for Navier-Stokes Fluid Flow," *Europhysics Letters*, 15(6), 1991, pp. 603-607.

[198] R Benzi, S Succi, and M Vergassola, "The lattice Boltzmann-equation—theory and applications," *Phys. Rep*., 222, 1992, pp.145-97.

[199] H Chen, "Discrete Boltzmann systems and fluid flows," *Comp. Phys*., 7(6), 1993, pp. 632-637.

[200] E Aharonov, D H Rothman, "Non-Newtonian flow (through porous media): a lattice Boltzmann method," *Geophys. Res. Lett*., 20, 1993, pp. 679-682.

[201] R R nourgaliev, T N Dinh, T G Theofanous, and D Joseph, "The Lattice Boltzmann Equation Method: Theoretical Interpretation, Numerics and Implications," *International Journal of Multiphase Flow*, 29(1), 2003, pp. 117-169.

[202] D Rabbe, "Overview of the lattice Boltzmann method for nano- and microscale fluid dynamics in materials science and engineering," *Modelling Simul. Mater. Sci. Eng*., 12, 2004, pp. R13-R46.

[203] M Yoshino and T Inamuro, "Lattice Boltzmann simulations for flow and heat/mass transfer problems in a three-dimensional porous structure," *Int. J. Numer. Meth. Fluid*, 2003, 43, pp. 183-198.

[204] Y Zhou, R Zhang, I Staroselsky, and H Chen, "Numerical simulation of laminar and turbulent bouyancy-driven flows using a lattice Boltzmann based algorithm," *International Journal of Heat and Mass Transfer*, 47, 2004, pp. 4869-4879.

[205] X Shan, "Simulation of Rayleigh-Benard convection using a lattice Boltzmann method," *Physical Review E*, 55(3), 1997, pp. 2780-2788.

[206] S C Mishra and A Lankadasu, "Transient conduction-radiation heat transfer in participating media using the lattice boltzmann method and the discrete transfer method," *Numerical Heat Transfer, Part A*, 47, 2005, pp.935-954.

[207] H Zhang, "Lattice Boltzmann method for solving the bioheat equation," *Phys. Med. Biol*., 53, 2008, pp. N15-23.

[208] W Miller, "The lattice Boltzmann method: a new tool for numerical simulation of the interaction of growth kinetics and melt flow," *Journal of Crystal Growth*, 230(1-2), 2001, pp. 263-269.

[209] W Miller, I Rasin, and S Succi, "Lattice Boltzmann phase-field modelling of binary-alloy solidification," *Physica A*, 362, 2006, pp. 78-83.

[210] D Sun, M Zhu, S Pan, and D Reabbe, “Lattice Boltzmann modeling of dendritic growth in a forced melt convection,” *Acta Materialia*, 57, 2009, pp. 1755-1767.

[211] Y Peng, C Shu, and Y T Chew, "Simplified thermal lattice Boltzmann model for incompressible thermal flows," *Physical Review E*, 68, 2003, pp. 026701.

[212] H N Dixit and V Babu, "simulation of high Rayleigh number natural convection in a square cavity using the lattice boltzmann method," *International Journal of Heat and Mass Transfer*, 49, 2006, pp. 727-739.

[213] C H Liu, K H Lin, H C Mai, and C A Lin, "Thermal boundary conditions for thermal lattice Boltzmann simulation," *Computers & Mathematics with Applications*, 59(7), 2010, pp. 2178-2193.

[214] A D'Orazio and S Succi, "Boundary Conditions for Thermal Lattice Boltzmann Simulations," Computational Science — ICCS 2003, Vol. 2657, pp. 656

[215] S G okaltun and G S Dulikravich, "Lattice Boltzmann computations of incompressible laminar flow and heat transfer in a constricted channel," *Computers and Mathematics with Applications*, 59(7), 2010, pp. 2431-2441.

[216] J S Wu and Y L Shao, “Simulation of lid-driven cavity flows by parallel lattice Boltzmann method using multi-relaxation-time scheme,” *Int. J. Numer. Meth. Fluids*, 46, 2004, pp. 921-937.

APPENDIX A

THERMOPHYSICAL PROPERTIES FOR SOME MATERIALS AND ASSOCIATED CALCULATION PARAMETERS ADOPTED IN THE SIMULATIONS

Table A.1 AISI 410 thermal properties and LENS process parameters

Parameter		Symbol	Units	Value
Density-solid		ρ_s	kg/m^3	7400
Density-liquid		ρ_l	kg/m^3	7150
Thermal conductivity-solid		λ_s	W/m K	28.4
Thermal conductivity-liquid		λ_l	W/m K	24.8
Specific heat of solid		C_s	J/kg K	460
Specific heat of liquid		C_l	J/kg K	520
Latent heat		L	J/kg	2.77×10^5
Liquidus		T_l	K	1799
Solidus		T_s	K	1735
Surface tension gradient		σ_k	N/(m×K)	-4×10^{-4}
Viscosity		μ	N×s/m^2	6.0×10^{-3}
Emissivity		ε	N/A	0.8
Slopes of liquidus	C	m^j	K/wt pct	-75.0
	Si			-15.0
	Mn			-5.0
	Cr			-0.7
Partition Coeff.	C	k^j		0.17
	Si			0.66
	Mn			0.75
	Cr			0.93
Convective heat transfer coefficient		h	W/m^2 K	100
Radius of the laser beam		w_0	mm	0.5

Table A.2 Fe-0.13wt%C thermal properties and calculation parameters

Parameter	Symbol	Units	Value
Density-solid	ρ_s	kg/m^3	7250
Density-liquid	ρ_l	kg/m^3	7100
Thermal conductivity-solid	λ_s	W/m K	27.8
Thermal conductivity-liquid	λ_l	W/m K	25.4
Specific heat of solid	C_s	J/kg K	460
Specific heat of liquid	C_l	J/kg K	520
Latent heat	L	J/kg	2.77×10^5
Liquidus	T_l	K	1784
Solidus	T_s	K	1723
Surface tension gradient	σ_k	N/(m×K)	-4×10^{-4}

Table A.2 (Continued)

Viscosity	μ	N×s/m^2	6.2×10^{-3}
Emissivity	ε	N/A	0.8
Slopes of liquidus	m^j	K/wt pct	-80.0
Partition Coeff.	k^j		0.17
Convective heat transfer coefficient	h	W/m^2 K	100
Radius of the laser beam	w_0	mm	0.5

Table A.3 Mg-8.9wt%Al thermal properties and calculation parameters

Property	Value
Thermal expansion coefficient (β)	-2.6×10^{-5}K^{-1}
Density of liquid (ρ_l) Density of solid (ρ_s)	1650kg m^{-3} 1750kg m^{-3}
Viscosity (μ)	2×10^{-3}N s m^{-2}
Diffusivity of alloy elements in liquid (D_l) Diffusivity of alloy elements in solid (D_s)	5.0×10^{-9}m^2 s^{-1} 5.0×10^{-13} m^2 s^{-1}
Thermal conductivity in liquid (λ_l) Thermal conductivity in solid (λ_s)	80J K^{-1} m^{-1} s^{-1} 105J K^{-1} m^{-1} s^{-1}
Average specific heat of liquid (C_l) Average specific heat of solid (C_s)	1350J kg^{-1} K^{-1} 1200J kg^{-1} K^{-1}
Latent heat of fusion (L)	3.7×10^5J kg^{-1}
Liquidus temperature (T_l)	868K
Eutectic temperature (T_E)	705K
Gibbs-Thomson coefficient	2.0×10^{-7}K·m

Table A.4 Al-3.0wt%Cu thermal properties and calculation parameters

Parameter	Symbol	Units	Value
Density	ρ	kg/m^3	2475
Thermal conductivity	λ	W/m K	30
Thermal diffusivity	α	m^2/s	1/12×10^{-4}
Specific heat	C_p	J/kg K	500
Solute diffusivity	D_l	m^2/s	3×10^{-9}
Liquidus	T_l	K	925.8

Table A.4 (Continued)

Viscosity	μ	N×s/m^2	1.4×10^{-4}
Slopes of liquidus	m	K/wt pct	-2.6
Partition Coeff.	k		0.17
Under cooling		K	4.5
Inflow velocity		m/s	0.0023